Metasurfaces for Ultrathin Optical Devices with Unusual Functionalities

by

Dandan Wen

Submitted for the degree of Doctor of Philosophy

Institute of Photonics and Quantum Sciences

School of Engineering & Physical Sciences

Heriot-Watt University

May 2017

Abstract

Metamaterials are artificial materials that are made from periodically arranged structures, showing properties that cannot be found in nature. The response of a metamaterial to the external field is defined by the geometry, orientation, and distribution of the artificial structures. Many groundbreaking discoveries, such as negative refraction, and super image resolution has been demonstrated based on metamaterials. Nevertheless, the difficulty in three-dimensional fabrication, especially when the operating band is located in the optical range, hinders their practical applications. As a two-dimensional counterpart, a metasurface consists of an array of planar optical antennas, which locally modify the properties of the scattered light. Metasurfaces do not require complicated three-dimensional nanofabrication techniques, and the complexity of the fabrication is greatly reduced. Also, the thickness of a metasurface can be deep subwavelength, making it possible to realize ultrathin devices.

In this thesis, geometric metasurfaces are utilized to realize a series of optical devices with unusual functionalities. Phase gradient metasurface is used to split the incident light into left-handed polarized (LCP) and right-handed polarized (RCP) components, whose intensities can be used to determine the polarization state of the incident light. Then we propose a method to integrate two optical elements with different functionalities into a single metasurface device, and its overall performance is determined by the polarization of the incident light. After that, a helicity multiplexed metasurface hologram is demonstrated to reconstruct two images with high efficiency and broadband. The two images swap their positions with the helicity reversion of the incident light. Finally, a polarization rotator is presented, which can rotate the incident light to arbitrary polarization direction by using the non-chiral metasurface. The proposed metasurface devices may inspire the development of new optical devices, and expand the applications of metasurfaces in integrated optical systems.

Acknowledgements

First, I would like to thank my supervisor Dr. Xianzhong Chen for his great support during my PhD study. Dr. Chen not only led me to the amazing world of nanoscience but also taught me how to think and act when facing with difficulties. I still remember the busy but memorable days when we were doing experiments together in the spring of 2015. Within the three years, he spent a lot of time discussing the technical issues I encountered and revising my papers, without which this thesis would not have been possible. I also sincerely thank my second supervisor Prof. Ajoy K. Kar for his encouragement and support throughout my doctoral program.

I had a great time to work with my colleges in our group. Fuyong helped me a lot since he is an expert on the optical experiments. The circular hole in the screen (figure 5.14) would not be so 'circular' if he did not use the end of a protective tube to cut through the screen. I would like to thank Chunmei for her help in the clean room, and the wonderful dinners she made. Many thanks to our visiting scholars: Prof. Ming Chen, Dr. Huigang Liu, Dr. Xiaofei Zang, and Dr. Zhengren Zhang. The discussions with them always inspired me.

I also sincerely thank Prof. Shuang Zhang, Dr. Guixin Li and Prof. Guoxing Zheng for their generous help. Hereby I would like to thank all the collaborators for their great contributions: Mr. Neil Ross, Mr. Mark Leonard, Dr. Santosh Kumar, Dr. Peter E. Kremer, Prof. Brian D. Gerardot, Prof. Mohammad R. Taghizadeh, Prof. Gerald S. Buller, Dr. Wei Wang, Dr. Shumei Chen, Mr. Kinlong Chan, Dr. Marcus Ardron, Dr. King Fai Li, Dr. Polis Wing Han Wong, Prof. Kok Wai Cheah, Prof. Edwin Yue Bun Pun, Dr. Andrea Di Falco, Mr. James Burch.

In addition, I thank all my friends in Edinburgh for the great time we spent together (in particular for Dr. Ximing Ren, Prof. Jinghua Sun, Dr. Maoshuai Li, Dr. Haoyu Li, Miss Qianru Zhou, Mr. Yang Chen, Dr. Jianyong Chen, Miss Jieyu Wang, Miss Meifen Jiang, Dr. Yong Ma, Prof. Zhaowei Zhang, Dr. Wenxing Tang, Dr. Jia Ni, Mr. Zhou Zhou, Mr. David Vocke, Mr. Hatef Dinparasti Saleh).

I would like to express my most sincere gratitude to my parents and my wife for their unconditional love and ever-lasting support. I am grateful for my grandparents, who experienced so many difficult years, but are still optimistic about the future. My son Zhaoqian was born in May last year, and the little boy has always been an encouragement for me to move forward.

ACADEMIC REGISTRY

Research Thesis Submission

Name:			
School:			
Version: *(i.e. First, Resubmission, Final)*		Degree Sought:	

Declaration

In accordance with the appropriate regulations I hereby submit my thesis and I declare that:

1) the thesis embodies the results of my own work and has been composed by myself
2) where appropriate, I have made acknowledgement of the work of others and have made reference to work carried out in collaboration with other persons
3) the thesis is the correct version of the thesis for submission and is the same version as any electronic versions submitted*.
4) my thesis for the award referred to, deposited in the Heriot-Watt University Library, should be made available for loan or photocopying and be available via the Institutional Repository, subject to such conditions as the Librarian may require
5) I understand that as a student of the University I am required to abide by the Regulations of the University and to conform to its discipline.
6) I confirm that the thesis has been verified against plagiarism via an approved plagiarism detection application e.g. Turnitin.

* *Please note that it is the responsibility of the candidate to ensure that the correct version of the thesis is submitted.*

Signature of Candidate:		Date:	

Submission

Submitted By *(name in capitals)*:	
Signature of Individual Submitting:	
Date Submitted:	

For Completion in the Student Service Centre (SSC)

Received in the SSC by *(name in capitals)*:			
Method of Submission *(Handed in to SSC; posted through internal/external mail)*:			
E-thesis Submitted ***(mandatory for final theses)***			
Signature:		Date:	

Please note this form should be bound into the submitted thesis.
Academic Registry/Version (1) August 2016

Table of Contents

Abstract I

Acknowledgements II

Table of Contents IV

List of Publications VII

Chapter 1 Introduction 1

1.1 Introduction to metasurfaces 1

1.2 Phase control and wavefront shaping 2

1.3 Polarization conversion 6

1.4 Other applications and dielectric metasurfaces 9

1.5 Overview of the thesis 14

1.6 References 14

Chapter 2 Geometric phase and geometric metasurfaces 22

2.1 Introduction to the geometric phase 22

2.2. Scattering properties of a single nanorod and the transmission-type geometric metasurface 23

2.3 The reflection-type geometric metasurface 27

2.4 Conclusion 33

2.5 References 33

Chapter 3 Phase gradient metasurface for polarization measurement 35

3.1 Introduction 35

3.2 Design of the phase gradient metasurface 36

3.3 Experimental characterization of the polarization measurement functionality 38

3.4 Discussion 42

3.5 Conclusion 44

3.6 References 44

Chapter 4 Polarization selective metasurface devices 48

4.1 Introduction 48

4.2 Design methodology of the metasurface PSOE 49
4.2.1 Integration of two completely different phase functions 49
4.2.2 Simulation of the background noise introduced by the merging method 51
4.3 Experimental characterizations of the multifunctional metasurface device 53
4.3.1 Polarization selective properties of the metasurface 53
4.3.2 Broadband performance of the metasurface PSOE 55
4.4 The multifunctional metasurface lens for imaging and Fourier transform 56
4.4.1 Design of the multifunctional metasurface lens 56
4.4.2 Focusing properties of the multifunctional lens 57
4.4.3 Imaging properties of the multifunctional lens 58
4.4.4 Fourier transform by the multifunctional lens 61
4.5 Conclusion 63
4.6 References 63
Chapter 5 Helicity multiplexed broadband metasurface holograms 67
5.1 Introduction 67
5.2 Design of the HMMH 68
5.2.1 Theoretical explanations of the image switchable functionality 68
5.2.2 Realization of the helicity multiplexed functionality using a metasurface 70
5.3 Experimental characterizations of the HMMH 72
5.3.1 Design of the projection angles 72
5.3.2 Other concerns of the metasurface hologram 74
5.3.3 Experimental setup and the reconstructed images versus the polarization state of the incident light 76
5.3.4 Image quality and efficiency of the HMMH 79
5.4 Optimized design of the HMMHs 80
5.4.1 Design principle 80
5.4.2 Efficiency of the optimized metasurface 83
5.5 Conclusions 86

5.6 References 87
Chapter 6 Geometric phase induced broadband optical rotation 89
6.1 Introduction 89
6.2 Design principle of the metasurface for optical rotations 91
6.3 Simulation of the optical rotation functionality 93
6.4 Experimental verification of the optical rotation functionality 95
6.5 Discussion 97
6.6 Conclusion 100
6.7 References 100
Chapter 7 Conclusions and Outlook 102
7.1 Conclusions 102
7.2 Outlook 102
7.3 References 104

List of Publications

Journal papers

1) **D. Wen**, F. Y. Yue, M. Ardron, and X. Z. Chen, "Multifunctional metasurface lens for imaging and Fourier transform," Scientific Reports **6**, 27628 (2016).
2) **D. Wen**, S. Chen, F. Yue, K. Chan, M. Chen, M. Ardron, K. F. Li, P. W. H. Wong, K. W. Cheah, E. Y. B. Pun, G. Li, S. Zhang, and X. Chen, "Metasurface Device with Helicity-Dependent Functionality," Advanced Optical Materials **4**, 321-327 (2016).
3) **D. Wen**, F. Yue, G. Li, G. Zheng, K. Chan, S. Chen, M. Chen, K. F. Li, P. W. H. Wong, K. W. Cheah, E. Yue Bun Pun, S. Zhang, and X. Chen, "Helicity multiplexed broadband metasurface holograms," Nature Communications **6**, 9241 (2015).
4) **D. Wen**, F. Yue, S. Kumar, Y. Ma, M. Chen, X. Ren, P. E. Kremer, B. D. Gerardot, M. R. Taghizadeh, G. S. Buller, and X. Chen, "Metasurface for characterization of the polarization state of light," Optics Express **23**, 10272-10281 (2015).
5) **D. Wen**, F. Yue, C. Zhang, X. Zang, H. Liu, W. Wang and X. Chen, “Geometric phase induced optical rotation,” In preparation.
6) J. Burch, D. Wen, X. Chen, and A. Falco, "Holograms on a finger," In preparation.
7) F. Yue, **D. Wen**, C. Zhang, B. D. Gerardot, W. Wang, S. Zhang and X. Chen, “Multichannel Polarization-Controllable Superpositions of Orbital Angular Momentum States,” Advanced Materials (2017).
8) F. Yue, **D. Wen**, J. Xin, B. D. Gerardot, J. Li, and X. Chen, "Vector Vortex Beam Generation with a Single Plasmonic Metasurface," Acs Photonics **3**, 1558-1563 (2016).
9) X. Chen, M. Chen, M. Q. Mehmood, **D. Wen**, F. Yue, C.-W. Qiu, and S. Zhang, "Longitudinal Multifoci Metalens for Circularly Polarized Light," Advanced optical materials **3**, 201500110 (2015).

Conference papers

1) X.Chen, **D. Wen**, and F. Yue, "Unusual ultrathin optical devices: Metasurfaces make them practical," Piers in Shanghai, China 2016.
2) X. Chen, **D. Wen**, F. Yue, G. Li, G. Zheng, K. Chan, S. Chen, M. Chen, K. F. Li, P. W. H. Wong, K. W. Cheah, E. Y. B. Pun, S. Zhang," Metasurface for helicity multiplexed broadband holograms, " Meta'16, Malaga, Spain 2016.

3) **D. Wen**, F. Yue, S. Kumar, Y. Ma , M. Chen, X. Ren , P. Kremer , B. Gerardot, M. Taghizadeh , G. Buller , and X. Chen, "Polarization Measurement Method Based on Metasurface," Piers in Prague, Cezch Republic 2015.
4) X. Chen, **D. Wen**, F. Yue, and M. Chen, "Ultrathin Planar Optical Devices with Unusual Functionalities," Piers in Prague, Cezch Republic 2015.

Book Chapters

1) X. Chen, **D. Wen**, F. Yue, "Chapter 11: Metasurface and ultrathin optical devices" in "Optical MEMS, Nanophotonics, and Their Applications, " Eds: G. Zhou, C. Lee. Taylor & Francis Books, Inc. To be published.

Chapter 1 Introduction

Metamaterials are engineered to have periodic subwavelength structures, whose responses to the external field are determined by the structures rather than the base materials. These man-made materials have yielded many novel applications ranging from super-resolution imaging to negative refractive index. However, the difficulties in fabrication have hindered their practical applications, especially in the optical range, where high-resolution 3D fabrication is needed. In this chapter, we introduce a kind of 2D metamaterials, or metasurfaces, which greatly reduce the complexity of the fabrication process, and have the ability to tune the properties of light within deep subwavelength ranges. For these reasons, metasurfaces not only open a new avenue to scale down the size of photonic systems but also provide unusual functionalities to optical devices.

1.1 Introduction to metasurfaces

Conventional optical elements, such as lenses and wave-plates gradually change the phase and polarization of light during the propagation. It is difficult to accumulate sufficient phase change once the device size is further reduced to subwavelength scale due to the limited refractive indices of natural materials. To meet the growing requirement of device miniaturization and system integration, a new design methodology is urgently needed to develop ultrathin optical devices.

Metamaterials [1.1] are composed of artificial ‘atoms’ made from metals, dielectrics, and so on. These ‘atoms’ are usually subwavelength and arranged in repeating patterns [1.2]. The structures, orientations and distributions of these ‘atoms’ can be designed to manipulate electromagnetic waves in smart ways. Many unprecedented phenomena, such as super-resolution [1.3], negative refractive index [1.4] and artificial magnetic response [1.5] have been demonstrated using metamaterials. With the development of nanofabrication techniques, the operating wavelengths of metamaterials have been extended from microwave to optical range. However, the applications of metamaterials, especially in the infrared and visible spectrums are hindered by the fabrication difficulties, high losses and strong dispersion [1.6].

Recently, optical metasurfaces [1.7] have drawn much attention for their easy fabrication process and effective control of optical properties. Metasurfaces are composed of optical antennas that can locally change the phase, amplitude, and polarization of the scattered light within subwavelength range, which is completely different from the conventional optical elements relying on the propagation effect. As a

result, metasurface-based ultrathin optical devices such as lenses [1.8], waveplates [1.9] and axicons [1.10] have been developed. Besides, many novel applications have been explored including dual-polarity plasmonic metalens [1.11], anomalous refraction [1.12], giant spin-Hall effect [1.13], unidirectional surface plasmon polariton excitation [1.14], and so on. Although metasurfaces have shown great potential for practical applications, they are still at the infant stage and many new design principles and applications are still under exploration. This thesis aim to develop metasurface devices with unusual functionalities, such as helicity multiplexed holograms [1.15] and broadband polarization rotators [1.16], which further expand the application of metasurfaces in the field of optics.

In this chapter, metasurfaces are classified and introduced based on their functionalities. Since the main goal of metasurfaces is the phase control and wavefront shaping, the corresponding metasurfaces are first introduced in section 1.2. In section 1.3, metasurfaces with polarization conversion and measurement functionalities are reviewed. The two sections are closely related to the major part of this thesis in chapters 3-6. In addition to the phase and polarization control, metasurfaces with other functionalities, such as amplitude modulation and frequency selection are introduced in section 1.4. This section also includes a brief review of dielectric metasurfaces. In section 1.5, the organization of this thesis is provided.

1.2 Phase control and wavefront shaping

Metasurfaces made their debut through flexible control of the wavefront of light [1.7]. Abrupt phase changes can be given to the scattered light if it is transformed by the metasurfaces with deep subwavelength thicknesses. The pixel size of metasurfaces can be much smaller than the commercially available optical elements, such as spatial light modulators. Thus the nanoantennas provide subwavelength resolutions of wavefronts, which eliminate the unwanted higher diffraction orders. Moreover, the wavefront generated by a geometric metasurface [1.17] will be changed to its conjugation if the helicity of the incident light is reversed, giving rise to many novel applications.

A major approach for controlling the phase of the scattered light is the use of antenna dispersion. For an incident light beam shining on a metallic nanoantenna, its resonance condition is related to the size and geometry, which can be adjusted to tune the phase of the scattered light. For example, V-shaped antennas support both symmetric and anti-symmetric modes that are perpendicular to each other [1.7]. When the two modes are excited simultaneously, part of the scattered light has a polarization

cross to that of the incident light due to the distinct resonance conditions of the two resonant modes. The geometries and orientations of the antennas are properly chosen to provide certain phase delay to the cross-polarized light (figure 1.1). The metasurfaces consisting of V-antennas have been applied to realize anomalous refraction and reflection [1.12], lens [1.8, 1.18], axicon [1.10] and holograms [1.19].

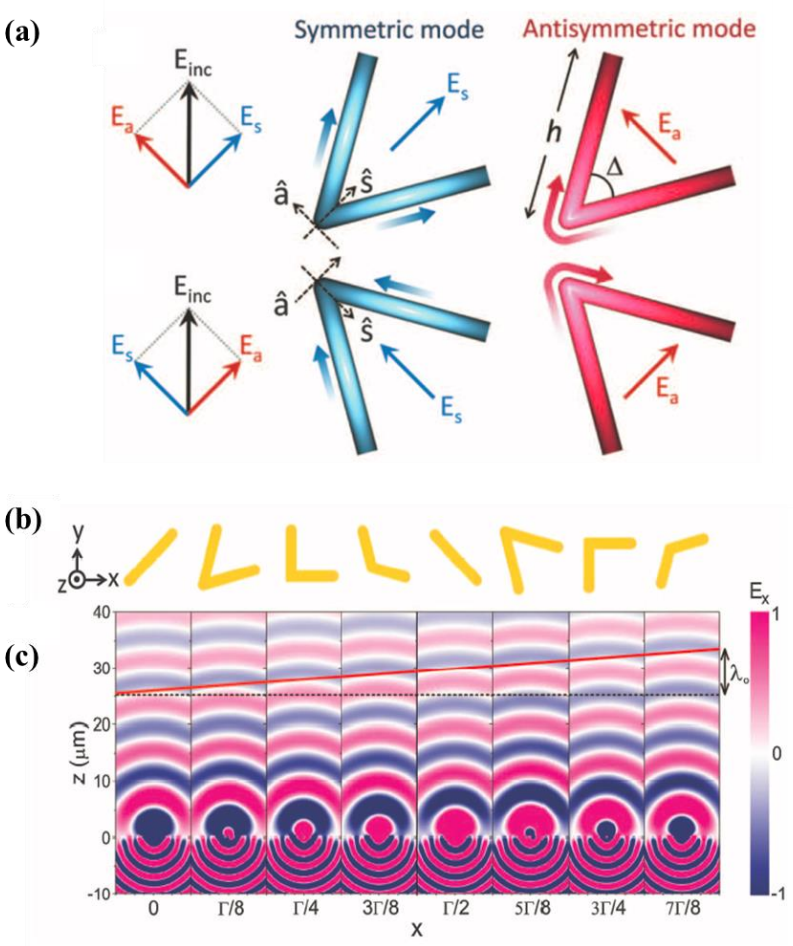

Figure 1.1 Schematic of the metasurface based on V-shaped nanoantennas. (a) The incident light $\mathbf{E_{inc}}$ can excite both the symmetric and antisymmetric modes, which are represented by the blue and red colors, respectively. Since the two modes have different resonance conditions, part of the scattered light has a polarization cross to that of the incident light. (b) Schematic of a supercell containing eight V-antennas. The cross-polarized scattered light from the neighboring antennas is designed to have equal amplitude and a phase difference of $\pi/4$. (c) Simulated electric field of the scattered light from the eight antennas composing the supercell [1.7].

As the simplest nanoantenna, a nanorod can tune the phase of the scattered light polarized along its long axis by adjusting its length [1.20, 1.21]. If the width of the nanorod is increased to form a rectangle-shaped nanoantenna, it will respond anisotropically to the light polarized along the two axes [1.22, 1.23]. Also, C-shaped antennas with different geometries and orientations have been experimentally verified to simultaneously control the phase and amplitude of the scattered light [1.24]. H-shaped

antennas with different heights [1.25] or widths [1.26], patch-dipole antennas [1.27] and multilayer Huygens' surface [1.28-1.30] have also been demonstrated to effectively control the phase.

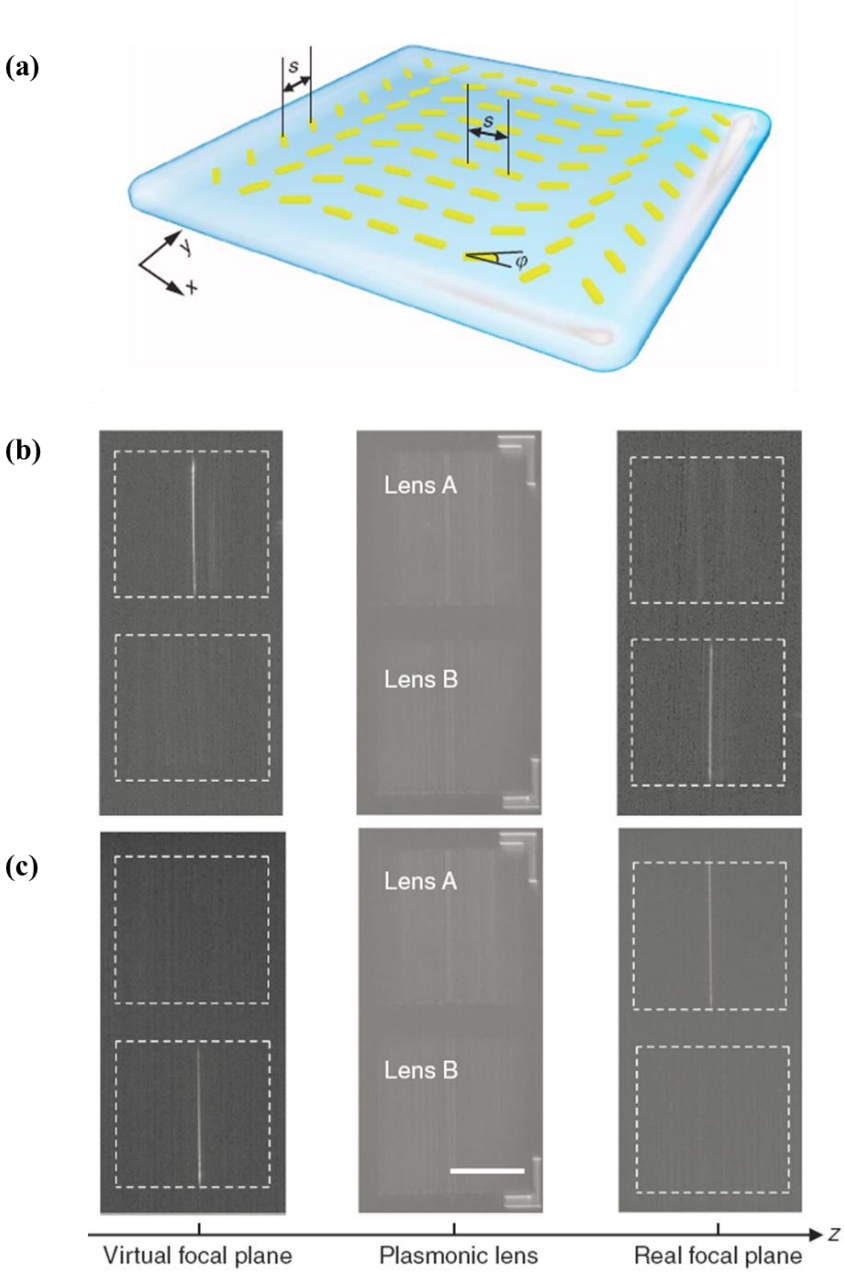

Figure 1.2 Metasurface dual-polarity lens. (a) All the nanorods in the designed metasurface have the same geometry, and their orientations change along the *x*- direction. The pixel pitch *s* has the value of 400 nm. (b) Under the illumination of RCP light, lens A is negative while lens B is positive. Therefore the focal lines are located at the virtual and real focal planes for lens Aand B, respectively. (c) The polarities of both lens are reversed for the LCP incident light [1.11].

For previous examples, metasurfaces are composed of nanoantennas of different shapes, which are designed to give spatially different phase delays to the scattered light. A different approach to introduce abrupt phase changes is to utilize the geometric phase, which is obtained through the polarization conversion caused by an anisotropic scatterer

[1.31]. For the circularly polarized incident light, an anisotropic scatterer can partly change the incident light into its opposite helicity and give a geometric phase $\pm 2\psi$ to it. The parameter ψ is the orientation of the nanorod. '+' sign is valid for the conversion from left-handed circularly polarized (LCP) light to right-handed circularly polarized (RCP) light and the '-' sign for RCP to LCP. As a result, a sampled phase function can be encoded onto an array of nanoantennas that have the same geometry but varying orientations. Since the geometric phase is independent of wavelengths, the metasurface has the potential to work for a broad range of wavelengths.

A typical example of the geometric phase-based metasurfaces is the dual-polarity plasmonic metalens [1.11]. The metasurface is formed by gradually changing the orientations of the gold nanorods along the *x*-direction [figure 1.2(a)]. It can converge the scattered light into a bright focal line at the real or virtual focal plane, depending on the helicity of the incident light [figures 1.2(b)-(c)]. Since the '+' or '-' sign of the geometric phase is determined by the helicity of the incident light, multifunctional metasurface devices and helicity multiplexed broadband metasurface holograms will be presented in chapters 4 and 5, respectively.

If the surface waves are used as reference beams, holographic metasurfaces can tune the wavefront in a similar way to the traditional holograms. The interference pattern is first generated by the reference surface plasmon polaritons (SPP) and the scattered light from the object; then the pattern is transferred to the metallic film by etching apertures along the maximum of interference pattern [1.32], which forms a holographic metasurface. The image of the object can be reconstructed from the metasurface if the reference SPP beam propagates along the surface and passes the etched pattern. Holography with white light illumination [1.33], Airy beam generators [1.34] (figure 1.3) and multi-beam plasmonic collimators [1.35] have been experimentally demonstrated. If the holographic metasurface is used in the opposite way, which means to illuminate the metasurface with a propagating wave with certain wavefronts, the SPP beam with designed wavefront can be generated accordingly. The optical angular momentum detectors [1.36], polarization-controlled directional coupling of SPP [1.14, 1.37], and flexible coherent control of plasmonic spin-Hall effect [1.38] all fall into this category.

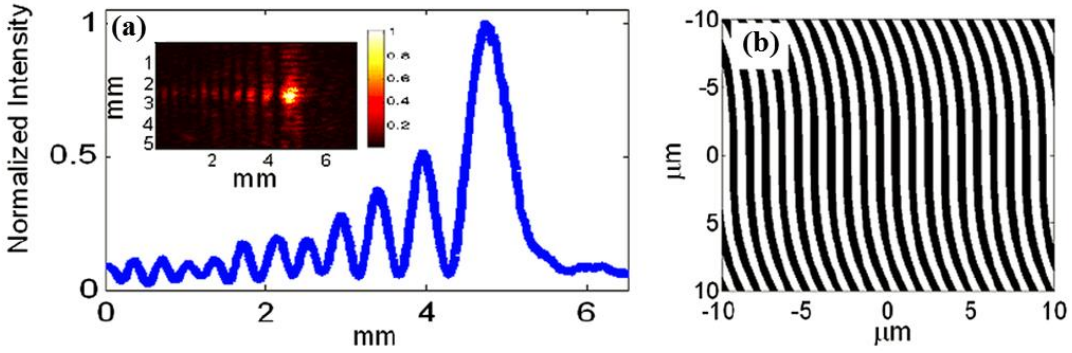

Figure 1.3 Airy beam generated by holographic metasurface The readout SPP wave passes the holographic metasurface (b) and generate the Airy beam (a) in free space [1.34].

1.3 Polarization conversion

Since polarization is one of the basic properties of light, the polarization conversion is crucial for many useful applications, such as photography, sensing and display technology. With the development of nanofabrication techniques, metasurface-based miniature optical devices show great potential in polarization conversion, which will be introduced in the following based on different working mechanisms.

A natural birefringent crystal has a refractive index that is related to the polarization state of the incident light, and therefore it has the capacity to serve as a waveplate. Similarly, a metasurface can realize birefringence by using a single layer of anisotropic nanoantennas. For example, two nanoslits can be placed perpendicular to each other, and each nanoslit mainly interacts with the incident light polarized along its long axis. The two scattered light beams with orthogonal polarization can be designed to have equal amplitude and a $\pi/2$ phase difference at certain wavelength range, where the metasurface functions as a quarter-wave plate [figure 1.4(a)] [1.39-1.41]. Other metasurfaces consisting of anisotropic antennas such as split-ring [1.42] shaped, cross-shaped [1.43] and L-shaped antennas [1.44] have also been demonstrated as quarter-wave plates. A phase gradient metasurface composed of anisotropic nanorods that separate the LCP and RCP components of the incident light can be used for polarization measurement, which will be illustrated in chapter 3.

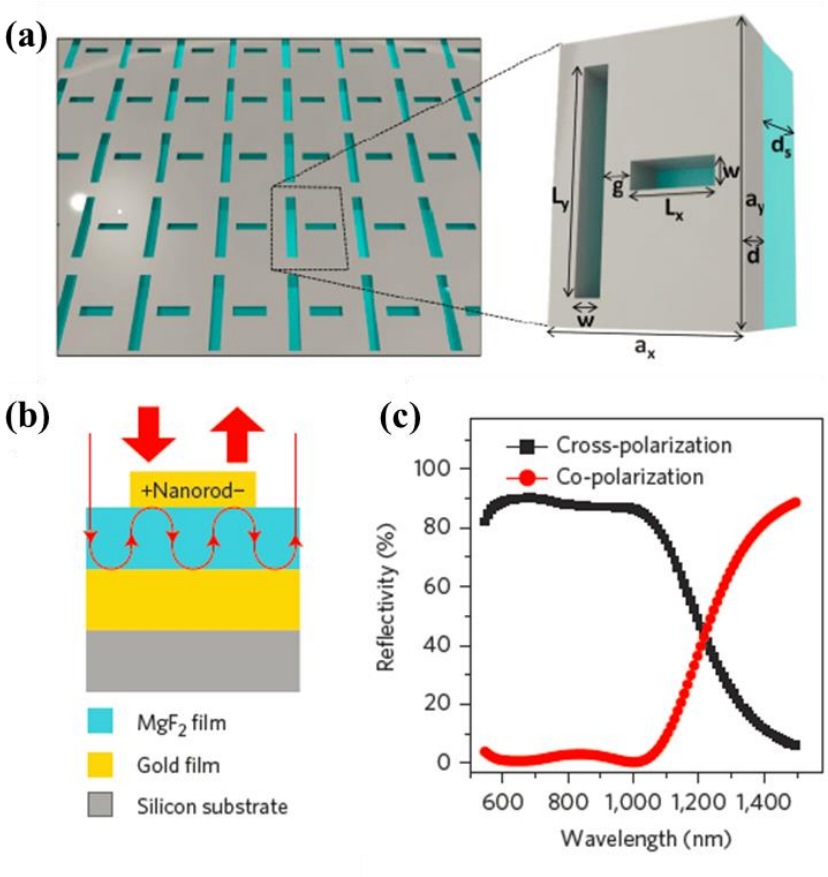

Figure 1.4 Metasurface based quarter-wave plate and half-wave plate. (a) The light beams polarized along the two nanoslits are designed to have the equal transmissivity and a phase difference of $\pi/2$ for a given wavelength, therefore the metasurface functions as a quarter-wave plate [1.41]. (b) Schematic of the half-wave plate based on reflection-type metasurface, which consists of a nanorod layer on the top, a dielectric spacer in the middle and a reflective layer at the bottom. (c) The simulated conversion efficiency of the metasurface [1.17]. The metasurface can convert most of the incident circularly polarized light into its cross-polarization, similar to a traditional half-wave plate.

In comparison with metasurfaces based on single-layer anisotropic nanoantennas, multilayer anisotropic metasurfaces, although complicated in fabrication, show obvious advantages in polarization conversion [1.45-1.47]. For example, three cascaded anisotropic layers provide the required admittances, which aim to convert the transmitted light to any designed polarization [1.48, 1.49]. High extinction ratio metasurface polarizers operating at telecommunication wavelengths are realized using metasurfaces of three layers [1.50]. To improve the conversion efficiency and broaden the operational bandwidth, reflection-type multilayer metasurfaces are designed that include an anisotropic nanoantenna layer, a dielectric spacer, and a reflective layer [figure 1.4(b)]. The broadband performance arises from the interplay between the dispersion of the nanoantenna layer and the Fabry–Pérot like cavity formed by the three

layers. Reflection-type half- or quarter-wave plates [1.51-1.54], polarization converters [1.55, 1.56] and polarization beam splitters [1.57] have been experimentally verified.

For the metasurfaces mentioned above, the desired polarization state of the scattered light can be realized by each unit cell independently. On the contrary, a metasurface based polarization element can also work based on the collective operation of all the nanoantennas. For example, a metasurface contains two subunits can generate two linearly polarized scattered light beams with cross-polarization [1.9] or two circularly polarized light beams with opposite helicities [1.58]. The spatial separation of the two subunits provides a phase difference $\Delta\Phi$ to the orthogonally polarized light beams, which then superpose and form a new polarization [figure 1.5(a)]. To improve the conversion efficiency and expand the operational bandwidth to visible range, a broadband polarization rotator will be presented in chapter 6 that based on metasurface rectangular phase grating.

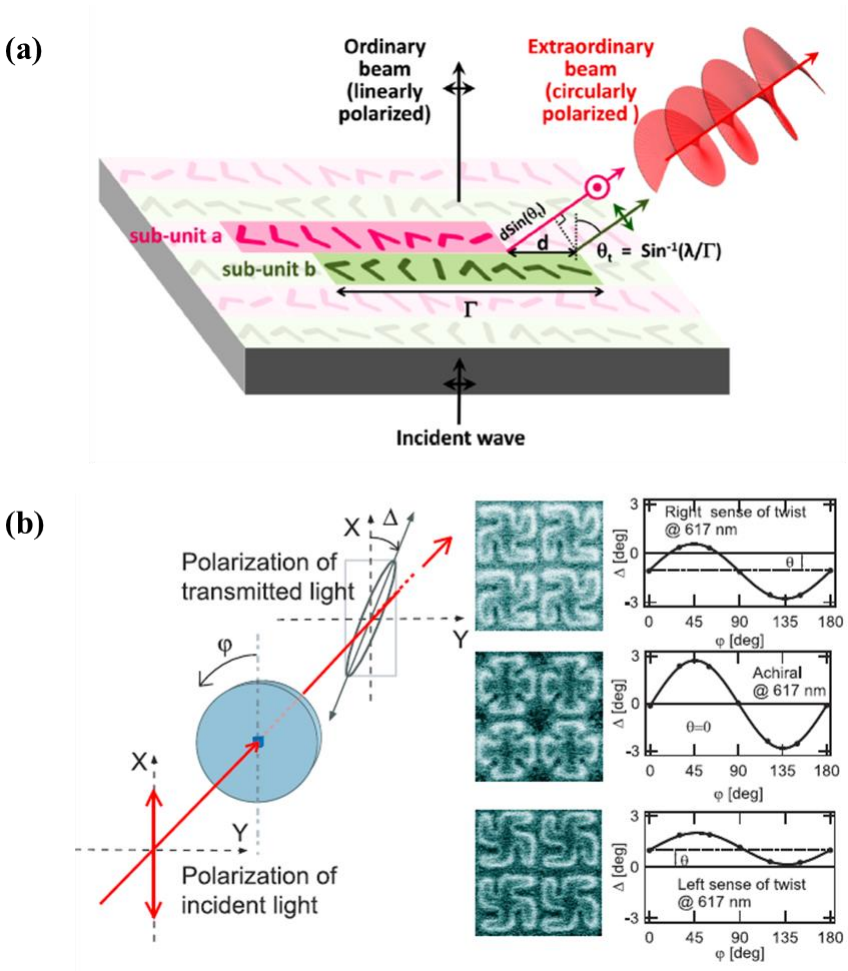

Figure 1.5 (a) The scattered light beams from subunits a and b have a phase difference of $\pi/2$, which is induced by the spatial separation of the two subunits [1.9]. (b) The rotation angle of the polarization ellipse Δ has an offset angle θ when the structures have left- or right-hand twist [1.59].

Materials with chiral structures lift the degeneracy of LCP and RCP components and induce the optical rotation. A three-dimensional material is defined to be chiral if it lacks any planes of mirror symmetry [1.60]. Similarly, a two-dimensional chiral metasurface can be defined as the one containing nanoantennas, which cannot be brought into congruence with their mirror images unless they are lifted from the plane [1.61]. Since there is an additional interaction between the chirality of the incident wave and the chirality of the nanostructures, a chiral metasurface responses differently to the incident LCP and RCP light [figure 1.5(b)]. Therefore the transmitted light from the metasurface changes its polarization accordingly. Chiral metasurfaces have been used as polarization rotators [1.59, 1.61, 1.62], circular polarization filter [1.63, 1.64], and so on [1.65, 1.66].

1.4 Other applications and dielectric metasurfaces

The majority of metasurface applications fall into the categories of wavefront or polarization control as discussed in sections 1.2-1.3. However, metasurfaces prove to be efficient in many other areas including the amplitude control, frequency selection, and so on. In this section, an introduction is given to these novel applications. Although dielectric metasurfaces are not involved in the main body of this thesis, an overview of dielectric metasurfaces is given in this section providing their abilities to achieve higher efficiency in transmission mode than their metallic counterparts.

First, metasurfaces used for amplitude control of the scattered light are introduced. The simplest form of amplitude control is the binary modulation, where a function is sampled and represented by a matrix consisting of elements with the values of either 1 or 0. The matrix can be encoded onto a metasurface, where each nanorod represent an element with nonzero value [1.67]. To obtain the multiple levels of amplitude modulation, V-shaped nanoantennas of different arm lengths and splitting angles [figures 1.6(a)-(b)] [1.19], or L-shaped antennas with tunable arm length differences [1.68] have been experimentally demonstrated. Arbitrary levels of amplitude modulation are realized by using C-shaped antennas, where the amplitude of the scattered light is determined by the angular orientations of the antennas [1.69].

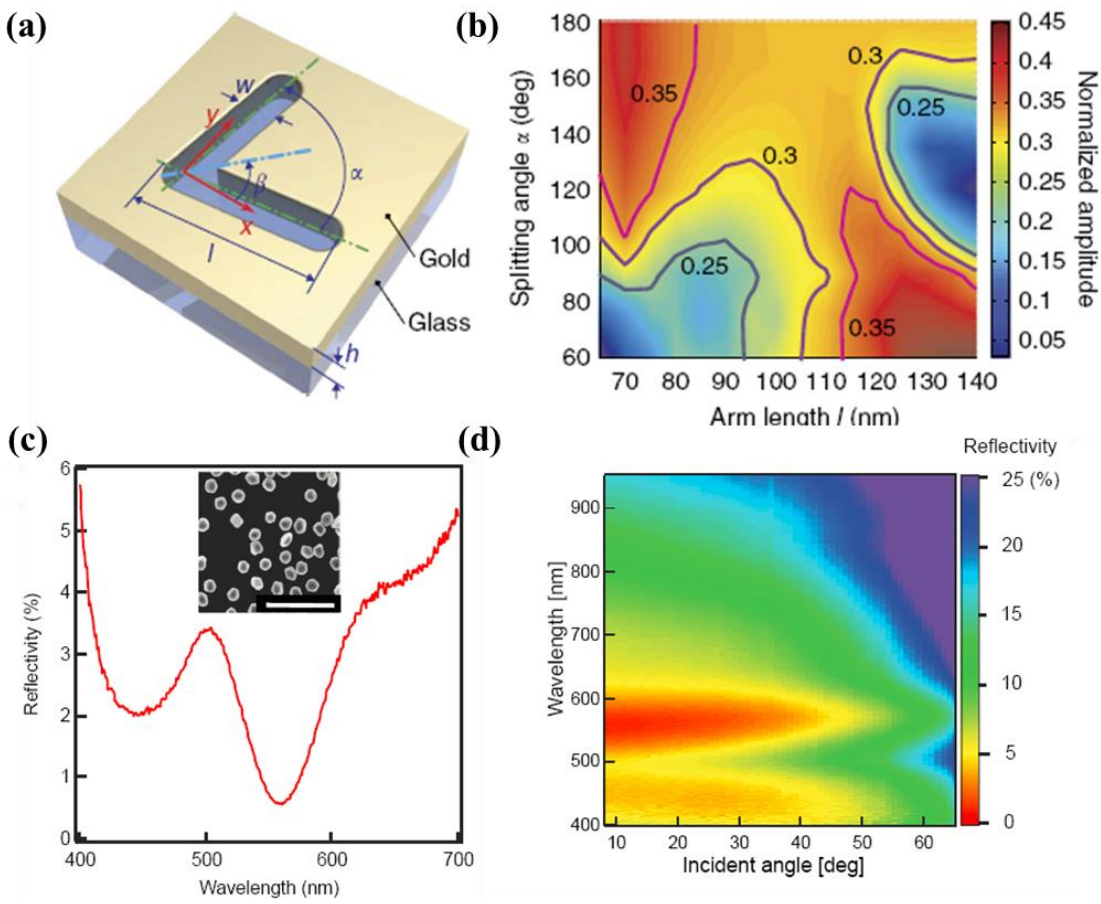

Figure 1.6 (a) A V-aperture antenna that is etched into the gold film. The antenna can partly convert the linear polarization into its orthogonal one. (b) The amplitude of the converted light versus the arm lengths and split angles of the V-antennas [1.19]. (c) Reflection spectrum of a silicon substrate covered with gold nanoparticles. The inset is the SEM image of the sample, and the scale bar is 1 μm. The minimum reflectivity is located at 560 nm with the value of 0.5% (d) Measured reflection spectrum versus the incident angles [1.70].

The spectral response of a metasurface is dependent on the antenna geometry, packing density and other parameters, which yields many interesting applications. For example, high resolution color prints are demonstrated by using nanodisks of different diameters [1.71], where the plasmon resonance of a disk determines the color of an individual pixel. Similarly, nano-gratings with different geometries [1.72, 1.73] or orientations [1.74] can create vibrant colors. Besides the plasmonic color printing, multicolor holograms [1.20, 1.75], polarization-dependent color switching [1.76] and dual wavelength diffractive lenses [1.77] are also developed. Elimination of undesired wavelengths of the reflected light is important for many applications [1.78]. A single layer of disordered gold nanoparticles have been experimentally demonstrated to completely absorb the reflected light over a wide range of incident angles, yielding a zero reflectance meta-film [figures 1.6(c)-(d)] [1.70].

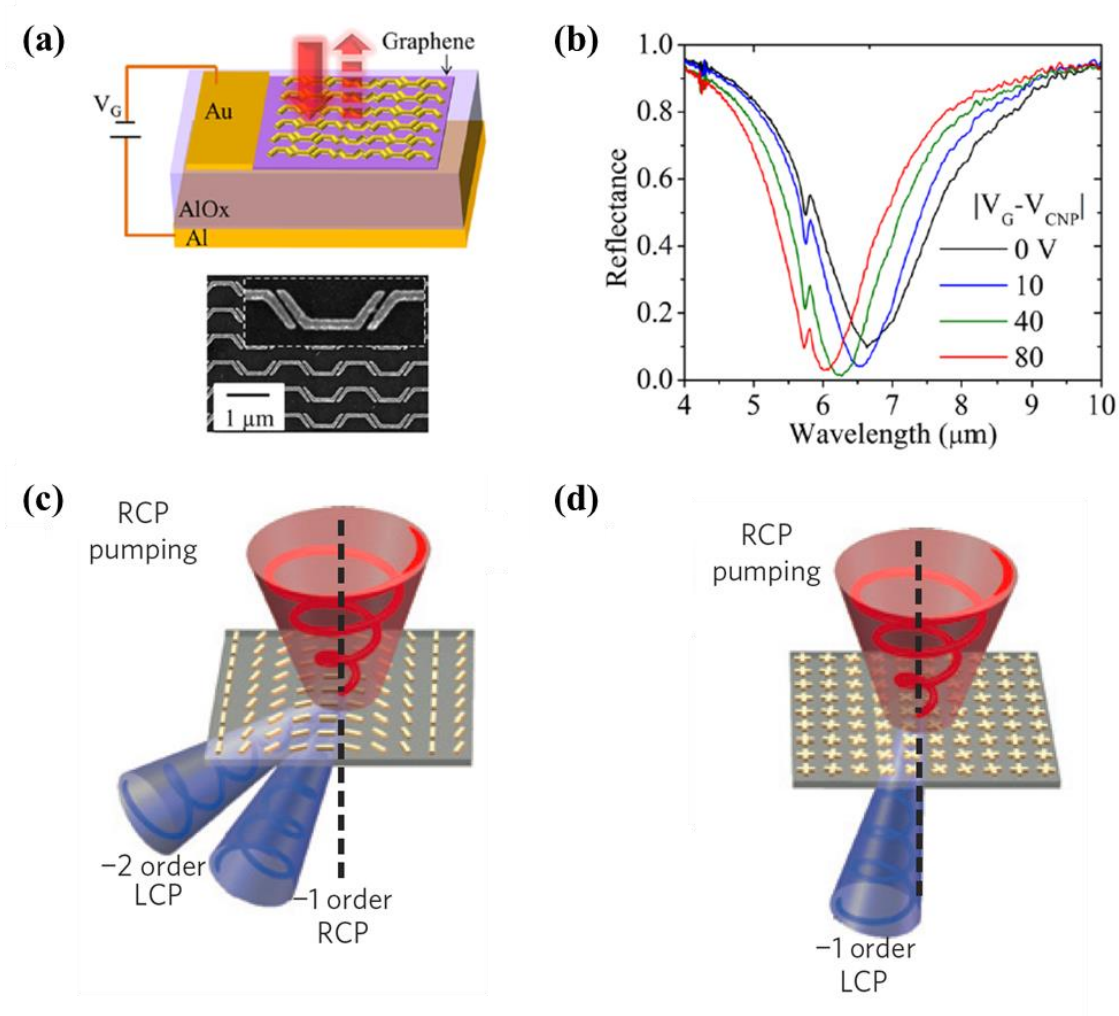

Figure 1.7 (a) Schematic of the tunable metasurface absorber, which is composed of an array of nanoantennas on graphene, an aluminum oxide layer and an aluminum substrate. (b) Simulated reflection spectrum from the metasurface for different gate voltages $|V_G-V_{CNP}|$. V_{CNP} represents the gate voltage when the concentrations of electrons and holes in the graphene sheet are equal [1.79]. (c) The metasurface with two-fold rotational symmetry allows third order harmonic generation (THG), but the RCP and LCP THG signals are diffracted to the first and second orders, respectively, since they have different phase gradients. (d) The metasurface with four-fold rotational symmetry diverts the LCP THG signal to the first-order [1.80].

The combination of metasurfaces and electrically tunable materials offer a degree of freedom to tune the properties of the scattered light. The conductivity and permittivity of graphene are tunable versus the gate voltage. Hence the polarization [1.81], reflection [1.79], transmission [1.82] and frequency shifts [1.83] of the scattered light from a metasurface can be dynamically modulated if it is integrated with graphene [figures 1.7(a)-(b)]. To enhance the Faraday rotation in a magneto-optical thin film, a metasurface is utilized to introduce the localized plasmonic resonance that interacts strongly with the waveguide mode in the film [1.84, 1.85]. Besides the commonly used gold and silver, metasurfaces can be made of alternative materials such as transition

metal nitrides and transparent conductive oxides, which show great dynamic tunability [1.86, 1.87].

The capability to locally change the nonlinear optical properties of materials has great significance for real applications. Recently, metasurfaces have been utilized to generate high harmonics and locally control their phase shifts. For example, geometric phases can be given to the nonlinear polarizabilities of the n^{th} harmonic [1.80], and therefore the propagation of harmonic signals can be completely controlled [figures 1.7(c)-(d)]. Based on the same principle, nonlinear metasurface holography with spin and wavelength multiplexing is realized through the proper arrangement of split ring antennas [1.88]. If a geometric metasurface is loaded by highly nonlinear multi-quantum-well substrates, second order beam steering, focusing and polarization manipulation can be achieved thereby [1.89].

A majority of metasurface researchers have focused on the metallic nanostructures; however, the low conversion efficiency in the transmission mode hinders the further applications. High refractive index dielectric materials do not suffer from the Ohmic losses of the metallic structures. Besides, the dielectric resonators enable both the electric and magnetic resonances that are adjustable through geometries and packing densities of the dielectric nanoantennas. Many interesting functionalities have been realized using dielectric metasurfaces, such as directional scatterers [1.90] and broadband waveplates [1.91], etc.

A dielectric nanoantenna can be properly designed to provide the scattered light with desired property. For example, a silicon elliptical post can give certain phase delays to the light polarized along its long and short axes; hence both the phase and polarization of the scattered light can be controlled [figures 1.8(a)-(b)]. It is worth noting that the experimentally measured efficiency in transmission mode ranges from 72% to 97% depending on exact designs [1.92]. If the elliptical posts are used as building blocks, subwavelength thick lens [1.93, 1.94], optical function decouples [1.95] can be realized. Besides the elliptical posts, silicon cuboids with different geometries can provide phase modulations to the scattered light, which are used to realize beam deflectors and vortex beam generators at near infrared [1.96]. By using high aspect ratio dielectric nanoantennas, whose scattering contributions of several multipoles are overlapped [1.91], broadband half-wave plates and quarter-wave plates are achieved.

Benefiting from the high refractive index of the dielectric nanoantennas, the modes are highly confined, and therefore the scattered light from an antenna is merely affected by its neighbors. Nevertheless, the coupling between two closely spaced antennas can

provide additional freedoms for optical properties control. A unit comprised of two coupled rectangular dielectric resonators can be designed to have distinct phase delays for three different wavelengths, resulting in a multi-wavelength achromatic metasurface [1.97, 1.98].

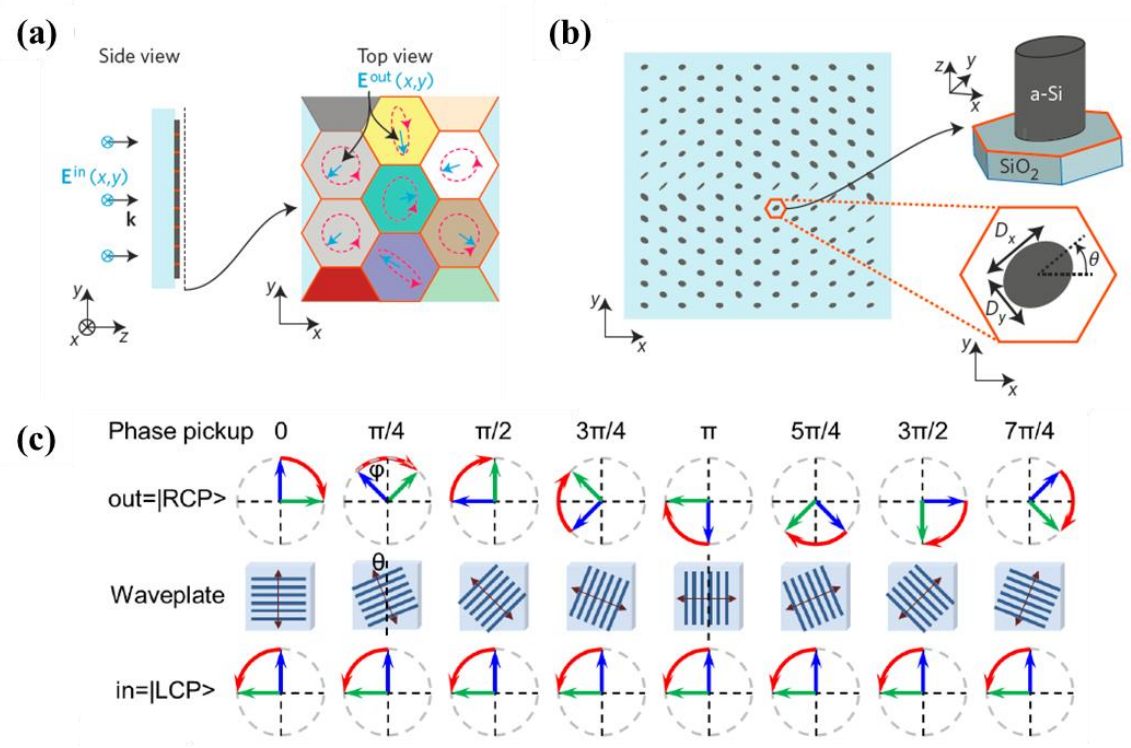

Figure 1.8 (a) The dielectric metasurface based on silicon elliptical posts. The incident light $\mathbf{E}_{in}$ can be locally changed into the output light $\mathbf{E}_{out}$ with arbitrary phase and polarization. (b) The silicon elliptical posts have the same height, but different geometries and orientations [1.92]. (c) Working principles of the dielectric metasurface based on silicon nanobeam arrays. Middle: the silicon nanobeam arrays function as half-wave plates with the fast axes rotating from 0 to 7π/8 counterclockwise. Bottom: The incident light is LCP. Top: The output beam is RCP with the picked-up phase ranging from 0 to 7π/4 [1.99].

The phase shifts of the scattered light from the dielectric nanoantennas mentioned above are closely related to the geometries of the antennas. However, dielectric metasurfaces based on geometric phases can serve as alternatives. A dielectric metasurface consisting of silicon nanobeam array located on the surface of the glass is shown in figure 1.8(c), each nanobeam array has the same functionality of a half-wave plate with the fast axis perpendicular to the nanobeams. Therefore the metasurface can imprint a locally varying geometric phase to the scattered light that has an opposite helicity with regard to the incident light. The metasurface also features with high transmission efficiency with 75% at 550nm [1.99]. If TiO_2 nanofins are used as building blocks to provide geometric phases, a high numerical aperture lens with magnification as high as 170× and high efficiency over the visible wavelength range is proposed [1.100].

Dielectric materials that are tunable versus the external field can be utilized as building blocks to form active metasurfaces. Chalcogenide compound $Ge_2Sb_2Te_5$ (GST) has the capacity to be changed from the amorphous state to the crystalline state according to the temperatures, or vice versa. By controlling the number of pulses emitting from a high-repetition-rate femtosecond laser, the functionality of a GST based metasurface can be erased and rewritten in a dynamical way [1.101]. By putting a temperature tuned lossy dielectric film onto a lossy substrate, the reflected light from the air/film interface and the film/substrate interface can have tunable phases, which makes it possible to engineer the reflectance of the reflected light versus the temperature [1.102].

1.5 Overview of the thesis

The thesis begins with an introduction chapter, which includes the concept of metasurfaces and their applications. In chapter 2, the background information about the geometric phase is first introduced, followed by the basic working mechanisms of the transmission and reflection-type geometric metasurfaces that are the basis of the following chapters. Chapters 3 and 4 demonstrate novel applications based on transmission-type metasurfaces. Phase gradient metasurface for polarization measurement (chapter 3) and metasurface device that tunes the wavefront based on the helicity of the incident light (chapter 4) are presented. To improve the conversion efficiency of the transmission-type metasurfaces, the reflection-type metasurfaces are adopted in chapters 5 and 6. A helicity multiplexed metasurface hologram (chapter 5) and a polarization rotator (chapter 6) are developed, whose design principles and high performances within a broadband may facilitate the future application of metasurfaces. The last chapter summarizes this thesis and gives the prospect of future work.

1.6 References

1.1 J. B. Pendry, D. Schurig, and D. R. Smith, *Controlling Electromagnetic Fields*, Science **312**, 1780-1782 (2006).

1.2 *https://en.wikipedia.org/wiki/Metamaterial*

1.3 N. Fang, H. Lee, C. Sun, and X. Zhang, *Sub–Diffraction-Limited Optical Imaging with a Silver Superlens*, Science **308**, 534-537 (2005).

1.4 R. A. Shelby, D. R. Smith, and S. Schultz, *Experimental Verification of a Negative Index of Refraction*, Science **292**, 77-79 (2001).

1.5 T. J. Yen, et al., *Terahertz Magnetic Response from Artificial Materials*, Science **303**, 1494-1496 (2004).

1.6 C. Hou-Tong, J. T. Antoinette, and Y. Nanfang, *A review of metasurfaces: physics and applications*, Rep. Prog. Phys. **79**, 076401 (2016).

1.7 N. Yu, et al., *Light Propagation with Phase Discontinuities: Generalized Laws of Reflection and Refraction*, Science **334**, 333-337 (2011).

1.8 X. J. Ni, S. Ishii, A. V. Kildishev, and V. M. Shalaev, *Ultra-thin, planar, Babinet-inverted plasmonic metalenses*, Light-Sci Appl **2**, e72 (2013).

1.9 N. Yu, et al., *A Broadband, Background-Free Quarter-Wave Plate Based on Plasmonic Metasurfaces*, Nano Lett. **12**, 6328-6333 (2012).

1.10 F. Aieta, et al., *Aberration-Free Ultrathin Flat Lenses and Axicons at Telecom Wavelengths Based on Plasmonic Metasurfaces*, Nano Lett. **12**, 4932-4936 (2012).

1.11 X. Z. Chen, et al., *Dual-polarity plasmonic metalens for visible light*, Nat. Commun. **3**, 2207 (2012).

1.12 F. Aieta, et al., *Out-of-Plane Reflection and Refraction of Light by Anisotropic Optical Antenna Metasurfaces with Phase Discontinuities*, Nano Lett. **12**, 1702-1706 (2012).

1.13 X. B. Yin, Z. L. Ye, J. Rho, Y. Wang, and X. Zhang, *Photonic Spin Hall Effect at Metasurfaces*, Science **339**, 1405-1407 (2013).

1.14 L. L. Huang, et al., *Helicity dependent directional surface plasmon polariton excitation using a metasurface with interfacial phase discontinuity*, Light-Sci Appl **2**, e70 (2013).

1.15 D. Wen, et al., *Helicity multiplexed broadband metasurface holograms*, Nat. Commun. **6**, 9241 (2015).

1.16 D. Wen, et al., *Geometric phase induced polarization rotation*, submitted to Light-Sci Appl.

1.17 G. Zheng, et al., *Metasurface holograms reaching 80% efficiency*, Nat. Nano. **10**, 308-312 (2015).

1.18 X. Y. Jiang, et al., *An ultrathin terahertz lens with axial long focal depth based on metasurfaces*, Opt. Express **21**, 30030-30038 (2013).

1.19 X. Ni, A. V. Kildishev, and V. M. Shalaev, *Metasurface holograms for visible light*, Nat. Commun. **4**, 3807 (2013).

1.20 Y. W. Huang, et al., *Aluminum Plasmonic Multicolor Meta-Hologram*, Nano Lett. **15**, 3122-3127 (2015).

1.21 S. L. Sun, et al., *High-Efficiency Broadband Anomalous Reflection by Gradient Meta-Surfaces*, Nano Lett. **12**, 6223-6229 (2012).

1.22 M. Farmahini-Farahani, and H. Mosallaei, *Birefringent reflectarray metasurface for beam engineering in infrared*, Opt. Lett. **38**, 462-464 (2013).

1.23 A. Pors, and S. I. Bozhevolnyi, *Efficient and broadband quarter-wave plates by gap-plasmon resonators*, Opt. Express **21**, 2942-2952 (2013).

1.24 L. X. Liu, et al., *Broadband Metasurfaces with Simultaneous Control of Phase and Amplitude*, Adv. Mater. **26**, 5031-5036 (2014).

1.25 S. L. Sun, et al., *Gradient-index meta-surfaces as a bridge linking propagating waves and surface waves*, Nat. Mater. **11**, 426-431 (2012).

1.26 X. Li, et al., *Flat metasurfaces to focus electromagnetic waves in reflection geometry*, Opt. Lett. **37**, 4940-4942 (2012).

1.27 Y. Yifat, et al., *Highly Efficient and Broadband Wide-Angle Holography Using Patch-Dipole Nanoantenna Reflectarrays*, Nano Lett. **14**, 2485-2490 (2014).

1.28 F. Monticone, N. M. Estakhri, and A. Alu, *Full Control of Nanoscale Optical Transmission with a Composite Metascreen*, Phys. Rev. Lett. **110**, 203903 (2013).

1.29 C. Pfeiffer, et al., *Efficient Light Bending with Isotropic Metamaterial Huygens' Surfaces*, Nano Lett. **14**, 2491-2497 (2014).

1.30 C. Pfeiffer, and A. Grbic, *Metamaterial Huygens' Surfaces: Tailoring Wave Fronts with Reflectionless Sheets*, Phys. Rev. Lett. **110**, 197401 (2013).

1.31 M. Kang, T. H. Feng, H. T. Wang, and J. S. Li, *Wave front engineering from an array of thin aperture antennas*, Opt. Express **20**, 15882-15890 (2012).

1.32 P. Genevet, *Holographic optical metasurfaces-a review of current progress*, *Rep. Prog. Phys.* **78**, 024401 (2014).

1.33 M. Ozaki, J.-i. Kato, and S. Kawata, *Surface-Plasmon Holography with White-Light Illumination*, Science **332**, 218-220 (2011).

1.34 I. Dolev, I. Epstein, and A. Arie, *Surface-Plasmon Holographic Beam Shaping*, Phys. Rev. Lett. **109**, 203903 (2012).

1.35 J. P. Tetienne, et al., *Dipolar modeling and experimental demonstration of multi-beam plasmonic collimators*, New J. Phys. **13**, 053057 (2011).

1.36 P. Genevet, J. Lin, M. A. Kats, and F. Capasso, *Holographic detection of the orbital angular momentum of light with plasmonic photodiodes*, Nat. Commun. **3**, 2293 (2012).

1.37 J. Lin, et al., *Polarization-Controlled Tunable Directional Coupling of Surface Plasmon Polaritons*, Science **340**, 331-334 (2013).

1.38 S. Xiao, F. Zhong, H. Liu, S. Zhu, and J. Li, *Flexible coherent control of plasmonic spin-Hall effect*, Nat. Commun. **6**, 8360 (2015).

1.39 Y. Zhao, and A. Alu, *Tailoring the Dispersion of Plasmonic Nanorods To Realize Broadband Optical Meta-Waveplates*, Nano Lett. **13**, 1086-1091 (2013).

1.40 E. H. Khoo, E. P. Li, and K. B. Crozier, *Plasmonic wave plate based on subwavelength nanoslits*, Opt. Lett. **36**, 2498-2500 (2011).

1.41 Y. Zhao, and A. Alu, *Manipulating light polarization with ultrathin plasmonic metasurfaces*, Phys. Rev. B **84**, 205428 (2011).

1.42 A. C. Strikwerda, et al., *Comparison of birefringent electric split-ring resonator and meanderline*, Opt. Express **17**, 136-149 (2009).

1.43 A. Roberts, and L. Lin, *Plasmonic quarter-wave plate*, Opt. Lett. **37**, 1820-1822 (2012).

1.44 B. Yang, W.-M. Ye, X.-D. Yuan, Z.-H. Zhu, and C. Zeng, *Design of ultrathin plasmonic quarter-wave plate based on period coupling*, Opt. Lett. **38**, 679-681 (2013).

1.45 R.-H. Fan, et al., *Freely Tunable Broadband Polarization Rotator for Terahertz Waves*, Adv. Mater. **27**, 1201-1206 (2015).

1.46 T. Li, S. M. Wang, J. X. Cao, H. Liu, and S. N. Zhu, *Cavity-involved plasmonic metamaterial for optical polarization conversion*, Appl. Phys. Lett. **97**, 261113 (2010).

1.47 J. X. Li, et al., *Simultaneous Control of Light Polarization and Phase Distributions Using Plasmonic Metasurfaces*, Adv. Funct. Mater. **25**, 704-710 (2015).

1.48 C. Pfeiffer, and A. Grbic, *Bianisotropic Metasurfaces for Optimal Polarization Control: Analysis and Synthesis*, Phys. Rev. A **2**, 044011 (2014).

1.49 C. Pfeiffer, C. Zhang, V. Ray, L. J. Guo, and A. Grbic, *High Performance Bianisotropic Metasurfaces: Asymmetric Transmission of Light*, Phys. Rev. Lett. **113**, 023902 (2014).

1.50 H. Kurosawa, B. Choi, Y. Sugimoto, and M. Iwanaga, *High-performance metasurface polarizers with extinction ratios exceeding 12000*, Opt. Express **25**, 4446-4455 (2017).

1.51 A. Pors, M. G. Nielsen, and S. I. Bozhevolnyi, *Broadband plasmonic half-wave plates in reflection*, Opt. Lett. **38**, 513-515 (2013).

1.52 F. Ding, Z. Wang, S. He, V. M. Shalaev, and A. V. Kildishev, *Broadband High-Efficiency Half-Wave Plate: A Supercell-Based Plasmonic Metasurface Approach*, ACS Nano **9**, 4111-4119 (2015).

1.53 Z. H. Jiang, et al., *Broadband and Wide Field-of-view Plasmonic Metasurface-enabled Waveplates*, Sci. Rep. **4**, 07511 (2014).

1.54 S. C. Jiang, et al., *Controlling the Polarization State of Light with a Dispersion-Free Metastructure*, Phys. Rev. X **4**, 021026 (2014).

1.55 N. K. Grady, et al., *Terahertz Metamaterials for Linear Polarization Conversion and Anomalous Refraction*, Science **340**, 1304-1307 (2013).

1.56 F. Wang, A. Chakrabarty, F. Minkowski, K. Sun, and Q.-H. Wei, *Polarization conversion with elliptical patch nanoantennas*, Appl. Phys. Lett. **101**, 023101 (2012).

1.57 A. Pors, M. G. Nielsen, and S. I. Bozhevolnyi, *Plasmonic metagratings for simultaneous determination of Stokes parameters*, Optica **2**, 716-723 (2015).

1.58 A. Shaltout, J. Liu, V. M. Shalaev, and A. V. Kildishev, *Optically Active Metasurface with Non-Chiral Plasmonic Nanoantennas*, Nano Lett. **14**, 4426-4431 (2014).

1.59 M. Kuwata-Gonokami, et al., *Giant optical activity in quasi-two-dimensional planar nanostructures*, Phys. Rev. Lett. **95**, 227401 (2005).

1.60 S. Zhang, et al., *Negative Refractive Index in Chiral Metamaterials*, Phys. Rev. Lett. **102**, 023901 (2009).

1.61 A. Papakostas, et al., *Optical Manifestations of Planar Chirality*, Phys. Rev. Lett. **90**, 107404 (2003).

1.62 Y.-P. Jia, et al., *Complementary chiral metasurface with strong broadband optical activity and enhanced transmission*, Appl. Phys. Lett. **104**, 011108 (2014).

1.63 J. J. Cadusch, T. D. James, A. Djalalian-Assl, T. J. Davis, and A. Roberts, *A Chiral Plasmonic Metasurface Circular Polarization Filter*, IEEE PHOTONIC TECH L **26**, 2357-2360 (2014).

1.64 E. Plum, and N. I. Zheludev, *Chiral mirrors*, Appl. Phys. Lett. **106**, 221901 (2015).

1.65 J. H. Shi, H. F. Ma, C. Y. Guan, Z. P. Wang, and T. J. Cui, *Broadband chirality and asymmetric transmission in ultrathin 90°-twisted Babinet-inverted metasurfaces*, Phys. Rev. B **89**, 165128 (2014).

1.66 L. Yahong, Z. Xin, S. Kun, W. Mei, and Z. Xiaopeng, *Ultrathin planar chiral metasurface for controlling gradient phase discontinuities of circularly polarized waves*, J. Phys. D Appl. Phys. **48**, 365301 (2015).

1.67 Y. Montelongo, J. O. Tenorio-Pearl, W. I. Milne, and T. D. Wilkinson, *Polarization Switchable Diffraction Based on Subwavelength Plasmonic Nanoantennas*, Nano Lett. **14**, 294-298 (2014).

1.68 M. Farmahini-Farahani, J. R. Cheng, and H. Mosallaei, *Metasurfaces nanoantennas for light processing*, J. Opt. Soc. Am. B-Opt. Phys. **30**, 2365-2370 (2013).

1.69 Q. Wang, et al., *Broadband metasurface holograms: toward complete phase and amplitude engineering*, Sci. Rep. **6**, 32867 (2016).

1.70 F. Huang, et al., *Zero-Reflectance Metafilms for Optimal Plasmonic Sensing*, Adv. Opt. Mater. **4**, 328-335 (2016).

1.71 K. Kumar, et al., *Printing colour at the optical diffraction limit*, Nat. Nano. **7**, 557-561 (2012).

1.72 Y. K. R. Wu, A. E. Hollowell, C. Zhang, and L. J. Guo, *Angle-Insensitive Structural Colours based on Metallic Nanocavities and Coloured Pixels beyond the Diffraction Limit*, Sci. Rep. **3**, 01194 (2013).

1.73 T. Xu, Y. K. Wu, X. G. Luo, and L. J. Guo, *Plasmonic nanoresonators for high-resolution colour filtering and spectral imaging*, Nat. Commun. **1**, 1058 (2010).

1.74 L. Duempelmann, A. Luu-Dinh, B. Gallinet, and L. Novotny, *Four-Fold Color Filter Based on Plasmonic Phase Retarder*, Acs Photonics **3**, 190–196 (2015).

1.75 Y. Montelongo, et al., *Plasmonic nanoparticle scattering for color holograms*, P. Natl. Acad. Sci. USA **111**, 12679-12683 (2014).

1.76 P. Mandal, S. A. Ramakrishna, R. Patil, and A. V. Gopal, *Polarization dependent color switching by extra-ordinary transmission in H-slit plasmonic metasurface*, J. Appl. Phys. **114**, 224303 (2013).

1.77 O. Eisenbach, O. Avayu, R. Ditcovski, and T. Ellenbogen, *Metasurfaces based dual wavelength diffractive lenses*, Opt. Express. **23**, 3928-3936 (2015).

1.78 M. Svedendahl, P. Johansson, and M. Käll, *Complete Light Annihilation in an Ultrathin Layer of Gold Nanoparticles*, Nano Lett. **13**, 3053-3058 (2013).

1.79 Y. Yao, et al., *Electrically Tunable Metasurface Perfect Absorbers for Ultrathin Mid-Infrared Optical Modulators*, Nano Lett. **14**, 6526-6532 (2014).

1.80 G. Li, et al., *Continuous control of the nonlinearity phase for harmonic generations*, Nat. Mater. **14**, 607-612 (2015).

1.81 J. X. Li, et al., *Optical Polarization Encoding Using Graphene-Loaded Plasmonic Metasurfaces*, Adv. Opt. Mater. **4**, 91-98 (2016).

1.82 S. F. Shi, et al., *Optimizing Broadband Terahertz Modulation with Hybrid Graphene/Metasurface Structures*, Nano Lett. **15**, 372-377 (2015).

1.83 S. H. Mousavi, et al., *Inductive Tuning of Fano-Resonant Metasurfaces Using Plasmonic Response of Graphene in the Mid-Infrared*, Nano Lett. **13**, 1111-1117 (2013).

1.84 J. Y. Chin, et al., *Nonreciprocal plasmonics enables giant enhancement of thin-film Faraday rotation*, Nat. Commun. **4**, 1599 (2013).

1.85 D. Floess, et al., *Tunable and switchable polarization rotation with non-reciprocal plasmonic thin films at designated wavelengths*, Light-Sci Appl **4**, e284 (2015).

1.86 M. Ferrera, et al., *Dynamic nanophotonics [Invited]*, J. Opt. Soc. Am. B **34**, 95-103 (2016).

1.87 M. U. Augustine, et al., *Roadmap on optical metamaterials*, J. Opt. **18**, 093005 (2016).

1.88 W. Ye, et al., *Spin and wavelength multiplexed nonlinear metasurface holography*, Nat. Commun. **7**, 11930 (2016).

1.89 M. Tymchenko, et al., *Gradient Nonlinear Pancharatnam-Berry Metasurfaces*, Phys. Rev. Lett. **115**, 207403 (2015).

1.90 I. Staude, et al., *Tailoring Directional Scattering through Magnetic and Electric Resonances in Subwavelength Silicon Nanodisks*, ACS Nano **7**, 7824-7832 (2013).

1.91 S. Kruk, et al., *Invited Article: Broadband highly efficient dielectric metadevices for polarization control*, APL Photonics **1**, 030801 (2016).

1.92 A. Arbabi, Y. Horie, M. Bagheri, and A. Faraon, *Dielectric metasurfaces for complete control of phase and polarization with subwavelength spatial resolution and high transmission*, Nat. Nano. **10**, 937-943 (2015).

1.93 A. Arbabi, Y. Horie, A. J. Ball, M. Bagheri, and A. Faraon, *Subwavelength-thick lenses with high numerical apertures and large efficiency based on high-contrast transmitarrays*, Nat. Commun. **6**, 8069 (2015).

1.94 A. Arbabi, R. M. Briggs, Y. Horie, M. Bagheri, and A. Faraon, *Efficient dielectric metasurface collimating lenses for mid-infrared quantum cascade lasers*, Opt. Express **23**, 33310-33317 (2015).

1.95 S. M. Kamali, A. Arbabi, E. Arbabi, Y. Horie, and A. Faraon, Decoupling optical function and geometrical form using conformal flexible dielectric metasurfaces, Nat. Commun. **7**, 11618 (2016).

1.96 M. I. Shalaev, et al., *High-Efficiency All-Dielectric Metasurfaces for Ultracompact Beam Manipulation in Transmission Mode*, Nano Lett. **15**, 6261-6266 (2015).

1.97 F. Aieta, M. A. Kats, P. Genevet, and F. Capasso, *Multiwavelength achromatic metasurfaces by dispersive phase compensation*, Science **347**, 1342-1345 (2015).

1.98 M. Khorasaninejad, et al., *Achromatic Metasurface Lens at Telecommunication Wavelengths*, Nano Lett. **15**, 5358-5362 (2015).

1.99 D. Lin, P. Fan, E. Hasman, and M. L. Brongersma, *Dielectric gradient metasurface optical elements*, Science **345**, 298-302 (2014).

1.100 M. Khorasaninejad, et al., *Metalenses at visible wavelengths: Diffraction-limited focusing and subwavelength resolution imaging*, Science **352**, 1190-1194 (2016).

1.101 Q. Wang, et al., *Optically reconfigurable metasurfaces and photonic devices based on phase change materials*, Nat. Photon. **10**, 60-65 (2016).

1.102 M. A. Kats, et al., *Ultra-thin perfect absorber employing a tunable phase change material*, Appl. Phys. Lett. **101**, 221101 (2012).

Chapter 2 Geometric phase and geometric metasurfaces

A variety of metasurfaces based on different operating mechanisms have been introduced in chapter 1. In this chapter, we will focus on geometric metasurfaces, which are the basis for the main body of the thesis. Geometric metasurfaces depend on geometric phases picked up through helicity reversion of the scattered light in comparison with that of the incident light. A geometric metasurface composed of anisotropic nanoantennas with spatially varying orientations can control the wavefront precisely with high fabrication tolerance.

2.1 Introduction to the geometric phase

Geometric phase in optics originates from the coupling between intrinsic angular momentum and rotations of coordinates [2.1]. The most studied manifestations of geometric phase are spin-redirection phase and Pancharatnam-Berry (P-B) phase [2.1]. If a beam of circularly polarized light propagates along curvilinear trajectories and returns to its initial propagation direction, its phase will be different from the value of $\int \boldsymbol{k}d\boldsymbol{l}$, where $\boldsymbol{k}$ is the wave vector, and $\boldsymbol{l}$ is the trajectory. The extra phase is named spin redirection geometric phase. On the other hand, P-B phase arises from transformations of the polarization state. In this section, we will concentrate on a specific P-B phase, which is generated when a circularly polarized light beam has its helicity reversed. The detailed analysis about the specific P-B phase is shown in references [2.2] and [2.3]. Here in this chapter, we adopt an effective method, which is based on the Jones calculus to reveal the specific P-B phase.

First, an anisotropic scatterer is assumed to have the transmission coefficients T_{o} and T_{e} along the *x*- and *y*- directions, respectively. If the scattered light has no cross-coupling between the two directions, a Jones matrix can be used to represent the polarization conversion property of the scatterer

$$T_0 = \begin{bmatrix} T_{\mathrm{o}} & 0 \\ 0 & T_{\mathrm{e}} \end{bmatrix} \tag{2.1}$$

In general, when the scatterer is rotated around the *z*- direction to an arbitrary direction φ, its Jones matrix changes to

$$T(\varphi) = J(-\varphi)T_0J(\varphi) \tag{2.2}$$

With the rotation matrix

$$J(\varphi) = \begin{bmatrix} \cos(\varphi) & \sin(\varphi) \\ -\sin(\varphi) & \cos(\varphi) \end{bmatrix} \tag{2.3}$$

If the rotated scatterer is under the illumination of the LCP light that has the normalized Jones vector

$$\tilde{L} = \frac{1}{\sqrt{2}}\begin{bmatrix}1\\ i\end{bmatrix} \tag{2.4}$$

The transmitted electric field E_t is written as

$$E_{t-LCP} = T(\varphi)\tilde{L} = \frac{T_o+T_e}{2}\tilde{L} + \frac{T_o-T_e}{2}e^{i2\varphi}\tilde{R} \tag{2.5}$$

where $\tilde{R}$ represent the Jones vector of the RCP light

$$\tilde{R} = \frac{1}{\sqrt{2}}\begin{bmatrix}1\\ -i\end{bmatrix} \tag{2.6}$$

Similarly, with the RCP incident light, the transmitted field is

$$E_{t-RCP} = T(\varphi)\tilde{R} = \frac{T_o+T_e}{2}\tilde{R} + \frac{T_o-T_e}{2}e^{-i2\varphi}\tilde{L} \tag{2.7}$$

The first terms in equations (2.5) and (2.7) represent the transmitted light with the same helicity of the incident light. The second terms represent the transmitted light that has the different helicity and a P-B phase of $\pm 2\varphi$.

2.2. Scattering properties of a single nanorod and the transmission-type geometric metasurface

One of the key steps to utilize geometric phase as shown in equations (2.5) and (2.7) is to find a proper anisotropic scatterer as mentioned in the last section. Here, we consider a simple but effective anisotropic scatterer, which is a silver rectangular nanorod located on a glass substrate [figure 2.1(a)]. The nanorod has a size much smaller than the operating wavelength. Hence a quasi-static approximation is utilized to analyze the electric field both inside and outside the nanorod [2.4]. If the incident light is polarized along the long (short) axis of the silver nanorod, the electric potential outside the nanorod is the superposition of the applied field and that of an electric dipole located at the rod center. The direction of the electric dipole is parallel to the long (short) axis of the nanorod.

If the incident light has nonzero components along both axes of the nanorod, two dipole moments with perpendicular directions are generated [figures 2.1(b) and (c)]. Due to the different resonance conditions along the two axes, the two dipole moments have different magnitudes, and therefore the nanorod can be regarded as an anisotropic scatterer. Since the value of geometric phase is solely determined by the orientation of the nanorod [equations (2.5) and (2.7)], it is possible to encode a sampled phase

function to an array of nanorods with different orientations, which form a geometric metasurface (figure 2.2).

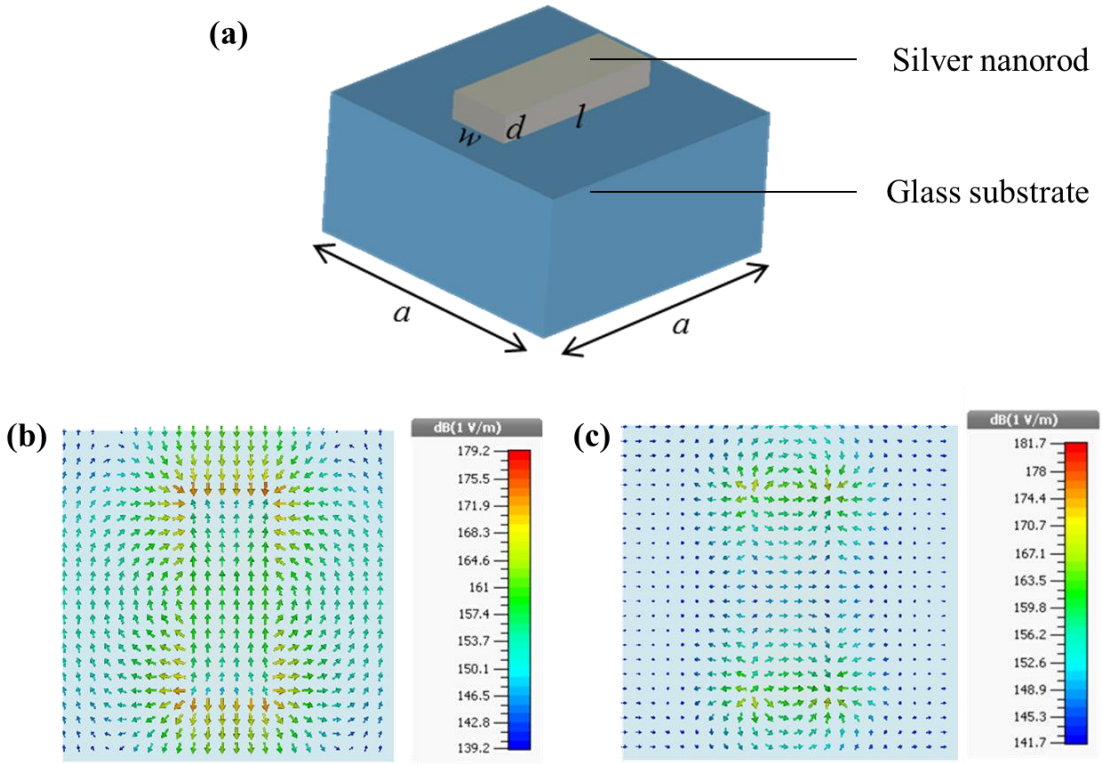

Figure 2.1 Schematic of a rectangular nanorod and its dipole model. (a) A silver rectangular nanorod is located on the glass substrate. The parameters *l*, *w* and *d* represent the length, width and thickness of the nanorod. The pixel pitch is *a*. The parameters are set as follows: *l*=220 nm, *w*=90 nm, *d*=30 nm and *a*=350 nm. The electric field around the nanorod is simulated if the incident light is polarized along its (b) long axis and (c) short axis. The incident light has the wavelength of 926 nm for (b) and 528 nm for (c). The result is obtained using finite difference time domain (FDTD) method. The amplitude of the incident light is set to be 1V/m in both (b) and (c).

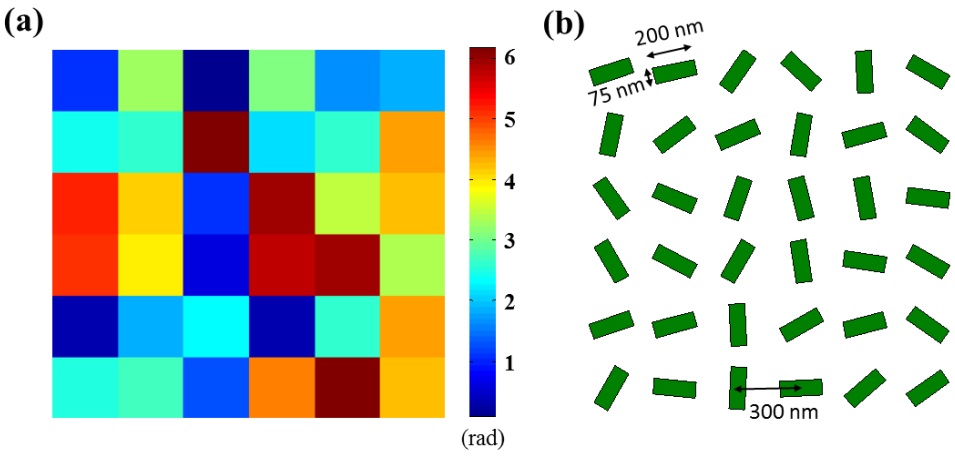

Figure 2.2 The encoding process of a geometric metasurface. (a) A random phase profile with 6×6 pixels. The color of each pixel denotes its phase value. (b) The phase profile in figure (a) is represented by an array of nanorods with different orientations.

The conversion efficiency of a metasurface denotes its ability to change the incident circularly polarized light into the light with opposite helicity. As shown in equations (2.5) and (2.7), the conversion efficiency is determined by the transmission coefficients T_o and T_e of a single nanorod, which can be written as

$$\eta_{\text{convert}} = \frac{|T_o - T_e|^2}{4} \tag{2.8}$$

The parameters T_o and T_e are related to the geometry of the nanorod (l, w, d), pixel pitch a, and its component material. In figure 2.3, η_{convert} is simulated for several specific examples, where the nanorods have different widths and component materials. When the nanorod width is increased, the peak of an efficiency curve will be blue-shifted. For the silver and gold nanorods of the same geometry, the efficiency peak of the former is located at a shorter wavelength than that of the latter.

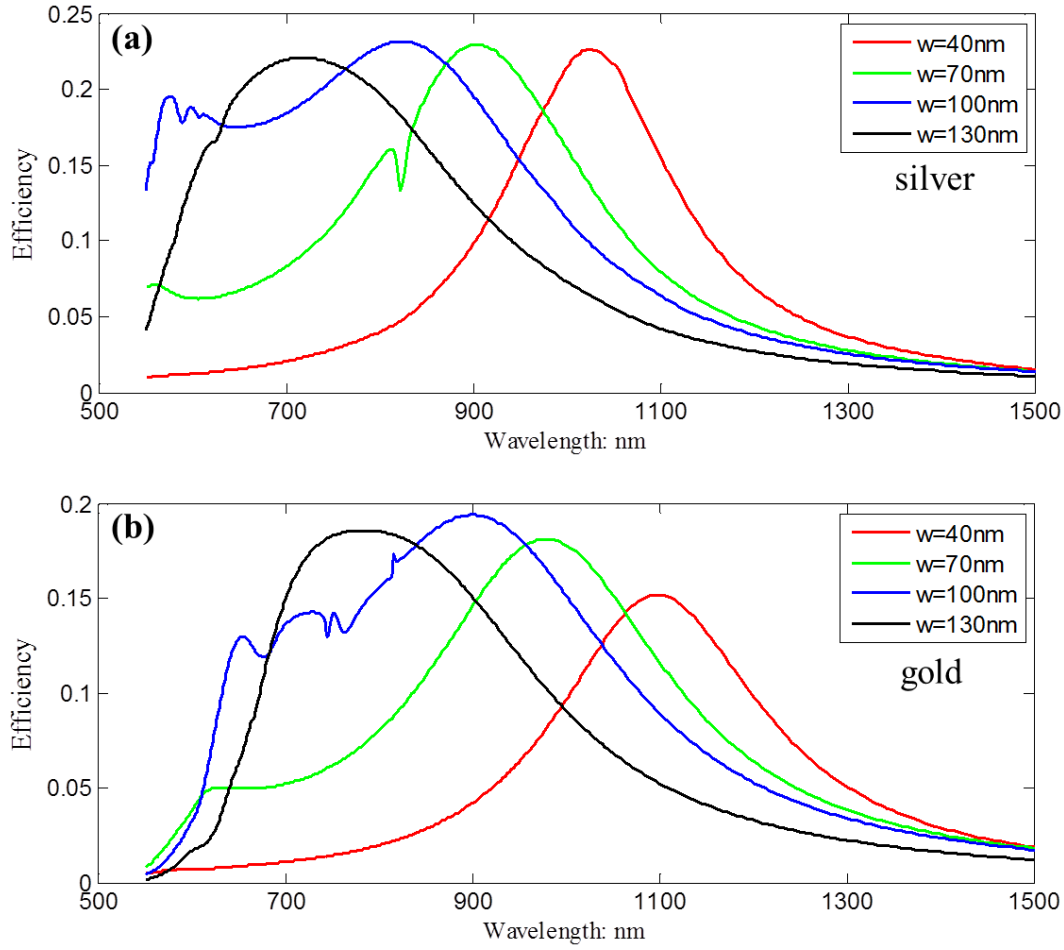

Figure 2.3 Simulated conversion efficiency of the metasurface. The four efficiency curves in each figure correspond to four different metasurfaces, whose nanorods have the widths of 40 nm, 70 nm, 100 nm and 130 nm, respectively. The nanorods of different metasurfaces have the same length of 200 nm, the thickness of 30 nm and the pixel pitch of 300 nm. The component material is silver in (a), and gold in (b).

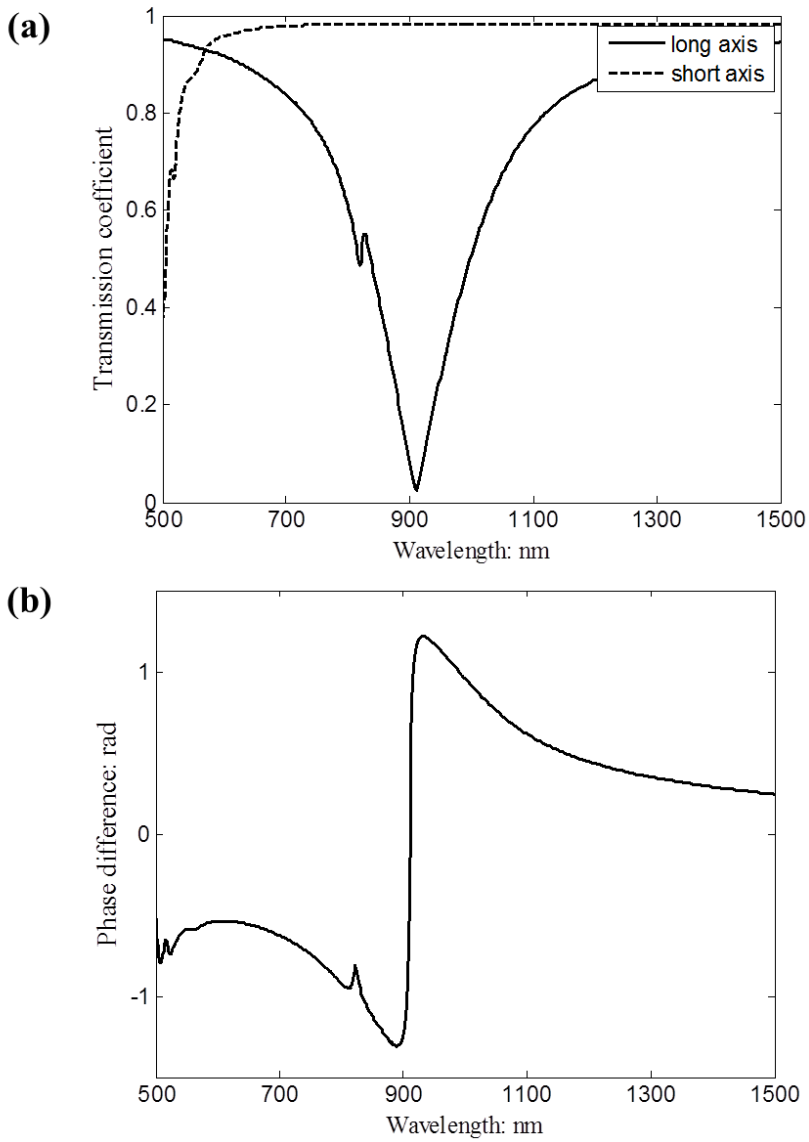

Figure 2.4 Simulated scattering properties of a single silver nanorod. The nanorod is 200 nm long, 70 nm wide and 30 nm thick. The pixel pitch is 300 nm. (a) The transmission coefficients of the light polarized along the long and short axes of the nanorod. (b) The phase difference between the two cross-polarized light beams scattered by the nanorod.

It should be noted that the conversion efficiency of the transmission-type geometric metasurface composed of a single layer of metallic nanorods is relatively low (figure 2.3). To get higher conversion efficiency, the scattered light without geometric phase has to be eliminated, meaning that

$$T_{\mathrm{o}} + T_{\mathrm{e}} = 0 \tag{2.9}$$

For a rectangular metallic nanorod, the equation (2.9) can be interpreted as

$$|T_{\mathrm{o}}| = |T_{\mathrm{e}}| \tag{2.10}$$

$$\arg(T_{\mathrm{o}}) - \arg(T_{\mathrm{e}}) = \pm\pi \tag{2.11}$$

Equations (2.10)-(2.11) imply that a nanorod should work as a half-wave plate with the fast axis along its long or short axis. However, this goal cannot be achieved for the following reasons: First, $|T_o|$ does not equal to $|T_e|$ in most of the wavelength range of interest due to the different resonance conditions along the two axes of the nanorod [figure 2.4(a)]. Second, the phase difference between T_o and T_e cannot reach π as shown in figure 2.4(b).

2.3 The reflection-type geometric metasurface

In order to boost the conversion efficiency of the metasurface, a three-layer structure can be applied as shown in figure 2.5. The antenna layer, along with the dielectric spacer and the metallic reflective layer compose a Fabry-Pérot-like cavity. The high efficiency arises from the interplay of the antenna resonance and the cavity effect of the multilayer structure. Several different theoretical models have been proposed to illustrate the high efficiency and broadband performance of the metasurface. Grady [2.5] calculated the amplitude of the co- and cross-polarized reflected light after each round trip in the cavity. After multiple reflections, the superposition of all the cross-polarized light results in a constructive interference, while the co-polarized light forms a deconstructive interference. Jiang [2.6] pointed out that the metallic ground layer acts as a perfect mirror. The light reflected from the ground layer can be regarded as the mirror image of the incident light together with the radiation of the mirror image of the metallic structure. Then the total reflection is the superposition of all components of light propagating along the surface normal. The dispersion of the metallic nanoantennas is canceled out by that of the dielectric spacing layer, which yields a dispersionless performance. Zheng [2.7] proposed a multi-beam interference model to illustrate the high efficiency and broadband property of the reflection-type metasurface. Although the interference model is commonly used to analyze traditional Fabry-Pérot cavities, it is effective to link the conversion efficiency of the metasurface with the scattering parameters of the nanorod layer.

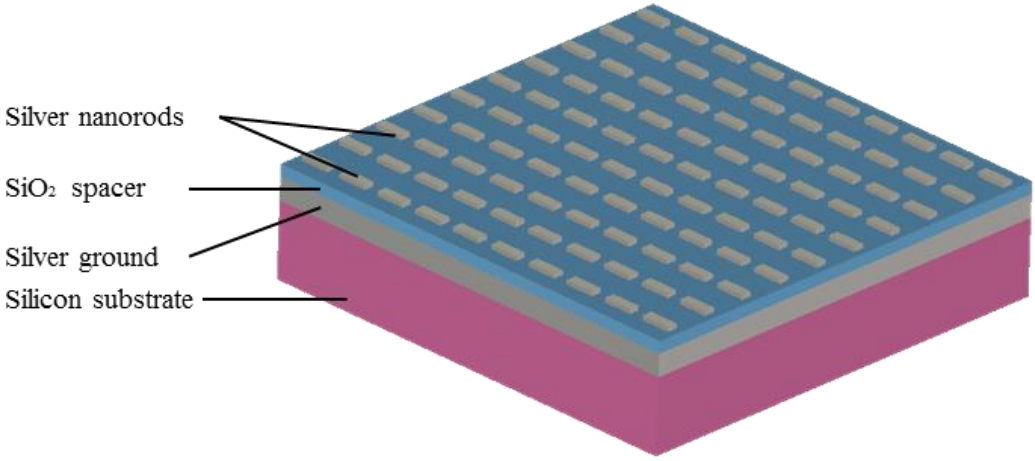

Figure 2.5 Schematic of the reflection-type metasurface. The metasurface is composed of three layers: the silver nanorods on the top, the SiO_2 spacer in the middle and the silver ground layer on the silicon substrate. All the silver nanorods are assumed to have the same orientation for simplicity.

Although gold is chosen to be the component material in references [2.5-2.7], silver is used here since it has less absorptions of blue and green light. Therefore it turns to be a better candidate for the visible range. As shown in figure 2.5, we consider a reflection-type metasurface with nanorods of uniform orientations for simplicity. The silver nanorod layer can be regarded as a homogeneous but anisotropic layer. According to the multi-beam interference model [2.7], the conversion efficiency of the metasurface is determined by the refractive indices and thicknesses of the nanorod layer and the SiO_2 spacer, and the reflection coefficient of the silver ground layer.

We first link the refractive index of the nanorod layer with the scattering properties of the nanorods. The case when the incident light has a polarization parallel to the long axis of a nanorod is first considered, and the subscript letter L is added to the related parameters thereby. For a certain volume in the material Δv that carries a dipole moment Δp_L, the polarization density P_L has the expression [2.7]

$$P_L = \frac{\Delta p_L}{\Delta v} = \frac{\varepsilon_0 \alpha_{eL} E_L}{a^2 h} \tag{2.12}$$

The parameter a is the pixel pitch and h represents the height of the nanorod layer. The expression a^2h denotes the average volume of a single pixel in the nanorod layer. α_{eL} is the polarizability of a nanorod along its long axis. ε_0 represents the permittivity of free space, and E_L is the electric field polarized along the long axis of the nanorod. From classical electromagnetics, P_L also has the definition of

$$P_L = \chi_{eL} \varepsilon_0 E_L \tag{2.13}$$

where χ_{eL} is the susceptibility of the medium. In comparison with equation (2.12), χ_{eL} can be written as

$$\chi_{eL} = \frac{\alpha_{eL}}{a^2 h} \tag{2.14}$$

The relative permittivity ε_L of the nanorod layer is

$$\varepsilon_L = 1 + \chi_{eL} \tag{2.15}$$

Therefore the refractive index of the nanorod layer is written as

$$n_L = \sqrt{\varepsilon_L} = \sqrt{1 + \frac{\alpha_{eL}}{a^2 h}} \tag{2.16}$$

Similarly, we have n_S when the incident light has a polarization parallel to the short axis of a nanorod

$$n_S = \sqrt{\varepsilon_S} = \sqrt{1 + \frac{\alpha_{eS}}{a^2 h}} \tag{2.17}$$

Equations (2.16)-(2.17) show that the refractive indices of the nanorod layer n_L and n_S are determined by the parameters α_{eL}, α_{eS}, a and h. Since α_{eL} and α_{eS} are related to the geometry of the nanorod (length l, width w, and height h) and the pixel pitch a, it means that n_L and n_S are both determined by l, w, h and a.

When the incident light impinges normally onto a nanorod layer, the transmitted light passes through the SiO_2 spacer and is reflected back by the silver ground layer. The reflected light keeps on stimulating the nanorod to generate the light beam carrying geometric phase. Therefore the thickness of the SiO_2 spacer layer d_{spacer} is important to provide constructive interference condition for the output beam. The refractive index of the SiO_2 spacer n_{spacer} is known; hence d_{spacer} is the only parameter of the SiO_2 spacer to be considered.

The silver ground layer has a thickness of 150 nm, which is thick enough to make sure that no light is transmitted, and the reflection coefficient of the silver ground layer can be obtained from literature values.

We first study the air-nanorod-SiO_2 structure with the assumption that there are no silver ground layer and the silicon substrate in figure 2.5. If a beam of light is polarized along the long axis of the nanorod and it is incident from the air side, the transmission coefficient t_L and the reflection coefficient r_L can be found in the reference [2.8], which are the functions of n_L, n_{spacer} and h. If the light is incident from the SiO_2 side, the transmission and reflection coefficients are written as t'_L and r'_L, respectively. Similarly, we can get t_S, r_S, t'_S and r'_S, which are valid for the light polarized along the short axis of

the nanorod. Next we take the silver ground layer into consideration, and the reflection coefficient for the light polarized along the long axis of the nanorod can be written as [2.7]

$$R_L = r_L + \frac{t_L t'_L |r_m| e^{i\alpha}}{1 - r'_L |r_m| e^{i\alpha}} \tag{2.18}$$

The parameter r_m is the reflection coefficient of the SiO_2/silver interface, and it can be easily calculated. The parameter α has the expression

$$\alpha = 2n_{\text{spacer}} k_0 d_{\text{spacer}} + \varphi(r_m) \tag{2.19}$$

k_0 is the wave vector of free space. $\varphi(r_m)$ is the phase of r_m. α represents the round-trip phase accumulated in the SiO_2 spacer. Similar to equation (2.18), the reflection coefficient for the light polarized along the short axis of the nanorod is

$$R_S = r_s + \frac{t_S t'_S |r_m| e^{i\alpha}}{1 - r'_S |r_m| e^{i\alpha}} \tag{2.20}$$

Based on equations (2.18-2.20), the conversion efficiency of the reflection-type metasurface is

$$\eta_{\text{convert}} = \frac{|R_L - R_S|^2}{4} \tag{2.21}$$

Equations (2.18)-(2.21) show that the conversion efficiency η_{convert} is related to the refractive indices and thickness of the nanorod layer through parameter set $\{t_L, r_L, t'_L, r'_L, t_S, r_S, t'_S, r'_S\}$, and η_{convert} is also related to d_{spacer}.

Instead of discussing the influence of n_L and n_S, h and d_{spacer} on the conversion efficiency, it can be written as a more straightforward way

$$\eta_{\text{convert}} = f\left(l, w, h, a, d_{\text{spacer}}\right) \tag{2.22}$$

For a metasurface with given configuration (l, w, h, a, d_{spacer}), it is possible to approximate α_{eL} and α_{eS} to Lorentzian forms with the aid of FDTD method. The analytical expression of η_{convert} versus the wavelengths of the incident light can be given by using the multilayer reflection model [2.7]. However, it is not practical to deduce a generalized expression of $f(l, w, h, a, d_{\text{spacer}})$ from which the optimum design of the metasurface can be calculated.

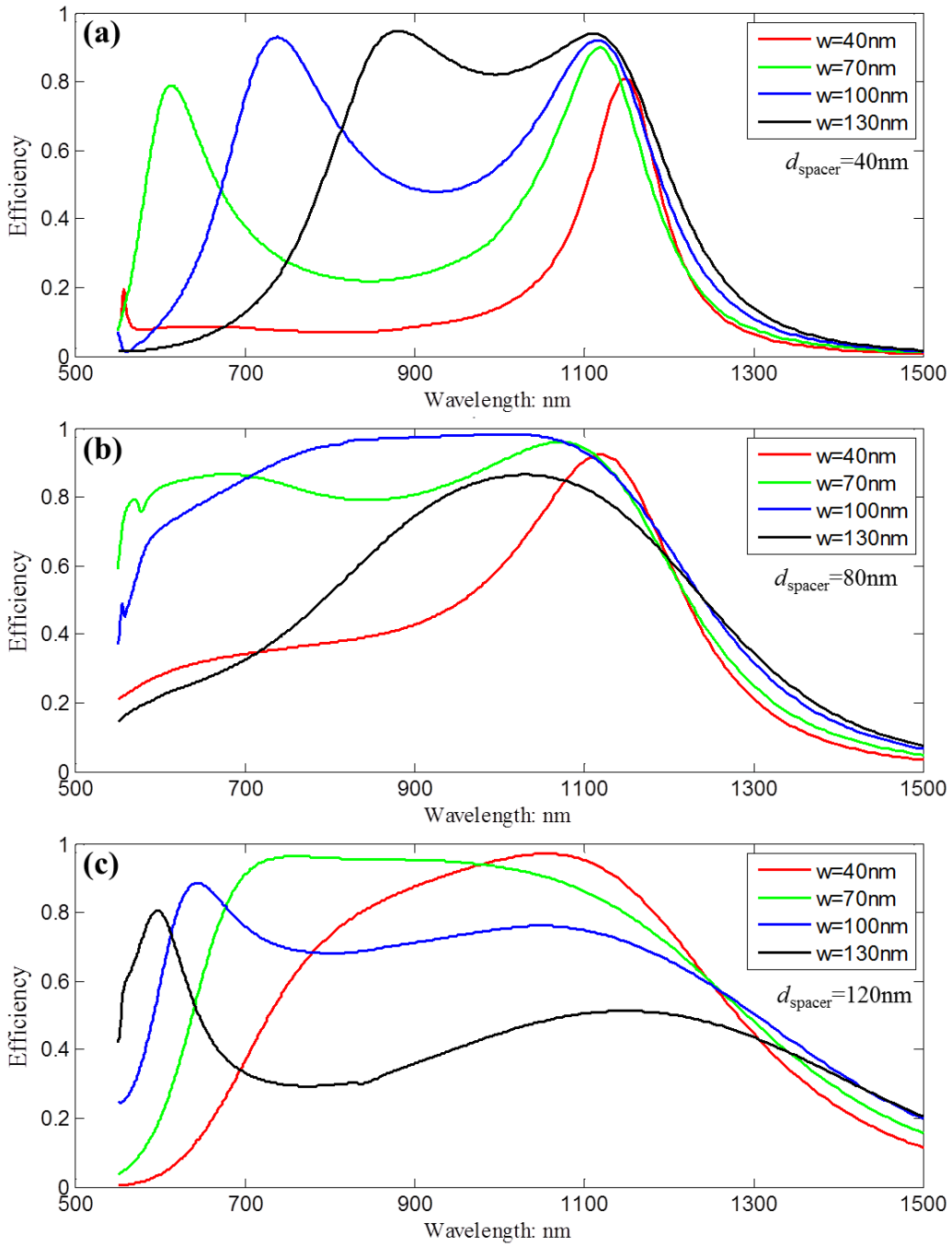

Figure 2.6 Simulated conversion efficiency of the reflection-type metasurfaces with silver nanorods. The four efficiency curves in each figure correspond to four different metasurfaces, whose nanorods have widths of 40 nm, 70 nm, 100 nm and 130 nm, respectively. The nanorods of different metasurfaces have the same length of 200 nm, the thickness of 30 nm and the pixel pitch of 300 nm. The thickness of the SiO_2 spacer is 40 nm in (a), 80 nm in (b) and 120 nm in (c).

In the following, the relationship between the conversion efficiency and the metasurface configuration parameters is analyzed, which aims to achieve a high efficiency and broadband performance. For simplicity, the length and thickness of a nanorod are set to be 200nm and 30 nm, respectively. The pixel pitch is fixed to be 300 nm. As shown in figure 2.6, the efficiency curve changes with the thickness of the SiO_2

spacer and the width of the nanorods. Since we are interested in the visible and near infrared range, the case when the nanorod width is within 70 to 100nm, and d_{spacer} equals to 80 nm is the best choice [blue and green curves in figure 2.6(b)]. With the increase of d_{spacer}, the efficiency is improved for the wavelengths longer than 1300 nm.

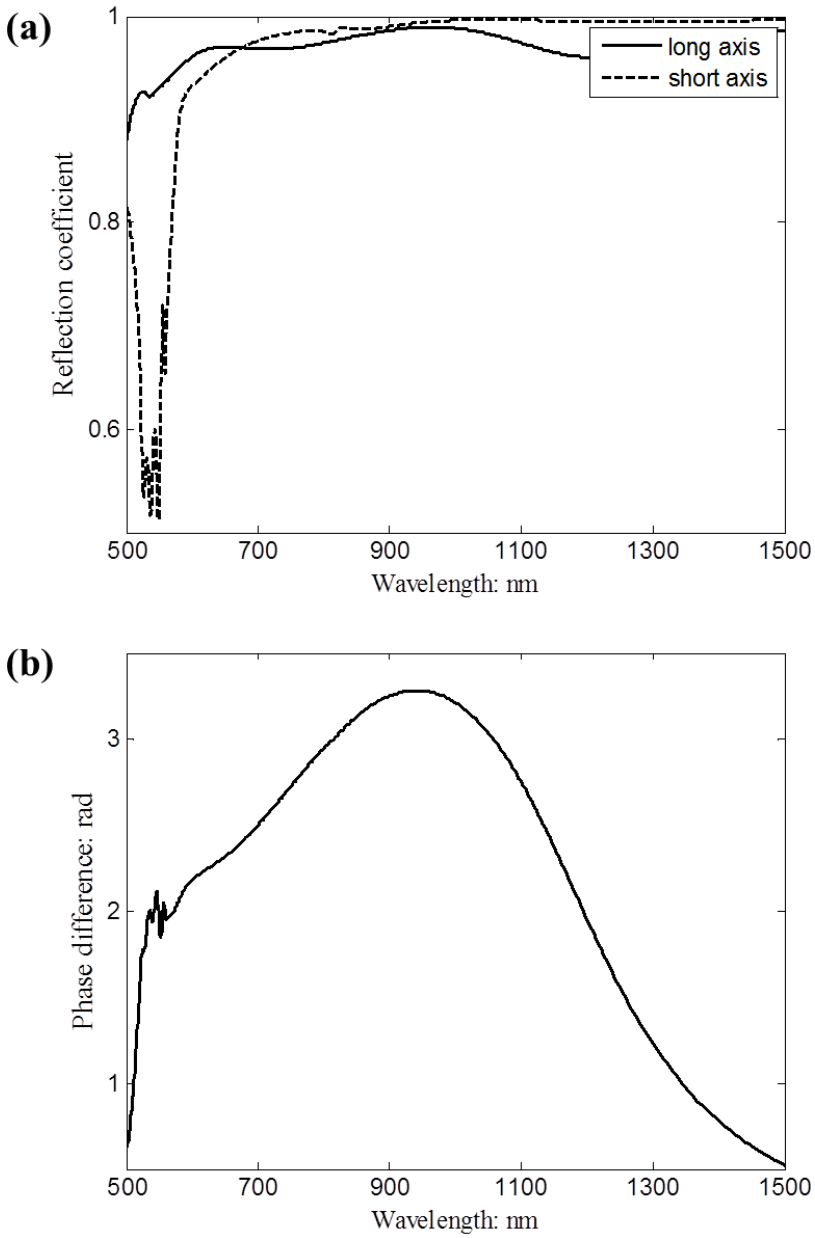

Figure 2.7 Simulated scattering properties of a silver nanorod in a reflection-type metasurface. The nanorod is 200 long, 100 nm wide and 30 nm thick. The pixel pitch is 300 nm, and the SiO_2 spacer is 80 nm. (a) The reflection coefficients of the light polarized along the long and short axes of the nanorod. (b) The phase difference between the two cross-polarized light beams scattered by the nanorod.

If the configuration parameters of the metasurface are chosen properly, each nanorod, in combination with the SiO_2 spacer and silver ground layer can form a broadband reflection-type half-wave plate, which accounts for the high efficiency and broadband performance. We simulate the reflection coefficients of the light beams

polarized along the long and short axes of the nanorod and the phase difference between them (figure 2.7). Figure 2.7 shows that the two cross-polarized light beams have roughly equal amplitude and a phase difference that approaches π in a wide operational bandwidth. In comparison with those of the transmission type metasurface (figure 2.4), the reflection type metasurface here is much closer to the function of a half waveplate. Alternatively, if the calculation results in figures 2.4 and 2.7 are both substituted into equation (2.8), it shows that the efficiency is much higher for the reflection type metasurface.

2.4 Conclusion

In this chapter, the geometric phase and the transmission/reflection-type geometric metasurfaces are introduced. Since the geometric phase is determined by the orientation angle of the anisotropic scatterer, the geometric metasurface can continuously tune the phase of the scattered light from 0 to 2π. As geometric phase is independent of the incident wavelengths, the geometric metasurface can work in the broad wavelength range. When the helicity of the incident light is reversed, the phase function of the geometric metasurface will be added to a minus sign, which gives rise to many new applications [2.9-2.12]. Above all, the distance between the neighboring nanorods can be sub-wavelength, and the thickness of the nanorods is only a few dozen nanometers, which makes the geometric metasurface a potential candidate for miniature optical devices.

2.5 References

2.1 K. Y. Bliokh, F. J. Rodriguez-Fortuno, F. Nori, and A. V. Zayats, *Spin-orbit interactions of light*, Nat. Photon. **9**, 796-808 (2015).

2.2 M. V. Berry, *The Adiabatic Phase And Pancharatnam Phase For Polarized Light*, J. Mod. Opt. **34**, 1401-1407 (1987).

2.3 L. L. Huang, et al., *Dispersionless Phase Discontinuities for Controlling Light Propagation*, Nano Lett. **12**, 5750-5755 (2012).

2.4 S. Maier, *Plasmonics Fundamentals and Applications*, Springer, New York (2007).

2.5 N. K. Grady, et al., *Terahertz Metamaterials for Linear Polarization Conversion and Anomalous Refraction*, Science **340**, 1304-1307 (2013).

2.6 S. C. Jiang, et al., *Controlling the Polarization State of Light with a Dispersion-Free Metastructure*, Phys. Rev. X **4**, 021026 (2014).

2.7 G. Zheng, et al., *Metasurface holograms reaching 80% efficiency*, Nat. Nano. **10**, 308-312 (2015).

2.8 M. Born and E. Wolf, *Principles of optics, seventh (expanded) edition*, Cambridge University Press, Cambridge (1999).

2.9 X. Chen, et al., *Longitudinal Multifoci Metalens for Circularly Polarized Light*, Adv. Opt. Mater., **3**, 1201-1206 (2015).

2.10 X. Z. Chen, et al., *Dual-polarity plasmonic metalens for visible light*, Nat. Commun. **3**, 2207 (2012).

2.11 D. D. Wen, F. Y. Yue, M. Ardron, and X. Z. Chen, *Multifunctional metasurface lens for imaging and Fourier transform*, Sci. Rep. **6**, 27628 (2016).

2.12 F. Yue, et al., *Vector Vortex Beam Generation with a Single Plasmonic Metasurface*, Acs Photonics **3**, 1558–1563 (2016).

Chapter 3 Phase gradient metasurface for polarization measurement

Polarization measurement system conventionally uses a series of polarizers and waveplates, which change the polarization of light over a distance much longer than the operating wavelengths. Here in this chapter, a phase gradient metasurface is utilized to realize the polarization measurement. The incident light is separated into two orthogonal circular components (LCP and RCP), and they are deflected to different directions. The ellipticity and helicity of the incident polarized light can be derived from the intensities of two components. Since the ultrathin metasurface offers unique advantages such as broadband, simplicity, and miniaturization, it shows the potential to simplify the experimental setup and improve the system integration dramatically.

3.1 Introduction

Polarization state measurement has found many applications [3.1], ranging from ellipsometry [3.2], remote sensing [3.3] to polarization light scattering [3.4] and ophthalmic polarimetry [3.5]. Miniaturization and integration of polarization measurement systems are necessary for their applications in integrated optical systems. However, since the conventional polarization elements rely on gradual polarization changes accumulated through propagation, the further reduction of the system volume is confronted with many challenges. Besides, as conventional waveplates are wavelength-sensitive, it is practically difficult to achieve the broadband polarization modulation.

Benefiting from the burgeoning field of metamaterials [3.6-3.12], much attention has been paid to the metamaterial-based polarization converting elements [3.13-3.16]. For example, metamaterials with artificial chirality may be used as circular polarizers [3.17-3.19] and polarization rotators [3.20-3.21]. Recently, two-dimensional metamaterials, or metasurfaces [3.22-3.24] show their unique ability in polarization manipulation, such as the conversion from a linear or circular polarization to its orthogonal one [3.23, 3.25-3.29]. Moreover, they can abruptly change the phase and polarization of light within a deep subwavelength range [3.30-3.31], which makes them potential candidates for miniature polarization measurement systems.

Here in this chapter, a phase gradient metasurface is adopted for the polarization measurement within a broad wavelength range. The metasurface is composed of an array of gold nanorods with varying orientations. For the incident light impinging normally onto the metasurface, part of it will be decomposed into the two orthogonal circular components and deflected to different directions. By measuring the intensities

of the two components, the polarization state of the incident light can be determined accordingly.

3.2 Design of the phase gradient metasurface

The designed metasurface is composed of an array of nanorods, which change their orientations along the *x*-direction, and the two neighboring nanorods have an orientation difference of $\pi/8$ [figure 3.1(a)]. In another view, eight nanorods form a supercell, and the supercell repeats in the *x*-direction to form the metasurface. The nanorods have the same length (200 nm), width (50 nm) and thickness (30 nm). The pixel pitch *s* equals to 400 nm. To fabricate the metasurface, a polymethyl methacrylate (PMMA) layer is first spin-coated onto the indium tin oxide (ITO) coated glass substrate. Then the nanorod structures are defined using electron-beam lithography and followed by the exposure and development processes. After that, a 30 nm thick gold film is deposited on the surface of the developed PMMA layer, and finally, a lift-off procedure is used to obtain the nanorods. The scanning electron microscope (SEM) image of the metasurface is shown in figure 3.1(b).

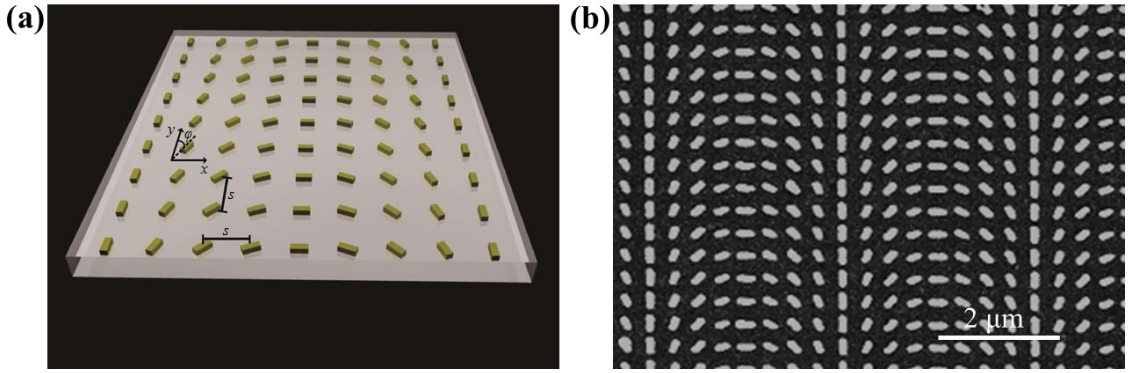

Figure 3.1 Schematic and SEM image of the phase gradient metasurface. (a) Schematic of the metasurface. The orientation angle φ is formed by the nanorod and the *y*-axis. The pixel pitch *s* equals to 400 nm. (b) SEM image of the fabricated metasurface [3.29].

As mentioned in chapter 2 [equations (2.5) and (2.7)], each nanorod can be regarded as an anisotropic scatterer, which decomposes the incident circularly polarized light into two parts [3.32]. The first part has the reversed helicity in comparison with the incident light, and it is given a geometric phase $\pm 2\varphi$ (the angle φ is shown in figure 3.1). The second part has the same helicity, and it is without the geometric phase. Therefore the metasurface proposed here is similar to a polarization grating [3.33], which operates in visible and near infrared wavelengths rather than that for far infrared and terahertz ranges [3.34-3.35]. When the LCP light impinges normally onto the phase gradient metasurface, the first part scattered light is RCP, which is given a geometric phase

gradient [figure 3.2(a)] and anomalously refracted to the right side of the incident light [figure 3.2(b)]. On the contrary, the second part scattered light is still LCP and is regularly refracted along the original direction of the incident light.

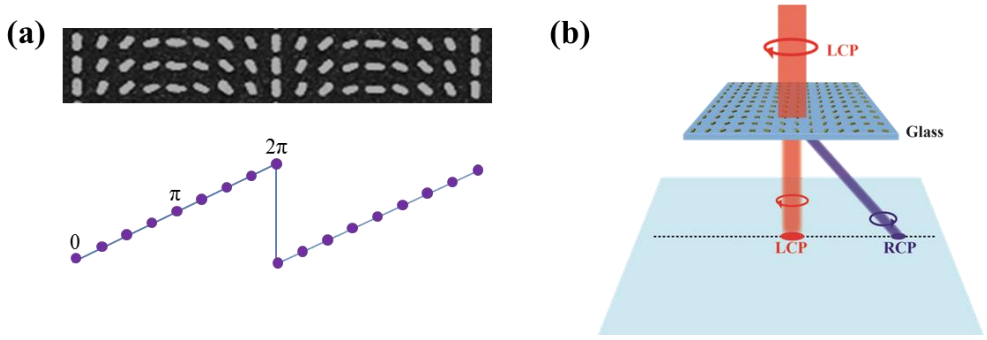

Figure 3.2 Schematic to show the case when the incident light is LCP. (a) The phase profile of the RCP refracted light. (b) The RCP refracted light is diverted to the right side of the metasurface due to the phase gradient. The LCP refracted light preserves the direction of the incident light for there is no phase gradient [3.29].

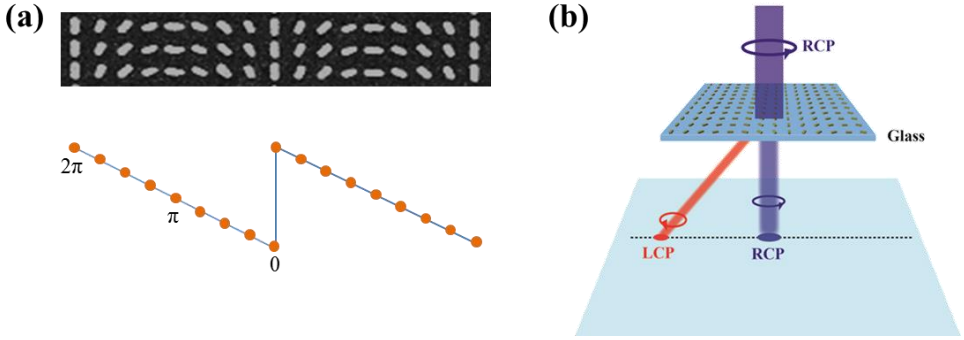

Figure 3.3 Schematic to show the case when the incident light is RCP. (a) The phase profile of the LCP refracted light. (b) Schematic to show the polarization and the propagation directions of the refracted light beams [3.29].

If the incident light is RCP, the phase gradient of the anomalously refracted LCP light is reversed in comparison with that in figure 3.2(a) [figure 3.3(a)]. Therefore the LCP refracted light is diverted to the left side because of the phase gradient [figure 3.3(b)]. When the incident is linearly or elliptically polarized that contains both RCP and LCP components, there will be anomalously refracted LCP and RCP light beams located on both sides of the metasurface (figure 3.4).

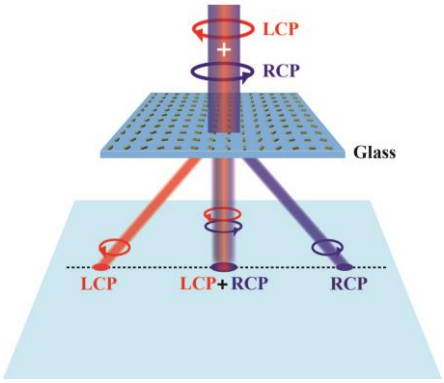

Figure 3.4 Schematic to show the case when the incident light is linearly or elliptically polarized [3.29].

By measuring the intensity ratio τ between the anomalously refracted RCP and LCP light, the intensity ratio between the LCP and RCP components of the incident light also equals to τ due to the helicity reversion

$$\frac{I_{LCP}}{I_{RCP}} = \tau \tag{3.1}$$

The ellipticity of the incident light is derived as

$$\eta = \frac{1-\sqrt{\tau}}{1+\sqrt{\tau}} \tag{3.2}$$

It can be deduced from equations (3.1)-(3.2) that the positive or negative sign of η denotes the helicity of the incident polarized light, with '+' and '-' representing the right and left-handedness, respectively. Especially, $\eta = \pm 1$ represents the pure RCP (LCP) light. For a linearly polarized light, we have $\eta = 0$.

3.3 Experimental characterization of the polarization measurement functionality

The experimental setup to characterize the polarization measurement functionality of the metasurface is shown in figure 3.5. The incident light comes from a continuous wave tunable laser (NKT, SuperK EXTREME supercontinuum), and its polarization state can be adjusted by a polarizer and a quarter- wave plate. The transmission axis of the polarizer is fixed while the fast axis of the quarter-wave plate is rotatable. Then the light is slightly shrunken by a lens and impinges normally onto the metasurface. An objective (10x/0.30 infinity corrected) and a lens are placed in the transmission side to collect the refracted light, including both the anomalously and regularly refracted parts. The image of the refracted light is captured by a CCD camera.

The damage threshold of the metasurface is related to the geometry and packing densities of the nanorods, the wavelength of the incident light, the repetition frequency and pulse duration of the pulsed laser source, and so on. It was reported that a

metasurface similar to figure 3.1 can work well under the 30 mW femtosecond (fs) laser (repetition frequency: 80MHz, pulse duration: 200 fs) [3.36]. In our experiment, the output power of the laser is about 0.5mW, which is much less than the damage threshold.

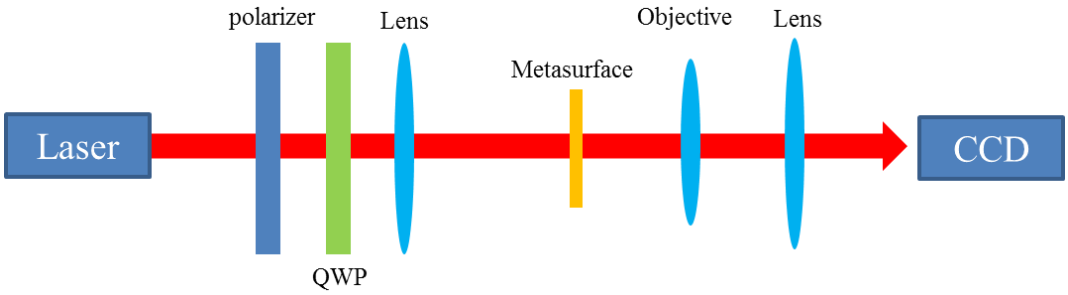

Figure 3.5 Schematic to show the experimental setup.

The incident light is first set to be RCP, and two light spots can be observed as shown in figure 3.6(a). The spot in the middle vanishes if we only collect the LCP refracted light by putting another quarter-wave plate and polarizer after the objective [figure 3.6(b)]. Therefore it proves that the middle and right light spots correspond to the regularly refracted RCP light and the anomalously refracted LCP light, respectively. Similarly, with the LCP incident light, the refracted light spots in the middle and on the left side are proved to be LCP and RCP, respectively [figures 3.6(c)-(d)]. For the linearly polarized incident light, three refracted light spots can be observed [figure 3.6(e)]. The two spots on both sides correspond to the anomalously refracted RCP and LCP light, while the one in the middle has the same linear polarization of the incident light [figure 3.6(f)].

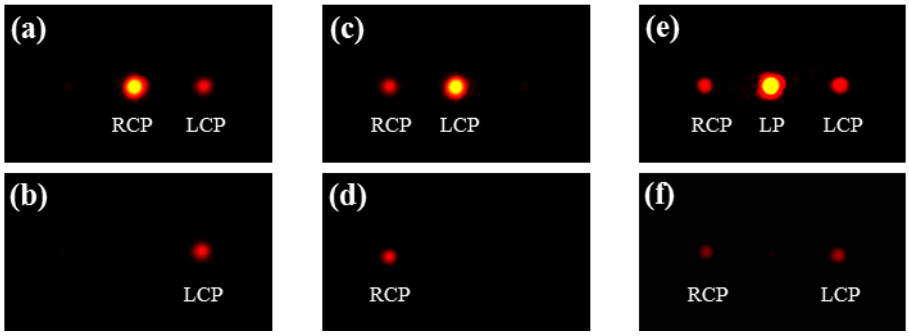

Figure 3.6 Verification of the polarization state of the refracted light at 633 nm. Images of the refracted light are obtained when the metasurface is illuminated by (a) RCP, (c) LCP and (e) linearly polarized light. If the refracted light with the same polarization of the incident light is filtered out, images (a), (c) and (e) change into (b), (d) and (f), respectively [3.29].

Figure 3.7 quantitatively shows the evolution of the anomalously refracted light versus the incident light polarization. A linearly polarized incident light contains equal RCP and LCP components; hence the anomalously refracted LCP and RCP light beams

have equal intensities [figure 3.7(a)]. When the incident light is left-handed elliptically polarized, the anomalously refracted RCP light has a higher intensity than that of the LCP light [figure 3.7(b)], and the latter disappears for pure LCP incident light [figure 3.7(c)]. Similarly, the cases for the right-hand elliptically polarized light and pure RCP light [figures 3.7(d) and (e)] can be understood in comparison with that in figures 3.7(b) and (c), respectively. Figure 3.7 clearly shows that the ellipticity and helicity of the incident light are closely related to the intensity ratio between the anomalously refracted RCP and LCP components.

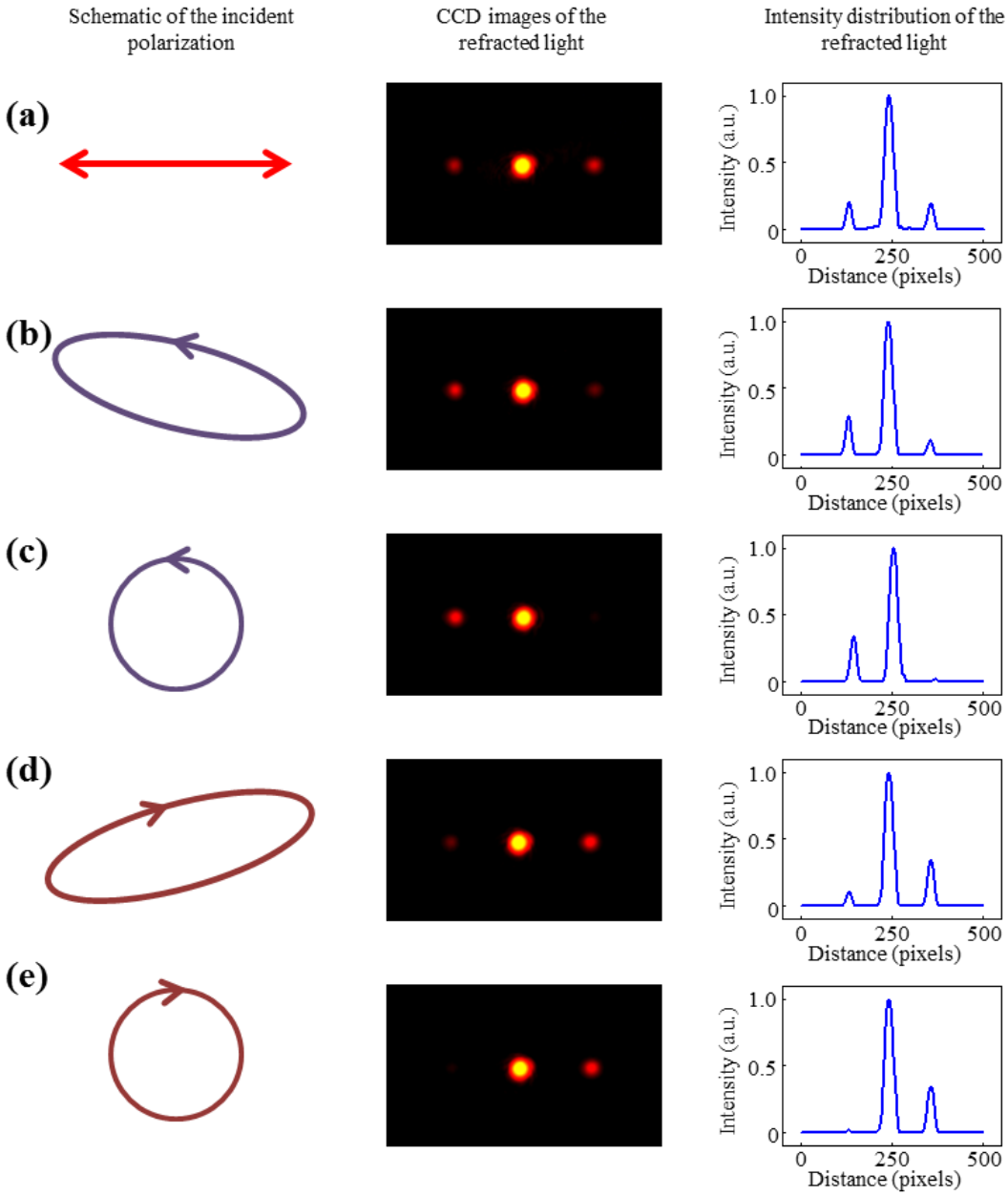

Figure 3.7 Intensity of the refracted light versus the incident light polarization. The left column shows the polarization ellipse of the incident light. The figures in the middle column are the images of the refracted light captured by the CCD cameras. The curves in the right column are the corresponding intensity values along a line that crosses the center of the light spots [3.29].

The efficiency of the metasurface for converting the incident circularly polarized light to its opposite helicity changes with wavelengths. However, the intensity ratio in equation (3.1) is dispersionless for a given incident polarization state, meaning that the method proposed in section 3.2 can work for a broad wavelength range. Here in this section, three different wavelengths are chosen as examples, and the ellipticity η is experimentally measured for different incident polarization states (figure 3.8). The experimental results show reasonable agreement with the prediction, which verifies the broadband performance of the proposed method.

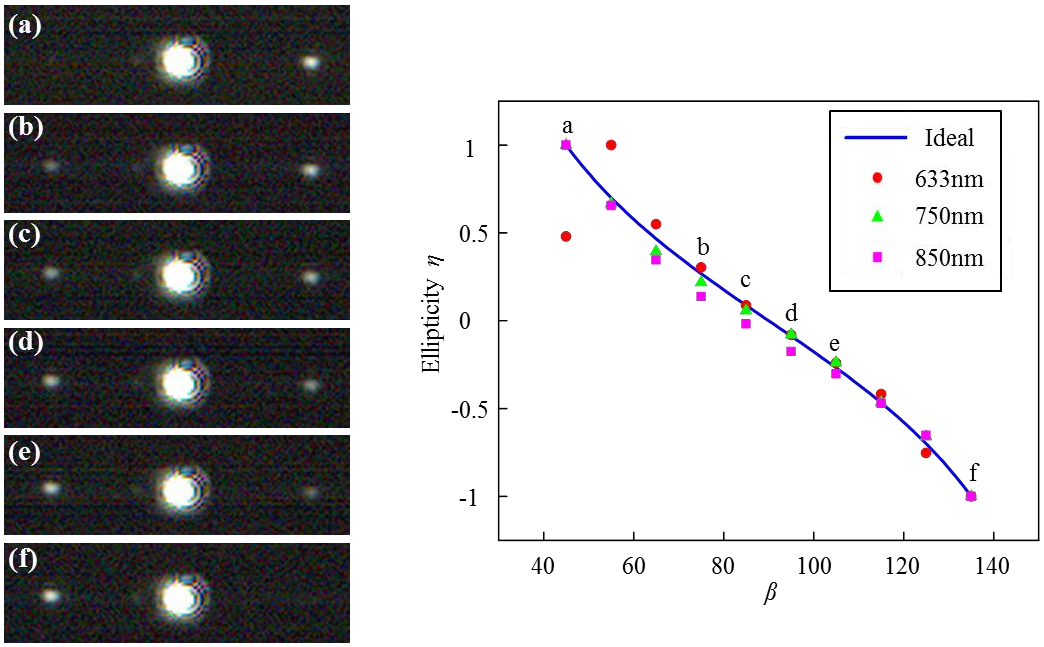

Figure 3.8 Measured ellipticity η for different incident polarization states and wavelengths. The polarization state of the incident light is changed by adjusting the value of β, which is the angle between the transmission axis of the polarizer (fixed along the horizontal direction) and the fast axis of the quarter-wave plate as shown in figure 3.5. The red circles, green triangles and pink squares represent the experimental results at 633 nm, 750 nm, and 850 nm, respectively. The blue curve represents the predicted relationship between η *and* β [3.29].

Besides the ellipticity and helicity, the azimuth angle of the polarization ellipse is needed to fully characterize the polarization of the incident light. As mentioned in section 3.2, the polarization state of the regularly refracted light is the same with that of the incident light. A polarizer can be deployed in front of the regularly refracted light, and the polarization azimuth angle can be detected by rotating the polarizer to find the maximum transmitted intensity. Here the polarization azimuth angles for different polarization states at 750 nm are experimentally measured, and the full polarization states are mapped onto the Poincaré sphere [figure 3.9]. The measurement process is without a quarter-wave plate, which usually cannot keep the π/2 phase retardance over a

broad wavelength range. Hence the polarization measurement method proposed here may facilitate the development of miniature and broadband polarization measurement systems.

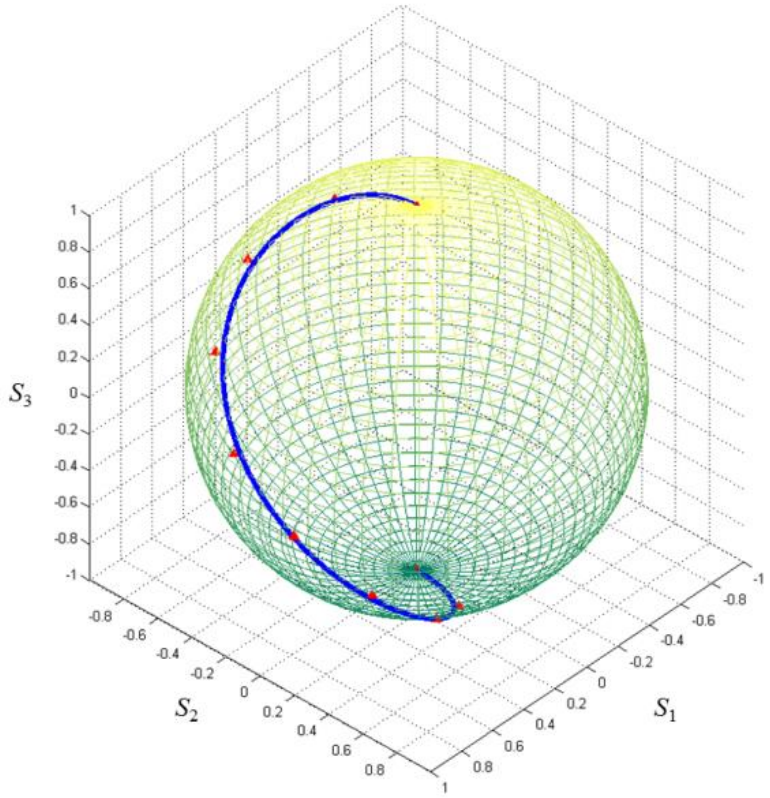

Figure 3.9 Full polarization state of the incident light at 750 nm. The azimuth angle of the polarization ellipse is measured and represented by ρ. Then the Stokes parameters S_1, S_2 and S_3 can be calculated by $S_1 = \cos2\chi\cos2\rho$, $S_2 = \cos2\chi\sin2\rho$, $S_3 = \sin2\chi$ with χ representing the arc tangent function of the ellipticity η. The solid line and the individual triangles represent the theoretical and experimental results, respectively. [3.29].

3.4 Discussion

As shown in figures 3.2-3.3, the phase profile of the anomalously refracted light has saw tooth shapes. Hence the refracted light from the metasurface has to follow

$$sin(\theta_{out}) - sin(\theta_{in}) = \sigma \frac{\lambda}{d} \tag{3.3}$$

Where d is the length of a supercell in the metasurface. θ_{in} and θ_{out} are the incident and refraction angles, respectively. λ represents the wavelength. $\sigma = \pm 1$ for the RCP and LCP refracted light. According to equation (3.3), the energy of the anomalously refracted RCP (LCP) light is concentrated in the direction θ_R (θ_L) by

$$dsin\theta_R = \lambda \tag{3.4}$$

and

$$-dsin\theta_L = \lambda \tag{3.5}$$

The angle formed by the two anomalously refracted light beams can be represented by

$$\alpha = \theta_R - \theta_L \tag{3.6}$$

Equations (3.4)-(3.6) denote that the split angle α changes with the incident wavelengths. From equation (3.6), it is not difficult to deduce that α has the value of 22.8° with the 633 nm incident light. α can also be measured as

$$\alpha = 2\arctan\left(\frac{d_2}{d_1}\right) \tag{3.7}$$

d_1 is the distance between the metasurface and the observation plane. d_2 is the distance between the anomalously refracted light spot and the regularly refracted light spot in the observation plane (figure 3.10). α is measured to be 22.6° at 633 nm, which agrees well with the prediction.

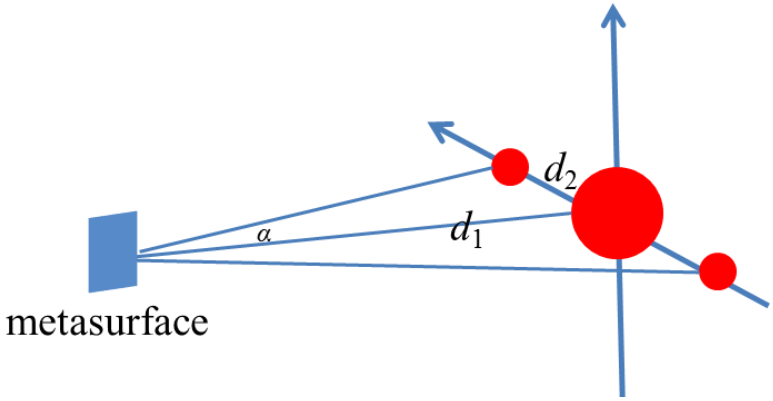

Figure 3.10 Measurement of the angle formed by the two anomalously refracted light beams.

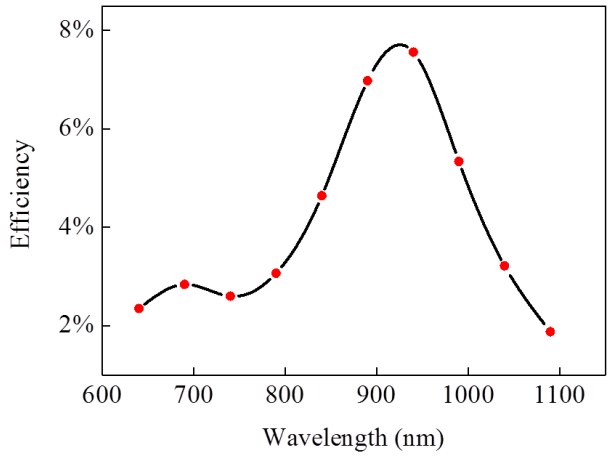

Figure 3.11 Conversion efficiency of the metasurface at different wavelengths. The red dots are the measured results [3.29].

Although the polarization measurement method proposed here can work for different wavelengths, its real operational bandwidth is limited by the conversion

efficiency, which is defined as the intensity ratio between the anomalously refracted light and the incident light. The experimentally measured conversion efficiency is shown in figure 3.11. The maximum conversion efficiency is located at 940 nm with the value of 7.6%. As the measurement accuracy can be boosted with the improvement of conversion efficiency, the reflection-type metasurface [3.37] proves to be a potential candidate to achieve a measurement system with higher performance.

3.5 Conclusion

In conclusion, a measurement method to determine the polarization state of a polarized light beam is demonstrated using phase gradient metasurface. By measuring the intensities of the anomalously refracted light beams, the ellipticity and the helicity of the incident light can be determined accordingly. The metasurface, along with a linear polarizer, can fully characterize the polarization state of the polarized light. In comparison with traditional polarization measurement systems, the device proposed in this chapter shows several advantages such as simplicity, miniaturization, and broadband, which may facilitate the development of integrated optical systems.

3.6 References

3.1 R. A. Chipman, *Polarimetry*, in *Handbook of Optics*. The McGraw Hill Companies, Inc.: New York, 2010.

3.2 A. Kasic, M. Schubert, S. Einfeldt, D. Hommel, and T. E. Tiwald, *Free-carrier and phonon properties of n- and p-type hexagonal GaN films measured by infrared ellipsometry*. Phys. Rev. B **62**, 7365–7377 (2000).

3.3 G. Vasile, E. Trouve, J. S. Lee, and V. Buzuloiu, *Intensity-driven adaptive-neighborhood technique for polarimetric and interferometric SAR parameters estimation*. IEEE Trans. Geosci. Remote Sens. **44**, 1609–1621 (2006).

3.4 X. Wang, J. Lai, and Z. Li, *Polarization studies for backscattering of RBC suspensions based on Mueller matrix decomposition*. Opt. Express **20**, 20771–20782 (2012).

3.5 A. Mistlberger, J. M. Liebmann, D. S. Greenfield, M. E. Pons, S. T. Hoh, H. Ishikawa, and R. Ritch, *Heidelberg retina tomography and optical coherence tomography in normal, ocular-hypertensive, and glaucomatous eyes*. Ophthalmology **106**, 2027–2032 (1999).

3.6 B. Edwards, A. Alù, M. G. Silveirinha, and N. Engheta, *Experimental verification of plasmonic cloaking at microwave frequencies with metamaterials*. Phys. Rev. Lett. **103**, 153901 (2009).

3.7 T. Ergin, N. Stenger, P. Brenner, J. B. Pendry, and M. Wegener, *Three-dimensional invisibility cloak at optical wavelengths*. Science **328**, 337–339 (2010).

3.8 N. Fang, H. Lee, C. Sun, and X. Zhang, *Sub-diffraction-limited optical imaging with a silver superlens*. Science **308**, 534–537 (2005).

3.9 R. A. Shelby, D. R. Smith, and S. Schultz, *Experimental verification of a negative index of refraction*. Science **292**, 77–79 (2001).

3.10 J. Valentine, S. Zhang, T. Zentgraf, E. Ulin-Avila, D. A. Genov, G. Bartal, and X. Zhang, *Three-dimensional optical metamaterial with a negative refractive index*. Nature **455**, 376–379 (2008).

3.11 V. M. Shalaev, *Optical negative-index metamaterials*. Nat. Photonics **1**, 41–48 (2007).

3.12 N. K. Grady, J. E. Heyes, D. R. Chowdhury, Y. Zeng, M. T. Reiten, A. K. Azad, A. J. Taylor, D. A. R. Dalvit, and H. T. Chen, *Terahertz metamaterials for linear polarization conversion and anomalous refraction*. Science **340**, 1304–1307 (2013).

3.13 V. A. Fedotov, P. L. Mladyonov, S. L. Prosvirnin, A. V. Rogacheva, Y. Chen, and N. I. Zheludev, *Asymmetric propagation of electromagnetic waves through a planar chiral structure*. Phys. Rev. Lett. **97**, 167401 (2006).

3.14 M. Kang, J. Chen, X. L. Wang, and H. T. Wang, *Twisted vector field from an inhomogeneous and anisotropic metamaterial*. J. Opt. Soc. Am. B **29**, 572–576 (2012).

3.15 C. Menzel, C. Helgert, C. Rockstuhl, E. B. Kley, A. Tünnermann, T. Pertsch, and F. Lederer, *Asymmetric transmission of linearly polarized light at optical metamaterials*. Phys. Rev. Lett. **104**, 253902 (2010).

3.16 S. Zhang, F. Liu, T. Zentgraf, and J. S. Li, *Interference-induced asymmetric transmission through a monolayer of anisotropic chiral metamolecules*. Phys. Rev. A **88**, 023823 (2013).

3.17 J. K. Gansel, M. Thiel, M. S. Rill, M. Decker, K. Bade, V. Saile, G. von Freymann, S. Linden, and M. Wegener, *Gold helix photonic metamaterial as broadband circular polarizer*. Science **325**, 1513–1515 (2009).

3.18 Y. Ye, X. Li, F. Zhuang, and S.-W. Chang, *Homogeneous circular polarizers using a bilayered chiral metamaterial*. Appl. Phys. Lett. **99**, 031111 (2011).

3.19 Y. Zhao, M. A. Belkin, and A. Alù, *Twisted optical metamaterials for planarized ultrathin broadband circular polarizers*. Nat. Commun. **3**, 870 (2012).

3.20 M. Decker, M. Ruther, C. E. Kriegler, J. Zhou, C. M. Soukoulis, S. Linden, and M. Wegener, *Strong optical activity from twisted-cross photonic metamaterials*. Opt. Lett. **34**, 2501–2503 (2009).

3.21 A. V. Rogacheva, V. A. Fedotov, A. S. Schwanecke, and N. I. Zheludev, *Giant gyrotropy due to electromagnetic-field coupling in a bilayered chiral structure*. Phys. Rev. Lett. **97**, 177401 (2006).

3.22 X. Ni, N. K. Emani, A. V. Kildishev, A. Boltasseva, and V. M. Shalaev, *Broadband light bending with plasmonic nanoantennas*. Science **335**, 427 (2012).

3.23 N. Yu, P. Genevet, M. A. Kats, F. Aieta, J. P. Tetienne, F. Capasso, and Z. Gaburro, *Light propagation with phase discontinuities: generalized laws of reflection and refraction*. Science **334**, 333–337 (2011).

3.24 S. Sun, Q. He, S. Xiao, Q. Xu, X. Li, and L. Zhou, *Gradient-index meta-surfaces as a bridge linking propagating waves and surface waves*. Nat. Mater. **11**, 426–431 (2012).

3.25 X. Chen, L. Huang, H. Mühlenbernd, G. Li, B. Bai, Q. Tan, G. Jin, C. W. Qiu, S. Zhang, and T. Zentgraf, *Dual polarity plasmonic metalens for visible light*. Nat. Commun. **3**, 1198 (2012).

3.26 L. L. Huang, X. Z. Chen, B. F. Bai, Q. F. Tan, G. F. Jin, T. Zentgraf, and S. Zhang, *Helicity dependent directional surface plasmon polariton excitation using a metasurface with interfacial phase discontinuity*. Light-Sci. Appl. **2**, e70 (2013).

3.27 L. Huang, X. Chen, H. Mühlenbernd, G. Li, B. Bai, Q. Tan, G. Jin, T. Zentgraf, and S. Zhang, *Dispersionless phase discontinuities for controlling light propagation*. Nano Lett. **12**, 5750–5755 (2012).

3.28 X. Z. Chen, L. L. Huang, H. Muehlenbernd, G. X. Li, B. F. Bai, Q. F. Tan, G. F. Jin, C. W. Qiu, T. Zentgraf, and S. Zhang, *Reversible three-dimensional focusing of visible light with ultrathin plasmonic flat lens*. Adv. Opt. Mater. **1**, 517–521 (2013).

3.29 D. Wen, F. Yue, S. Kumar, Y. Ma, M. Chen, X. Ren, P. E. Kremer, B. D. Gerardot, M. R. Taghizadeh, G. S. Buller, and X. Chen, *Metasurface for*

characterization of the polarization state of light, Opt. Express, **23**, 10272-10281 (2015).

3.30 W. T. Chen, K. Y. Yang, C. M. Wang, Y. W. Huang, G. Sun, I. D. Chiang, C. Y. Liao, W. L. Hsu, H. T. Lin, S. Sun, L. Zhou, A. Q. Liu, and D. P. Tsai, *High-efficiency broadband meta-hologram with polarization-controlled dual images*. Nano Lett. **14**, 225–230 (2014).

3.31 F. Aieta, P. Genevet, M. A. Kats, N. Yu, R. Blanchard, Z. Gaburro, and F. Capasso, *Aberration-free ultrathin flat lenses and axicons at telecom wavelengths based on plasmonic metasurfaces*. Nano Lett. **12**, 4932–4936 (2012).

3.32 M. Kang, T. Feng, H. T. Wang, and J. Li, *Wave front engineering from an array of thin aperture antennas*. Opt. Express **20**, 15882–15890 (2012)

3.33 F. Gori, *Measuring Stokes parameters by means of a polarization grating*. Opt. Lett. **24**, 584–586 (1999).

3.34 G. Biener, A. Niv, V. Kleiner, and E. Hasman, *Near-field Fourier transform polarimetry by use of a discrete space-variant subwavelength grating*. J. Opt. Soc. Am. A **20**, 1940–1948 (2003).

3.35 Z. Bomzon, G. Biener, V. Kleiner, and E. Hasman, *Space-variant Pancharatnam-Berry phase optical elements with computer-generated subwavelength gratings*. Opt. Lett. **27**, 1141–1143 (2002).

3.36 G. Li, et al., *Continuous control of the nonlinearity phase for harmonic generations*, Nat. Mater. **14**, 607-612 (2015).

3.37 G. Zheng, H. Mühlenbernd, M. Kenney, G. Li, T. Zentgraf, and S. Zhang, *Metasurface holograms reaching 80% efficiency*. Nat. Nanotechnol. **10**, 308-312 (2015).

Chapter 4 Polarization selective metasurface devices

Polarization selective optical elements (PSOEs) have the capacity to respond differently to the incident light based on its polarization state and realize different functions. Conventional PSOEs rely on well-defined nanostructures to realize anisotropy, but their mass applications are limited since high-precision machining proves to be difficult. In this chapter, we propose an approach to realize a novel metasurface PSOE, which merges two distinct functionalities by controlling the distribution of the nanoantennas. Moreover, the subwavelength pixel size and arbitrary phase levels can be achieved easily. The method proposed may further facilitate the development of multifunctional devices and the integration of micro-optical systems.

4.1 Introduction

People have always been looking for ways to integrate tools of different functions into a single device. Without exception, the field of optics keeps on developing multifunctional optical elements based on different mechanisms [4.1-4.4]. For example, PSOEs can achieve distinct functions according to the polarization state of the incident light, which makes them applicable for optical encryption [4.5], image processing [4.6] and so on. To make a PSOE, researchers conventionally use two anisotropic substrates [4.7-4.8] or a single form-birefringent structure [4.9-4.10] that respond differently to the two linearly and perpendicularly polarized light beams. However, traditional methods face the problems of limited phase levels and large pixel size due to the design principles and fabrication process.

Recently, the development of metasurfaces provides new opportunities to realize practical flat optical elements [4.11-4.26]. Benefiting from the polarization-sensitive properties and the flexibility in wavefront control, metasurfaces have the potential to work as PSOEs. Different from the conventional PSOEs that depend on anisotropic nanostructures, metasurface-based PSOEs can merge two different phase functions by controlling the distribution of the nanoantennas. Chen *et al.* proposed a metasurface hologram with polarization-controlled dual images, and each image is reconstructed either by horizontally or vertically polarized light [4.27]. Montelongo *et al.* demonstrated a polarization holography that can “switch on” or “switch off” the nanoantennas according to the polarization state of the incident light [4.28]. However, the limited phase levels [4.27] and binary amplitude modulation [4.28] remain as problems for further applications since multiple phase levels are always needed to control the wavefront precisely.

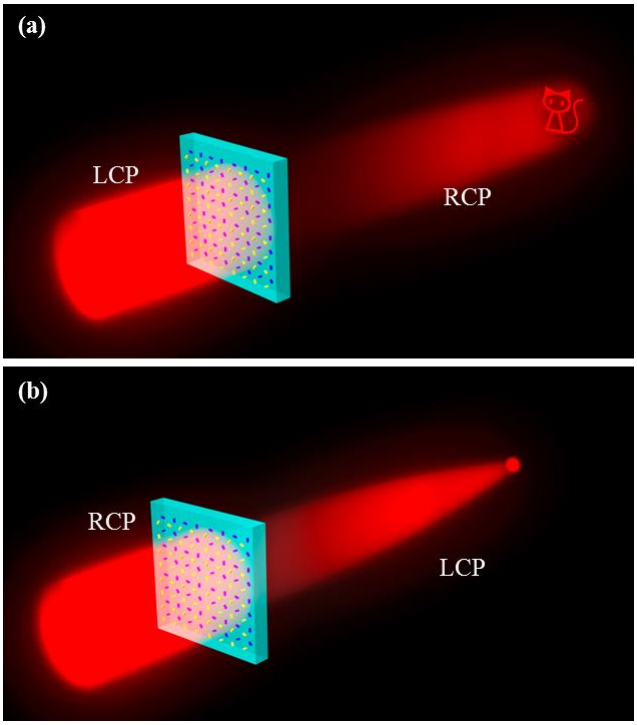

Figure 4.1 Schematics of the metasurface PSOE. (a) With the LCP incident light, a holographic 'cat' is observed. (b) A focal point replaces the holographic 'cat' for the RCP incident light, which shows that the metasurface device is polarization-switchable [4.14].

In this chapter, a PSOE is realized by using a transmission-type geometric metasurface, which can work as a hologram or a lens, depending on the polarization of the incident beam [figure 4.1]. Benefiting from the inherent properties of the geometric metasurface (chapter 2), arbitrary phase levels are achieved through more concise ways comparing with conventional PSOEs. Besides, the metasurface PSOE is ultra-thin and broadband, which can further facilitate its applications in integration optics and other relevant research fields.

4.2 Design methodology for the metasurface-based PSOE

4.2.1 Integration of two completely different phase functions

A phase-only hologram is first generated that reconstructs the image of 'cat' at a distance of 200 μm. As shown in figure 4.2(a), the target image is binary, and the value of each pixel is either 0 or 1. All the pixels in the target image are assumed to have random phase distributions, and each pixel emits a spherical wave. The spherical waves interfere in the hologram plane and form the field distribution

$$U(x,y) = \iint_{-\infty}^{\infty} U(x_0,y_0)\, h(x,y;\, x_0,y_0)\mathrm{d}x_0\mathrm{d}y_0 \tag{4.1}$$

with

$$h(x, y;\ x_0, y_0) = \frac{\exp\left[jk\sqrt{z^2+(x-x_0)^2+(y-y_0)^2}\right]}{j\lambda\sqrt{z^2+(x-x_0)^2+(y-y_0)^2}} \tag{4.2}$$

where $U(x_0, y_0)$ represents the complex amplitude of the target image.

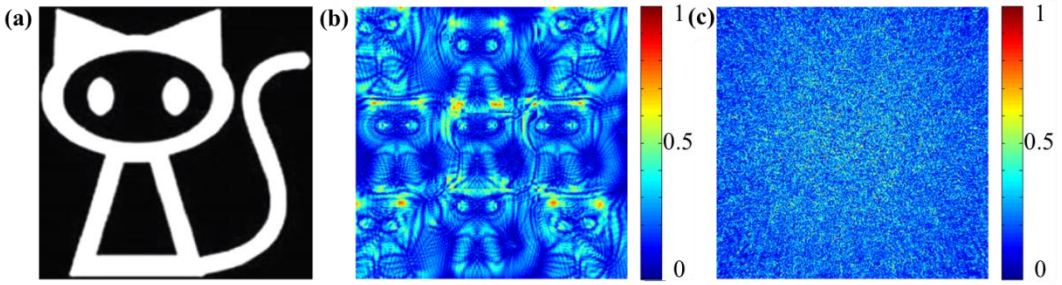

Figure 4.2 Design methodology for the metasurface-based PSOE. (a) The target image of 'cat' with a size of 150 μm×150 μm. $|U(x, y)|$ is calculated if the pixels in the target image are assumed to have (b) equal and (c) random phase distributions. It is shown that $|U(x, y)|$ is much more uniform in (c) than that in (b) [4.14].

Due to the random phase distributions of the target image, the energy is spread across a wide spectrum [figures 4.2(b)-(c)]. Therefore the argument of $U(x, y)$ is extracted to be the phase function of the phase-only hologram [4.29]

$$\varphi_1(x, y) = -\text{angle}\,[U(x, y)] \tag{4.3}$$

$\varphi_1(x, y)$ is sampled by a square lattice with the lattice distance *d*. The sampled $\varphi_1(x, y)$ is then encoded on a transmission-type metasurface. For the LCP incident light, a holographic image of 'cat' is reconstructed by the RCP scattered light as shown in figure 4.3(a). The hologram proposed here can be categorized into the computer generated holograms, which does not need a reference beam and no twin image is generated [4.29]. It is different from the traditional holograms, where the scattered light from the object interferes with the reference beam, and the intensity is recorded by the photosensitive material.

Similarly, a phase function of a concave lens can be written as [4.30]

$$\varphi_2(x, y) = \frac{2\pi}{\lambda}\left(\sqrt{x^2 + y^2 + f^2} - f\right) \tag{4.4}$$

where the focal length *f* equals to 200 μm. The phase function $\varphi_2(x, y)$ is also sampled and encoded onto the metasurface using the similar process. Under the illumination of LCP light, the outgoing RCP rays are diverged and form a background [figure 4.3(b)].

Finally, the metasurface hologram and lens are merged to form a new device. As shown in figure 4.3(c), the yellow nanorods correspond to the hologram, and they are named as type I for the description convenience. The purple nanorods correspond to the

lens, and they are named as type II. Although the merging process reduces the pixel size of the metasurface from d to $\sqrt{2}d/2$ (viewing from the 45° direction), it is still large enough to make each nanorod work independently.

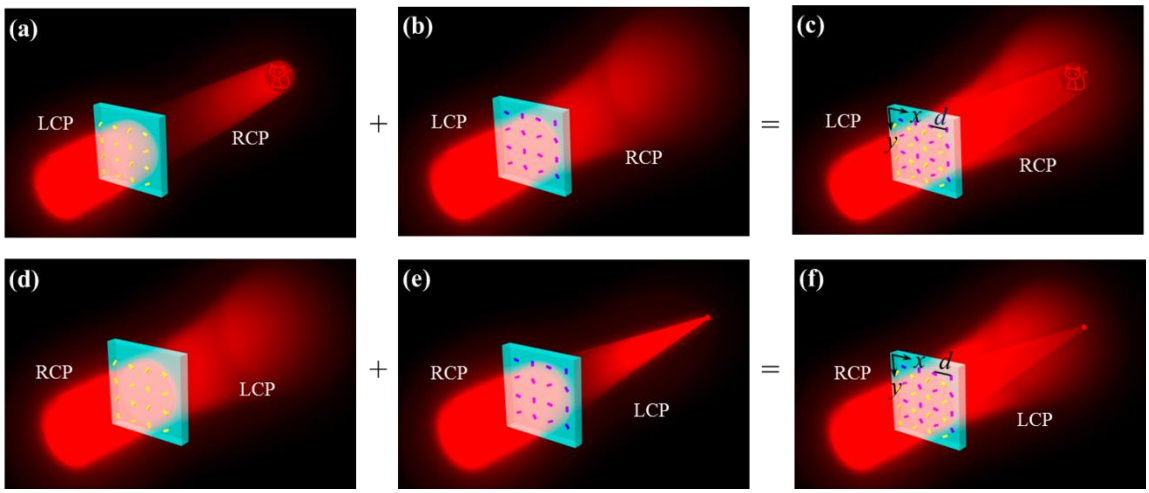

Figure 4.3 Design principle of the metasurface PSOE. (a) With the LCP incident light, the scattered RCP light forms a holographic 'cat' in the transmission side. (b) The metasurface concave lens diverges the scattered RCP light. (c) The hologram and the lens are merged to form a new device. The overall performance of the merged metasurface is a hologram. The distance d equals to 600nm. (d) For the RCP incident light, the metasurface in (a) diverges the scattered LCP light. (e) The metasurface in (b) turns into a convex lens and focus the scattered LCP light into a focal point. (f) The overall performance of the merged metasurface is a convex lens [4.14].

With the LCP incident light, the RCP scattered light from the merged metasurface can be divided into two parts: the light from nanorods I and that from nanorods II. The former converges to reconstruct the image of 'cat' while the latter diverges to form a subtle background [figure 4.3(c)]. Overall, the metasurface functions as a hologram for the LCP incident light. In contrast, under the illumination of RCP incident light, the phase of the LCP scattered light from the metasurface will be conjugated due to the inherent property of the geometric phase [4.31-4.38]. Hence the cases in figures 4.3(a), (b) and (c) change into that in (d), (e) and (f), respectively, and the merged metasurface works as a convex lens. Figures 4.3(c) and (f) clearly show the polarization-switchable property of the metasurface device.

4.2.2 Simulation of the background noise introduced by the merging method

As mentioned above, the scattered light from nanorods I contributes to the signal while that from nanorods II serves as the background noise, and vice versa. To evaluate the effect of the background noise, a comparison is made between the holographic images reconstructed by the metasurfaces before and after merging [figures 4.4-4.5]. In comparison with figure 4.4(b), figure 4.4(d) shows that the background noise is

increased after the merging process. But the outline of 'cat' is still much brighter than the background noise; hence the 'cat' pattern is still very clear [figure 4.4(c)]. Figure 4.5 shows that the background noise can be ignored when the metasurface device works as a convex lens.

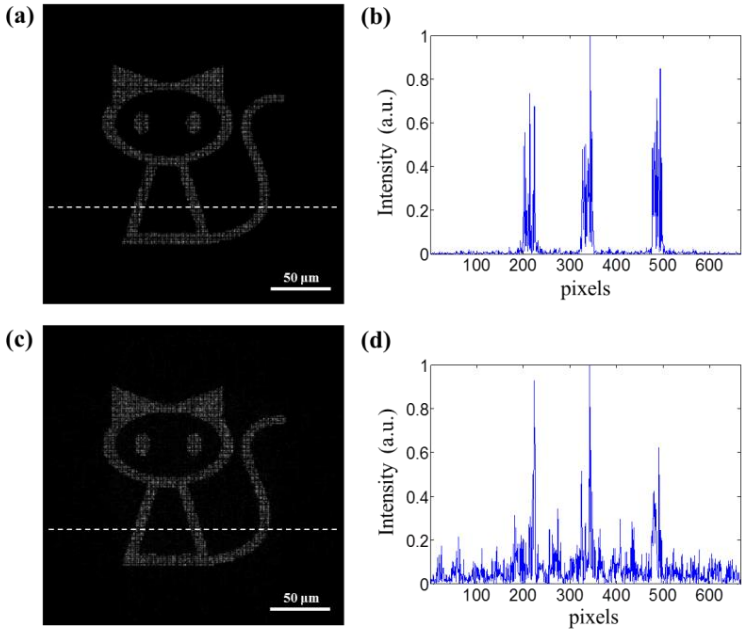

Figure 4.4 Comparison of the holographic images of 'cat' before and after the merging process. The simulated holographic images of 'cat' are obtained from (a) the single metasurface hologram and (c) the merged metasurface. The normalized intensity profiles along the dashed lines in (a) and (c) are shown in (b) and (d), respectively [4.14].

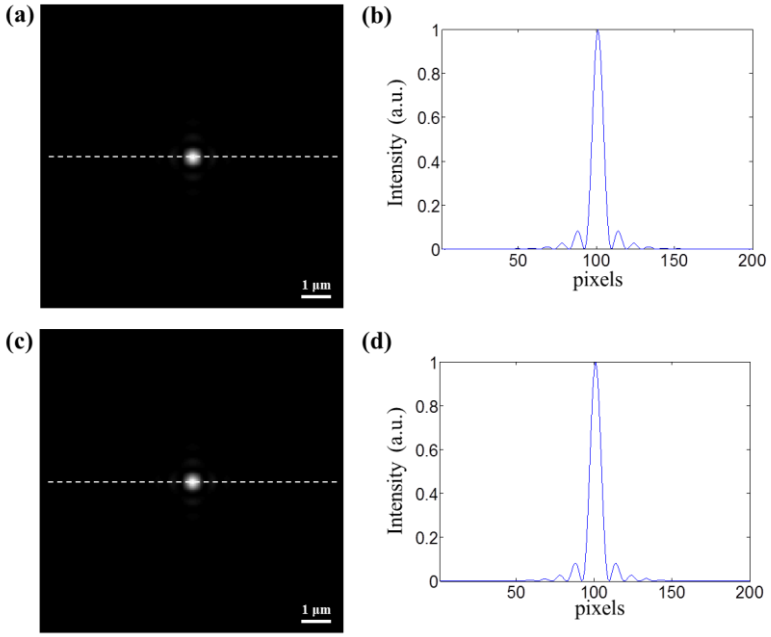

Figure 4.5 Comparison of the focal points. The simulated focal points are obtained from (a) the single metasurface lens and (c) the merged metasurface. The normalized intensity profiles along the dashed lines in (a) and (c) are shown in (b) and (d), respectively [4.14].

4.3 Experimental characterizations of the multifunctional metasurface device

4.3.1 Polarization selective properties of the metasurface

The phase function of the merged metasurface is first generated and encoded onto a nanorod array [figure 4.6(a)]. Then the nanorod array is transferred onto a glass substrate by using the similar fabrication process as mentioned in section 3.2 [figure 4.6(b)]. The fabricated sample covers an area of 400 μm×400 μm.

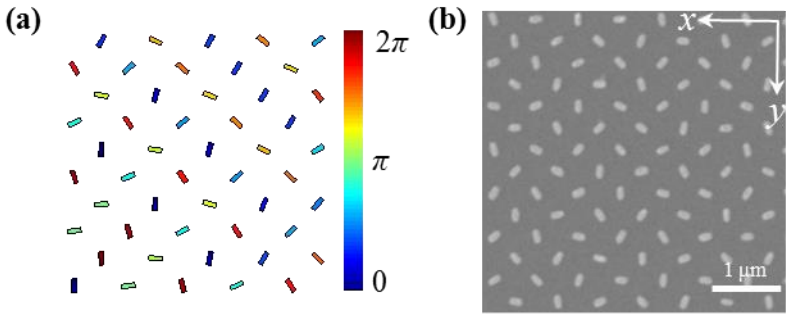

Figure 4.6 (a) Schematic to show the merged metasurface. The color of a nanorod represents the corresponding geometric phase value of the scattered light. (b) SEM image of the sample. The nanorods have the same length (150 nm), width (50 nm) and thickness (40 nm).

The experimental device is shown in figure 4.7. The light source is a supercontinuum laser (NKT, SuperK Extreme), and the incident beam is first slightly focused by a lens. A polarizer and a quarter-wave plate are used to change the incident light into LCP or RCP, which then impinges normally onto the metasurface. The scattered light is collected by an objective lens (10X/0.3) that is fastened to a three dimensional translational stage. Another quarter-wave plate and a polarizer are placed after the objective to make sure that only the orthogonally polarized scattered light is collected by the CCD. The lens in front of CCD, along with the objective forms a microscope to amplify the holographic image and the focal point.

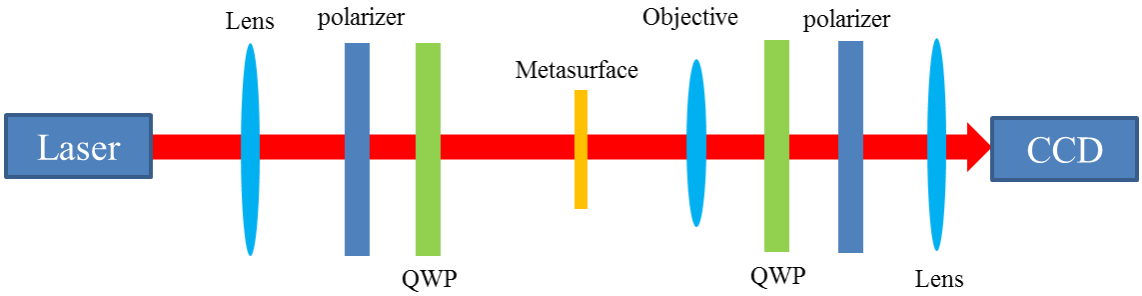

Figure 4.7 Experimental setup of to characterize the polarization selectivity of the metasurface.

With the LCP incident light, the position of the objective is gradually adjusted to get a clear image of ‘cat’ that is formed by the RCP scattered light [figure 4.8(a)]. Then we change the incident light to be RCP and only observe the LCP scattered light, a focal

point is formed at the same position that the holographic image of 'cat' is observed. The experimental results verify the polarization selective properties of the metasurface, agreeing with the prediction.

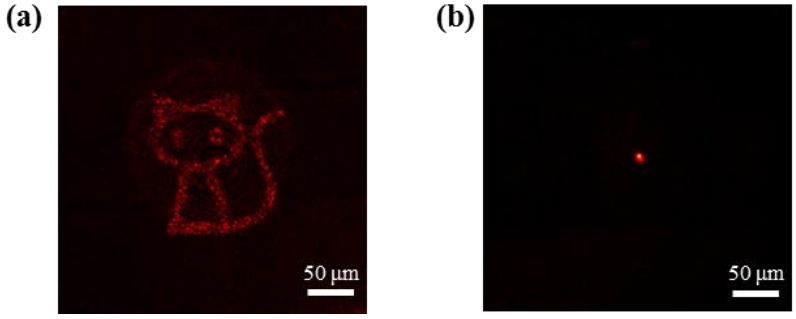

Figure 4.8 Experimental results at the wavelength of 633 nm. (a) With the LCP incident light, a holographic 'cat' is captured by the CCD. (b) The metasurface convex lens focuses the LCP scattered light to a point with the RCP incident light [4.14].

The signal-to-noise ratio (SNR) is an important factor for the image quality of a hologram. As shown in figure 4.9, the SNR is defined as I_B/S_A, where I_B represents the mean amplitude of area B, which is a part of the holographic image. S_A is the standard deviation of the amplitude in area A that is a part of the background. The value of SNR is 10.51 in the simulated image [figure 4.9(a)] and 7.97 in the experimentally obtained image [figure 4.9(b)]. The enlarged parts in figure 4.9 also verify that the background noise (intensity in areas A and C) is higher in the experiment than that in the simulation, and the mismatch can be ascribed to the fabrication errors and the observation system misalignment [4.39].

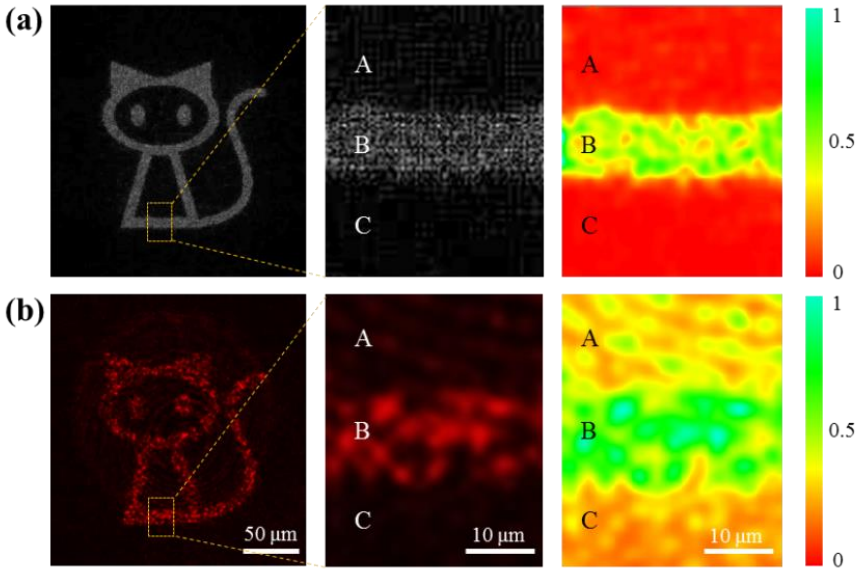

Figure 4.9 Comparison of the reconstructed images from (a) the simulation and (b) the experiment. Area B represents a part of the holographic image. The background is represented by the two areas A and C that are located beside area B [4.14].

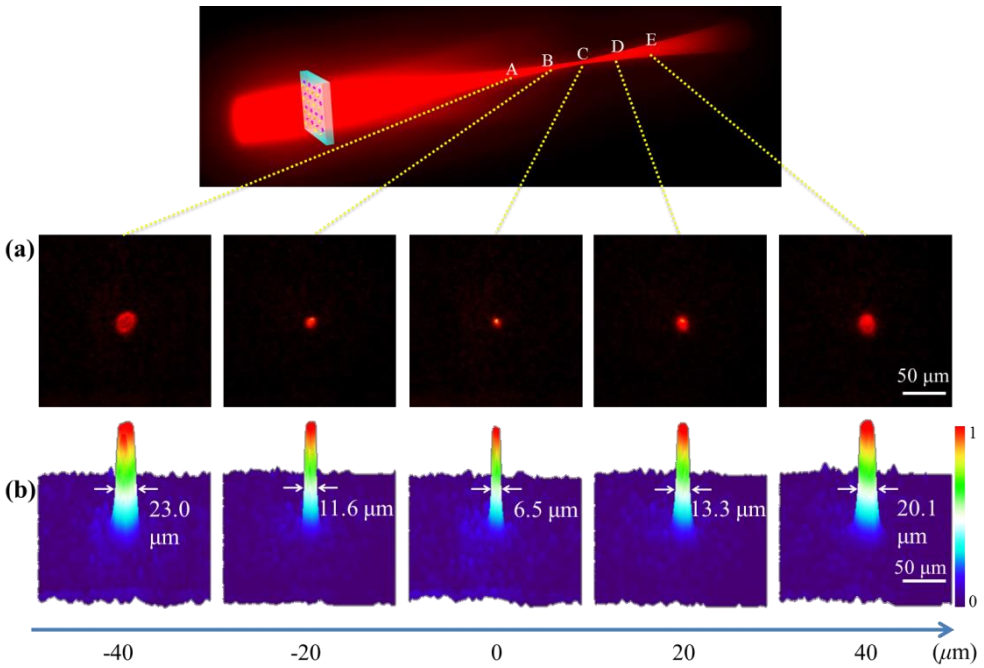

Figure 4.10 Focusing properties of the metasurface when it works as a convex lens. (a) Experimentally obtained CCD images of the light spots at different points A-E along the optical path. The distance between the two neighboring points is 20 μm. The focal point is located at C. (b) The corresponding normalized intensity distribution in (a) [4.14].

The focusing properties of the metasurface when it works as a convex lens are studied. Five different points along the optical path are chosen, and their CCD images are captured as shown in figure 4.10. Here the beam size of a light spot is defined as the full width at its half maximum, and it shows that the beam size is almost symmetric about the focal point. In comparison with the size of the metasurface (400 μm×400 μm), the beam size is about 6.5 μm at the focal point, representing an effective focus of the scattered light.

4.3.2 Broadband performance of the metasurface PSOE

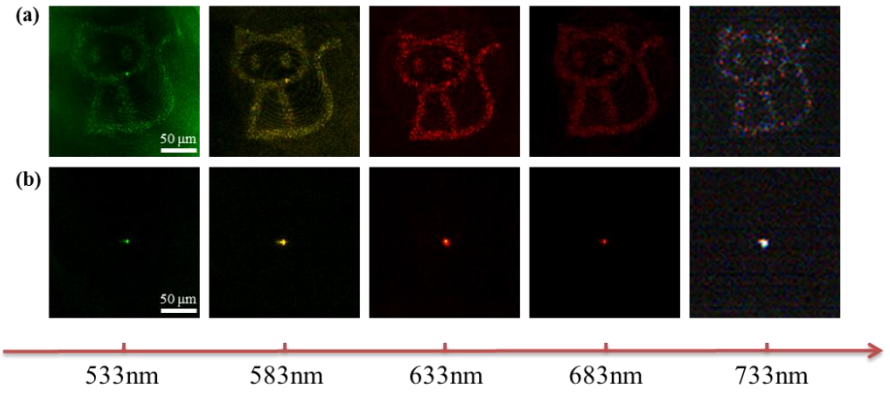

Figure 4.11 Experimental demonstration of the broadband performance of the metasurface. (a) Images of the holographic 'cat' with the LCP incident beam. (b) Images of the focal points with the RCP incident beam [4.14].

Since the geometric phase is independent of wavelengths, the metasurface PSOE can work for a broad wavelength range. The images of 'cat' and the focal point are captured between 533 nm and 733 nm with the step of 50 nm, as shown in figure 4.11.

4.3.3 Metasurface PSOE that integrates two holograms

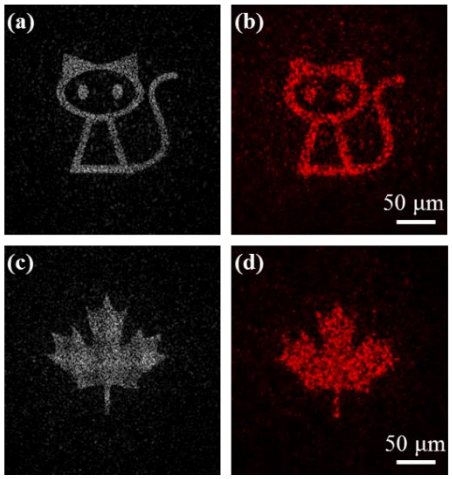

Figure 4.12 (a) and (c) represent the simulated holographic images for the LCP and RCP incident light, respectively. (b) and (d) are the experimental results that correspond to (a) and (c) at 633 nm, respectively.

By using the design principle proposed in section 4.2, two holograms can also be merged to form a PSOE. As shown in figure 4.12, the reconstructed holographic image is either 'cat' or 'leaf', which is dependent on the polarization of the incident light.

4.4 The multifunctional metasurface lens for imaging and Fourier transform

4.4.1 Design of the multifunctional metasurface lens

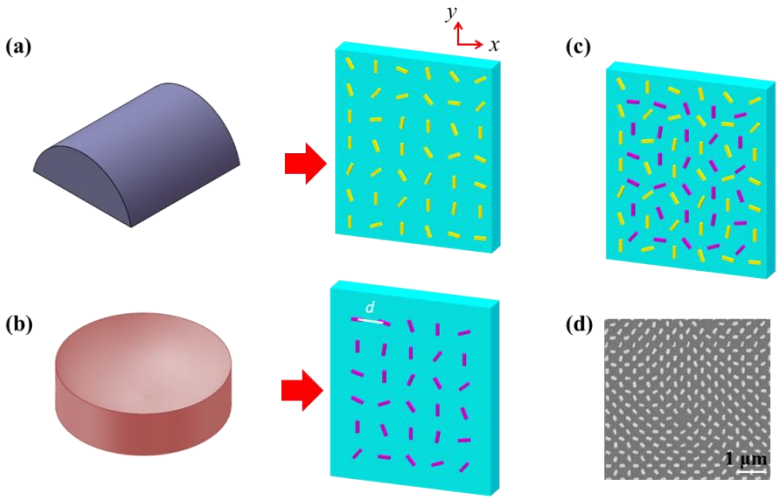

Figure 4.13 Design of the multifunctional lens. The functionalities of (a) a conventional cylindrical lens and (b) a spherical lens can be realized by metasurfaces consisting of nanorods. *d* is the pixel pitch, and it equals to 500 nm. The nanorods have the same length (200 nm), width (80 nm) and thickness (40 nm). (c) The two metasurface lenses are merged to form a multifunctional lens, with the size of 333 μm×333 μm. (d) SEM image of the multifunctional lens [4.15].

Conventional lenses cannot distinguish the incident light with different polarization states, and their functionalities are determined by the surface topography [figure 4.13]. In this section, we propose a multifunctional lens with flat surface, and it responds differently to the incident LCP and RCP light. The multifunctional lens functions as the combination of a spherical lens and a cylindrical lens with different polarities. Imaging and 1D/2D Fourier transform properties of the multifunctional lens are experimentally demonstrated in this section.

To create the multifunctional lens, we first generate the phase functions of the positive cylindrical lens and the negative spherical lens, which are represented by φ_1 and φ_2, respectively.

$$\varphi_1(y) = -\frac{2\pi}{\lambda}\left(\sqrt{y^2 + f^2} - f\right) \tag{4.5}$$

$$\varphi_2(x, y) = \frac{2\pi}{\lambda}\left(\sqrt{x^2 + y^2 + f^2} - f\right) \tag{4.6}$$

The focal length f is designed to be 198 μm for the 640 nm incident light. Then the two phase functions φ_1 and φ_2 are sampled and encoded onto the nanorod arrays as shown in figures 4.13(a) and (b), respectively. Finally, the two nanorod arrays are merged to form the multifunctional lens [figure 4.13(c)]. For the convenience of description, the nanorods in the merged metasurface corresponding to the positive cylindrical lens and the negative spherical lens are named as type I and type II, respectively.

For the RCP incident light shining on the multifunctional lens, the LCP scattered light from nanorods I is converged into a real focal line at $z=f$. Meanwhile, the LCP light from nanorods II diverges in the transmission side, as if it is emitted from a virtual focal point at $z=-f$. Due to the intrinsic properties of the geometric phase, the polarities of the cylindrical lens and spherical lens both reverse if the incident light is changed to LCP. Therefore, a real focal point and a virtual focal line can be observed at $z=f$ and $z=-f$, respectively.

4.4.2 Focusing properties of the multifunctional lens

To characterize the focusing properties of the multifunctional lens, the experimental setup is the same as that in figure 4.7. With the RCP incident light, the image of a real focal line is captured at $z=f$ [figure 4.14(a)]. If the objective is gradually moved along the optical path to shorten its distance from the metasurface, a virtual focal point at $z=-f$ can be observed [figure 4.14(b)]. The focal point and focal line swap their positions if the incident light is changed into LCP [figures 4.14(c) and (d)].

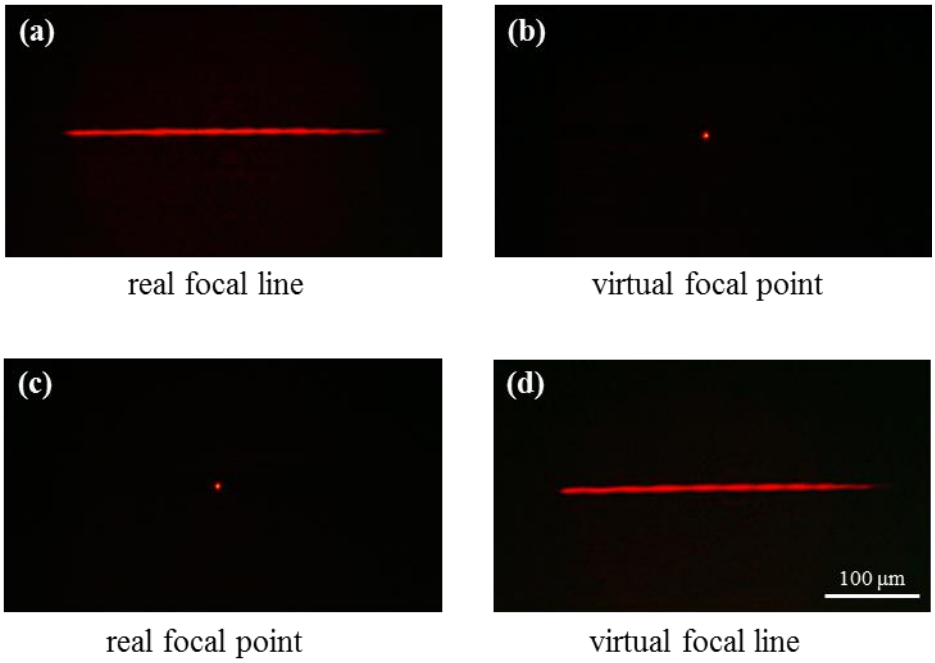

Figure 4.14 Focusing properties of the multifunctional lens. (a-b) With the RCP incident light at 640 nm, a real focal line and a virtual focal point can be observed at $z=f$ and $z=-f$, respectively. (c-d) If the incident light changes into LCP, a real focal point and a virtual focal line are observed at $z=f$ and $z=-f$, respectively [4.15].

4.4.3 Imaging properties of the multifunctional lens

Imaging is one of the primary functionalities of a lens. Here the polarization selective imaging of the multifunctional lens is experimentally verified. The object to be imaged is a T-aperture array [figure 4.15(a)], which is generated by using the focused ion beam to cut through a layer of chromium film with 40 nm thickness [figure 4.15(b)]. Since chromium is a high lossy material in the visible range, the incident light can only pass through the apertures themselves.

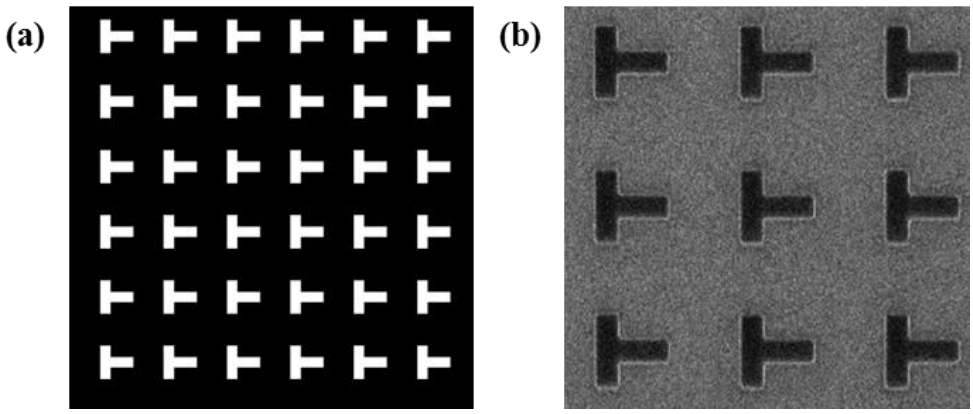

Figure 4.15 Schematic of the T-aperture array and the SEM image. (a) Schematic of the T-aperture array. The size of each aperture is 50 μm by 50 μm. The pixel pitch is 100 μm. (b) SEM image of the fabricated T-aperture array.

The experimental setup is shown in figure 4.16, which is similar to that in figure 4.7, but the T- array is added to the optical path and fixed in front of the metasurface lens with a distance *s*. The incident light passes through the T-array, transformed by the metasurface lens, and captured by a CCD camera.

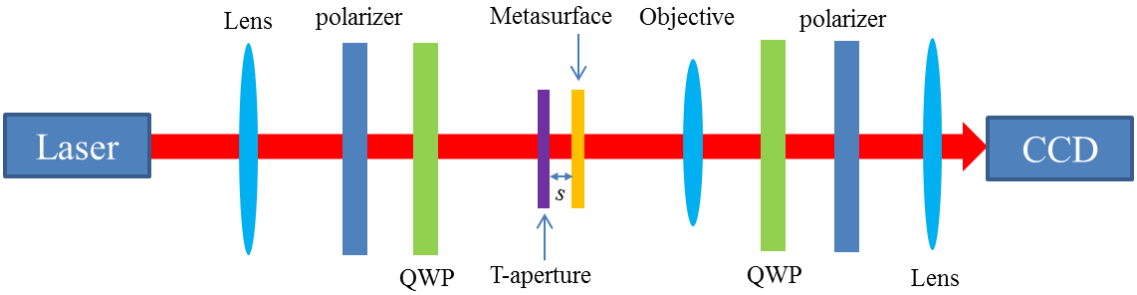

Figure 4.16 Experimental setup to study the imaging properties of the multifunctional lens.

In the experiment, the value of *s* is first set to be 105 μm, which is smaller than the focal distance of the lens (*f*=198 μm when the incident light is 640 nm). From geometric optics, we know that only virtual images can be formed by a lens if the object distance is within the focal length (figure 4.17).

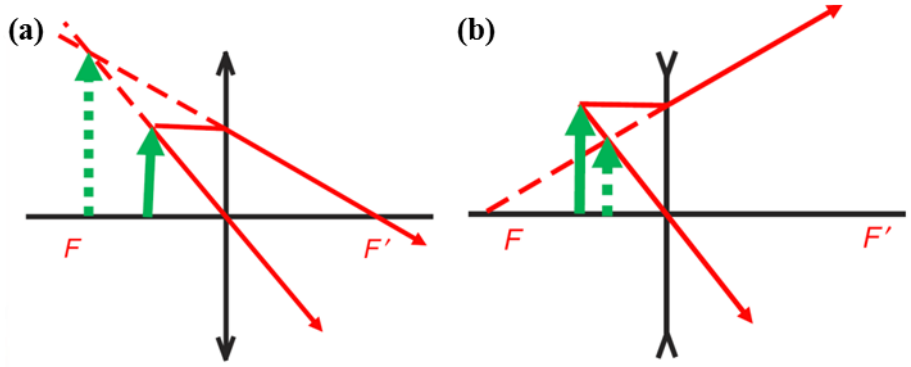

Figure 4.17 Schematics of the virtual images if the object distance is within the focal length. (a) The object (real arrow) is transformed by a convex lens, and a magnified virtual image (dashed arrow) is formed. (b) The object is transformed by a concave lens, forming a shrunken image [4.12].

Under the illumination of RCP light, the virtual image generated by the positive cylindrical lens is first captured as shown in figure 4.18(a), which is magnified along the *y*- direction. By moving the objective along the optical path to the CCD direction, a T-image shrunken both in *x*- and *y*- directions can be observed due to the transformation of the negative spherical lens [figure 4.18(b)]. The virtual images are also simulated using the diffraction theory [figures 4.18(c-d)], which agree well with the experimental results both in the image shapes and magnifications.

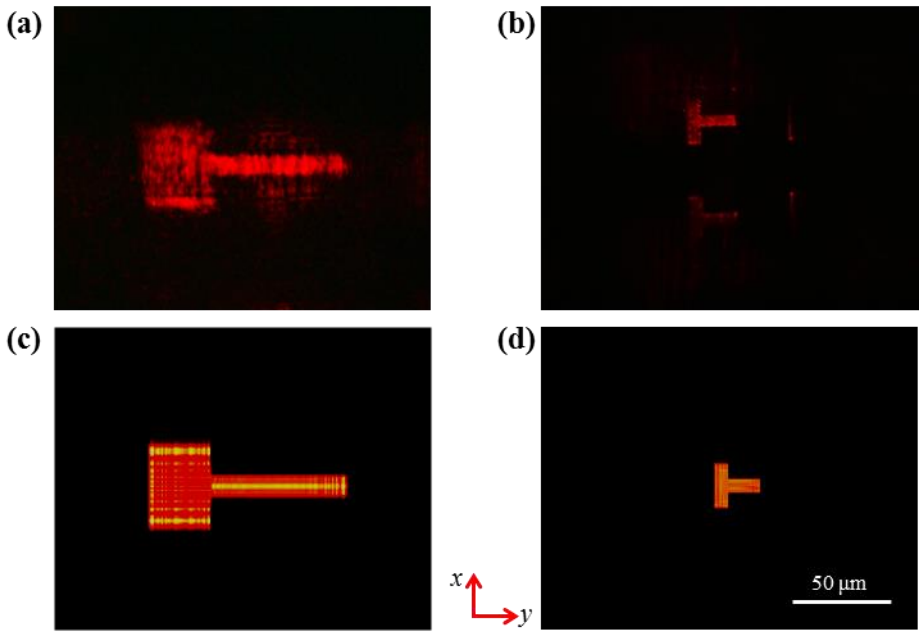

Figure 4.18 Different virtual images formed by the multifunctional lens with the RCP incident light. (a) The virtual image is stretched along the *y*-direction due to the transformation of the positive cylindrical lens. (b) The virtual image is shrunken in both directions due to the transformation of the negative spherical lens. (c-d) Simulated images corresponding to figures (a) and (b) [4.15].

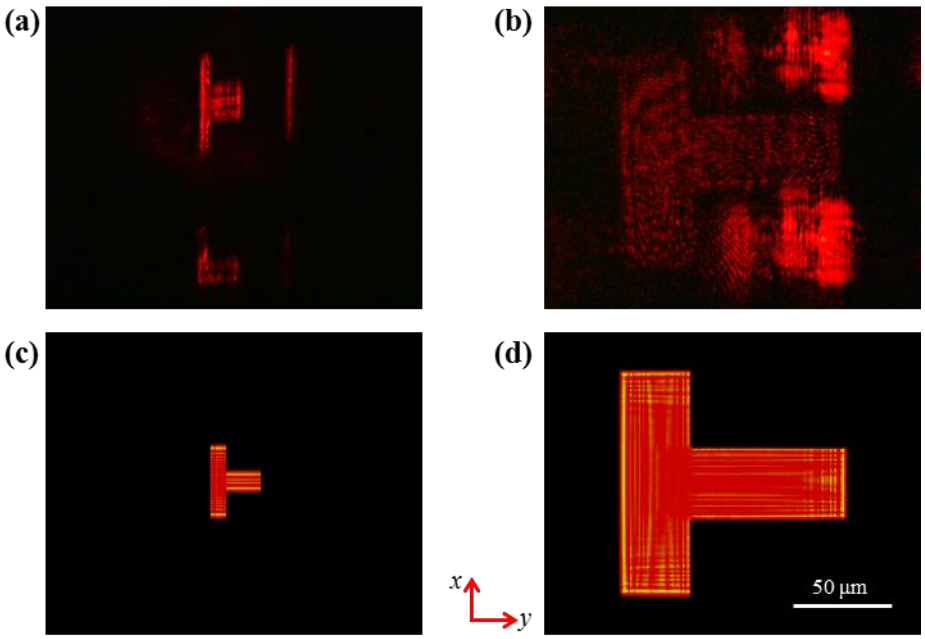

Figure 4.19 Different virtual images formed by the multifunctional lens for the LCP incident light. (a) The virtual image is shrunken along the *y*-direction due to the transformation of the negative cylindrical lens. (b) The virtual image is magnified in both directions by the positive spherical lens. (c-d) Simulated images corresponding to figures (a) and (b) [4.15].

When the incident light changes into LCP, the polarities of the cylindrical lens and the spherical lens both reverse. Then a virtual image shrunken along the *y*-direction [figure 4.19(a)] and another image magnified along both directions [figure 4.19(b)] are

obtained. Comparing figures 4.18(a) with 4.19(a), the virtual images formed by the cylindrical lens are either magnified or shrunken in the *y*-direction that is dependent on the polarization of the incident light. It is the same for the virtual images formed by the spherical lens, which are either shrunken or magnified along both directions.

If the object distance *s* is increased from 105 μm to 330 μm, it falls into the range between *f* and 2*f*. Then the positive spherical lens in the metasurface can form an inverted and magnified real image [figure 4.20(b)] in comparison with the original image of the T-shaped aperture [figure 4.20(a)]. Besides the large T-aperture array, a smaller T-aperture array (11μm×6μm for each aperture) is also used as an object [figure 4.20(c)], and its magnified real image is shown in figure 4.20(d).

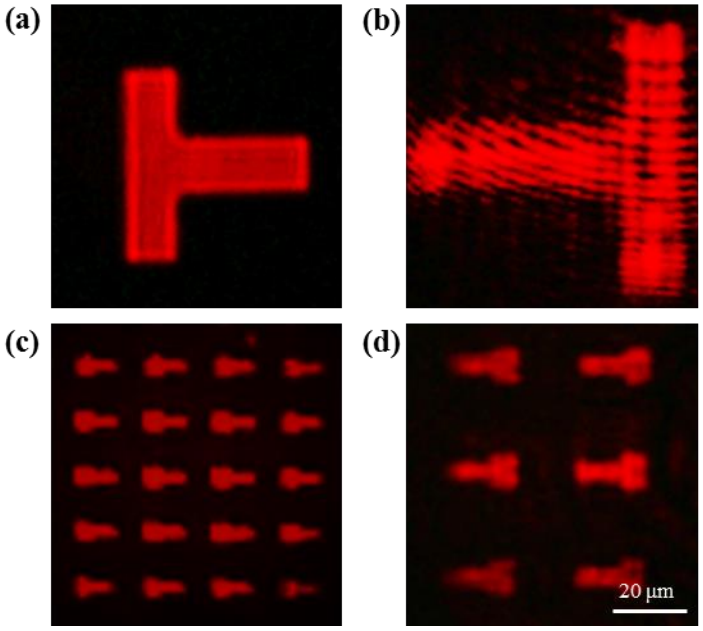

Figure 4.20 Real images formed by the multifunctional lens with the LCP incident light. (a) Original image of a large T-aperture (50 μm×50 μm) under the illumination of 640 nm laser beam. (b) The light passing through the T-aperture is transformed by the positive spherical lens and forms a real image, which is inverted and magnified. (c) Original image of a smaller T-aperture array and each aperture has the size of 11 μm×6 μm. (d) The real image of the smaller T-aperture array [4.15].

4.4.4 Fourier transform by the multifunctional lens

Since a cylindrical lens and a spherical lens can give certain phase functions [equations (4.5) and (4.6)] to the incident light, the 1D and 2D Fourier transforms can be performed accordingly. The T-aperture array (figure 4.15) is adopted again as the object to be Fourier transformed. The experimental setup is the same as that in figure 4.16, and *s* is set to be 105 μm.

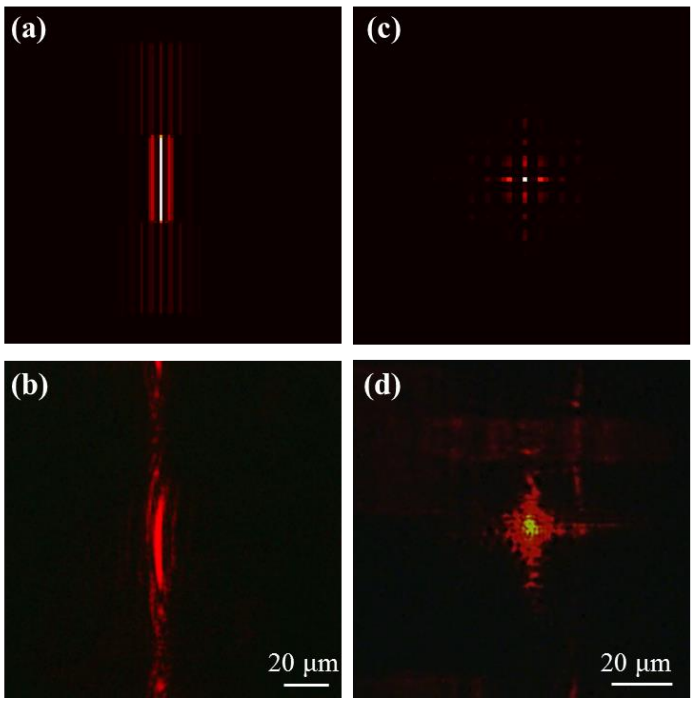

Figure 4.21 1D and 2D Fourier transforms performed by the multifunctional lens with the RCP incident light. The simulated (a) 1D and (c) 2D Fourier transforms of the T-aperture array are obtained using fast Fourier transform. (b) 1D and (d) 2D Fourier transforms by the multifunctional lens are obtained at 640 nm. The images (b) and (d) are captured at the real and virtual focal planes, respectively [4.15].

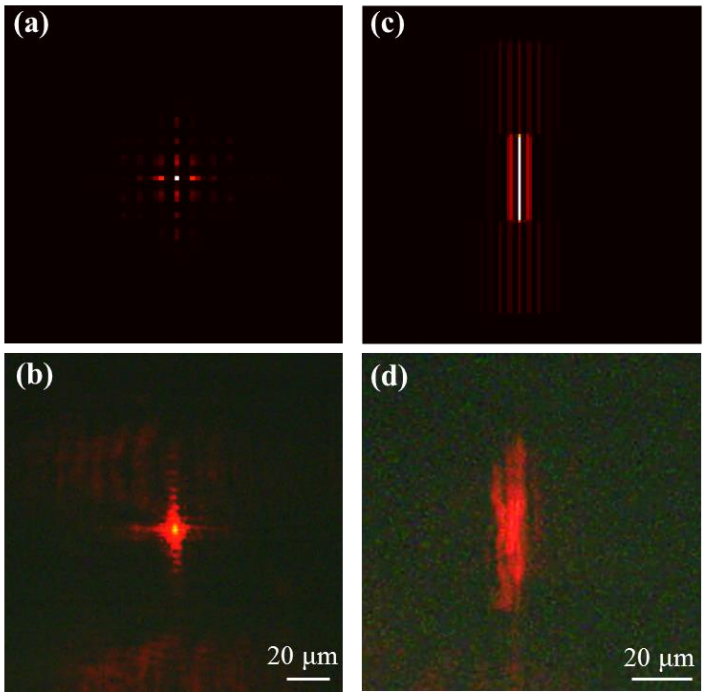

Figure 4.22 1D and 2D Fourier transforms performed by the multifunctional lens with the LCP incident light. The simulated (a) 2D and (c) 1D Fourier transforms of the T-aperture array are obtained. (b) 2D and (d) 1D Fourier transforms by the multifunctional lens are obtained at 640 nm. The images (b) and (d) are captured at the real and virtual focal planes, respectively [4.15].

Under the illumination of RCP incident light, the intensity distribution at the real focal plane is proportional to the 1D Fourier transform of the object, which is performed along the horizontal direction by the positive cylindrical lens [figures 4.21(a)-(b)]. The intensity distribution at the virtual focal plane represents the 2D Fourier transform of the object, and it is performed along both the horizontal and vertical directions by the negative spherical lens [figures 4.21(c)-(d)]. When the incident light changes to LCP, the positions of 1D and 2D Fourier transforms are swapped as shown in figure 4.22. Both the 1D and 2D Fourier transforms are useful in the Fourier spectrum analysis systems, which can be applied to analyze the structure of the target object.

4.5 Conclusion

In conclusion, an approach to integrate two completely different functionalities into a single metasurface device is experimentally verified. The overall performance of the metasurface device is dependent on the helicity of the incident circularly polarized light. Benefiting from the geometric metasurface, multiple phase levels, and broadband performance are achieved through more concise ways comparing with conventional PSOEs. The approach proposed in this chapter may pave the way for further reducing the volume of the optical elements and increasing the density of functionalities.

4.6 References

4.1 L. Chen, D. Zhao, *Optical color image encryption by wavelength multiplexing and lensless Fresnel transform holograms*. Opt. Express **14**, 8552-8560 (2006).

4.2 P. J. Winzer, *Making spatial multiplexing a reality*. Nat. Photonics **8**, 345-348 (2014).

4.3 Y. Tu, G. Zhang, Z. Zhai, J. Xu, *Angular multiplexing storage of light pulses and addressable optical buffer memory in Pr3+:Y2SiO5 based on electromagnetically induced transparency*. Phys. Rev. A **80**, 033816 (2009).

4.4 T. Zentgraf, J. Valentine, N. Tapia, J. Li, X. Zhang, *An Optical "Janus" Device for Integrated Photonics*. Adv. Mater. **22**, 2561-2564 (2010).

4.5 N. Zhu, Y. Wang, J. Liu, J. Xie, H. Zhang, *Optical image encryption based on interference of polarized light*. Opt. Express **17**, 13418-13424 (2009).

4.6 F. Xu, J. E. Ford, Y. Fainman, *Polarization-selective computer-generated holograms: design, fabrication, and applications*. App. Opt. **34**, 256-266 (1995).

4.7 J. E. Ford, F. Xu, K. Urquhart, Y. Fainman, *Polarization-Selective Computer-Generated Holograms*. Opt. Lett. **18**, 456-458 (1993).

4.8 N. Nieuborg, A. Kirk, B. Morlion, H. Thienpont, I. Veretennicoff, *Polarization-selective diffractive optical elements with an index-matching gap material*. App. Opt. **36**, 4681-4685 (1997).

4.9 F. Xu, C. C. Cheng, A. Scherer, R. C. Tyan, P. C. Sun, Y. Fainman, *Form-birefringent computer-generated holograms*. Opt. Lett. **21**, 1513-1515 (1996).

4.10 W. Yu, T. Konishi, T. Hamamoto, H. Toyota, T. Yotsuya, Y. Ichioka, *Polarization-multiplexed diffractive optical elements fabricated by subwavelength structures*. App. Opt. **41**, 96-100 (2002).

4.11 N. F. Yu, et al. *Light Propagation with Phase Discontinuities: Generalized Laws of Reflection and Refraction*. Science **334**, 333-337 (2011).

4.12 X. Z. Chen, et al. *Dual-polarity plasmonic metalens for visible light*. Nat. Commun. **3**, 1198 (2012).

4.13 X. J. Ni, N. K. Emani, A. V. Kildishev, A. Boltasseva, V. M. Shalaev, *Broadband Light Bending with Plasmonic Nanoantennas*. Science **335**, 427-427 (2012).

4.14 D. Wen, et al., *Metasurface Device with Helicity-Dependent Functionality*, Adv. Opt. Mater. **4**, 321-327 (2016).

4.15 D. Wen, F. Yue, M. Ardron, and X. Chen, *Multifunctional metasurface lens for imaging and Fourier transform*, Sci. Rep. **6**, 27628 (2016).

4.16 S. C. Jiang, et al. *Controlling the Polarization State of Light with a Dispersion-Free Metastructure*. Phys. Rev. X **4**, 021026 (2014).

4.17 A. V. Kildishev, A. Boltasseva, V. M. Shalaev, *Planar Photonics with Metasurfaces*. Science **339**, 1232009 (2013).

4.18 Y. B. Li, X. Wan, B. G. Cai, Q. Cheng, T. J. Cui, *Frequency-Controls of Electromagnetic Multi-Beam Scanning by Metasurfaces*. Sci. Rep. **4**, 06921 (2014).

4.19 D. Lin, P. Fan, E. Hasman, M. L. Brongersma, *Dielectric gradient metasurface optical elements*. Science **345**, 298-302 (2014).

4.20 J. Scheuer, Y. Yifat, *Holography: Metasurfaces make it practical*. Nat. Nano. **10**, 296-298 (2015).

4.21 Y. Zhao, M. A. Belkin, A. Alu, *Twisted optical metamaterials for planarized ultrathin broadband circular polarizers*. Nat. Commun. **3**, 870 (2012).

4.22 N. K. Grady, et al. *Terahertz Metamaterials for Linear Polarization Conversion and Anomalous Refraction*. Science **340**, 1304-1307 (2013).

4.23 S. Larouche, Y. J. Tsai, T. Tyler, N. M. Jokerst, D. R. Smith, *Infrared metamaterial phase holograms*. Nat. Mater. **11**, 450-454 (2012).

4.24 Y. Yifat, M. Eitan, Z. Iluz, Y. Hanein, A. Boag, J. Scheuer, *Highly Efficient and Broadband Wide-Angle Holography Using Patch-Dipole Nanoantenna Reflectarrays*. Nano Lett. **14**, 2485-2490 (2014).

4.25 X. Li, S. Xiao, B. Cai, Q. He, T. J. Cui, L. Zhou, *Flat metasurfaces to focus electromagnetic waves in reflection geometry*. Opt. Lett. **37**, 4940-4942 (2012).

4.26 A. Pors, M. G. Nielsen, R. L. Eriksen, S. I. Bozhevolnyi, *Broadband Focusing Flat Mirrors Based on Plasmonic Gradient Metasurfaces*. Nano Lett. **13**, 829-834 (2013).

4.27 W. T. Chen, et al. *High-Efficiency Broadband Meta-Hologram with Polarization-Controlled Dual Images*. Nano Lett. **14**, 225-230 (2014).

4.28 Y. Montelongo, J. O. Tenorio-Pearl, W. I. Milne, T. D. Wilkinson, *Polarization Switchable Diffraction Based on Subwavelength Plasmonic Nanoantennas*. Nano Lett. **14**, 294-298 (2014).

4.29 L. L. Huang, et al. *Three-dimensional optical holography using a plasmonic metasurface.* Nat. Commun. **4**, 2808 (2013).

4.30 F. Aieta, et al. *Aberration-Free Ultrathin Flat Lenses and Axicons at Telecom Wavelengths Based on Plasmonic Metasurfaces*. Nano Lett. **12**, 4932-4936 (2012).

4.31 N. Yu, F. Capasso, *Flat optics with designer metasurfaces*. Nat. Mater. **13**, 139-150 (2014).

4.32 M. V. Berry, *QUANTAL PHASE-FACTORS ACCOMPANYING ADIABATIC CHANGES*. Proc. R. Soc. A **392**, 45-57 (1984).

4.33 M. Kang, T. H. Feng, H. T. Wang, J. S. Li, *Wave front engineering from an array of thin aperture antennas*. Opt. Express **20**, 15882-15890 (2012).

4.34 D. Wen, et al. *Metasurface for characterization of the polarization state of light*. Opt. Express **23**, 10272-10281 (2015).

4.35 F. Gori, *Measuring Stokes parameters by means of a polarization grating*. Opt. Lett. **24**, 584-586 (1999).

4.36 Y. Yirmiyahu, A. Niv, G. Biener, V. Kleiner, E. Hasman, *Vectorial vortex mode transformation for a hollow waveguide using Pancharatnam-Berry phase optical elements*. Opt. Lett. **31**, 3252-3254 (2006).

4.37 L. L. Huang, et al. *Dispersionless Phase Discontinuities for Controlling Light Propagation*. Nano Lett. **12**, 5750-5755 (2012).

4.38 G. Zheng, H. Mühlenbernd, M. Kenney, G. Li, T. Zentgraf, S. Zhang, *Metasurface holograms reaching 80% efficiency*. Nat. Nano. **10**, 308-312 (2015).

4.39 P. Hariharan, *Optical Holography Principles, techniques,and applications*, 2nd edition. Cambridge University Press: New York, 1996.

Chapter 5 Helicity multiplexed broadband metasurface holograms

In this chapter, a helicity multiplexed metasurface hologram (HMMH) is presented, which reconstructs two holographic images simultaneously. The two images can swap their positions with the helicity reversion of the incident light. Due to the off-axis design principle, the background noise is greatly suppressed. Besides, the reflection-type metasurface provides high conversion efficiency over a wide operating wavelength range. The design principle of the HMMH and its high performance provide new opportunities for the functionality-switchable optical devices.

5.1 Introduction

Computer-generated holograms (CGHs) fabricated as phase-only optical elements are usually polarization-independent. However, a polarization selective CGH (PSCGH) can reconstruct distinct holographic images according to the polarization state of the incident light, and therefore extends the CGH applications, such as image processing [5.1] and multilevel optical switching [5.2]. To create a PSCGH by the conventional method, two phase-only CGHs are usually encoded onto one birefringent substrate [5.3], or an isotropic substrate with the form-birefringence [5.4]. There is a positive correlation between the conversion efficiency of a PSCGH and its phase levels within 0 and 2π. Multiple phase levels are generally realized through pixels of different depths for the birefringent substrate, or gratings with variable filling factors for the isotropic substrate. However, the risks of etching, resolution and alignment errors increase significantly with the number of phase levels for both kinds, especially when the extreme anisotropy is required. Besides, traditional PSCGHs usually have pixels much larger than the operating wavelength, which hinders fine sampling of the hologram. Above all, most current PSCGHs are narrowband since their nanostructures are designed to work for a given wavelength.

With the development of nanofabrication technology, metamaterials provide great flexibility in tailoring electromagnetic properties. As an emerging field of metamaterials, metasurfaces have attracted much attention [5.5-5.15], and they are opening up new opportunities to realize CGHs as well as PSCGHs [5.16-5.17]. Recently, a PSCGH with four phase levels has been realized by using a high-efficiency broadband metasurface consisting of the gold cross nanorods [5.16]. Although the nanorods with different lengths provide designed phase retardance to the scattered light, it is practically not able to generate a continuous phase profile due to the unwanted amplitude modulation. Another PSCGH is demonstrated through silver L-shaped nanorods [5.17], where their

vertical and horizontal arms work for different polarization states. However, it falls into the category of binary amplitude hologram, and the twin-image cannot be avoided.

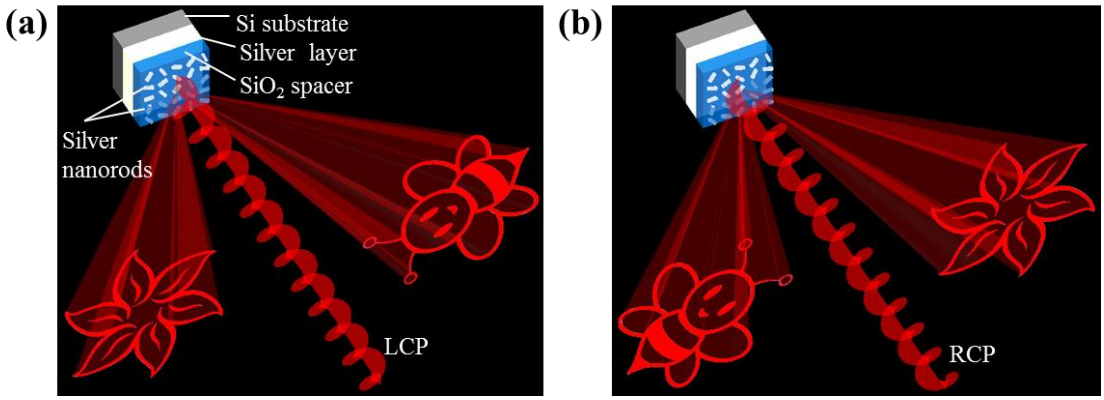

Figure 5.1 Schematics of the HMMH. The metasurface consists of three layers: the silver nanorods on the top, the SiO_2 layer in the middle and a silver ground layer at the bottom. (a) The reconstructed images of 'bee' and 'flower' are projected to different directions. (b) With the helicity reversion of the incident light, 'bee' and 'flower' swap their positions [5.9].

In this chapter, we demonstrate a PSCGH that is based on the reflection-type geometric metasurface. It shows distinct properties depending on the helicity of the incident light, and therefore it is named helicity multiplexed metasurface hologram (HMMH). Based on the off-axis design, two independent images can be reconstructed, and they have different projection angles. With the helicity reversion of the incident light, each reconstructed image flips around the normal of the HMMH and forms a mirror image on the opposite side [figure 5.1]. The HMMH shows advantages such as high efficiency and polarization contrast ratio, broadband, as well as the high quality images even in a large angular range.

5.2 Design of the HMMH

5.2.1 Theoretical explanations of the image switchable functionality

To generate a phase-only hologram, the Gerchberg−Saxton algorithm [5.18] proves to be a powerful tool. As shown in the flowchart (figure 5.2), the inverse Fourier transform of the target image is first obtained. The parameter Δ is introduced here with the expression

$$\Delta = Target - \left|FT\left[e^{i*Phase(A)}\right]\right|^2 \tag{5.1}$$

The loop terminates if Δ is within the error criterion, and the phase of A is extracted as the phase function for the phase-only hologram. Or else the loop continues to get the values of B, C, D and A.

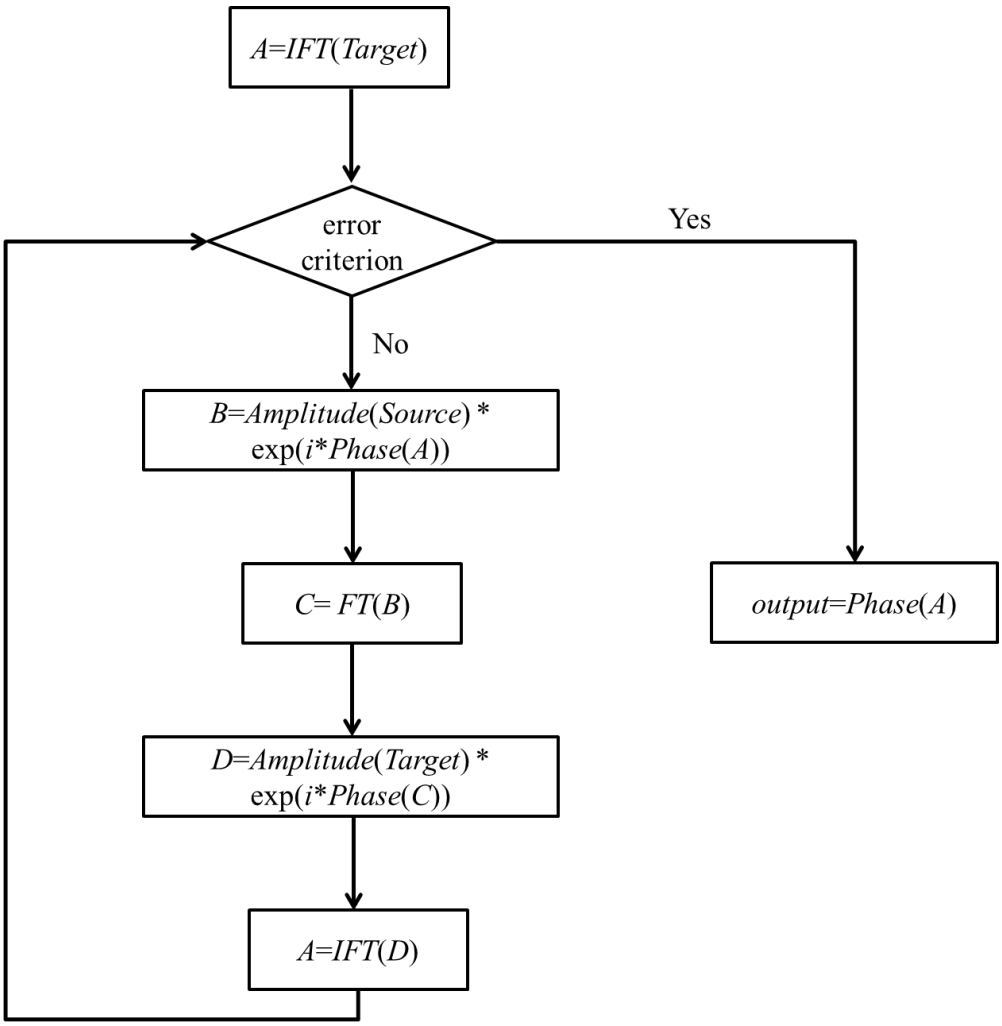

Figure 5.2 Flowchart of the Gerchberg−Saxton algorithm. *Target* and *Source* are the intensity distributions of the target image and light source, respectively. *FT* denotes the Fourier transform, and *IFT* represents the inverse Fourier transform. The functions of *Amplitude* and *Phase* extract the modulus and argument of a complex field, respectively [5.19].

The Gerchberg−Saxton algorithm is conventionally regarded as successful if the phase function $\varphi(x_0, y_0)$ of the phase-only hologram is retrieved, which reconstructs the target image

$$I(x,y) = A_0^2\left|FT[e^{i\varphi(x_0,y_0)}]\right|^2 \tag{5.2}$$

Here (x_0, y_0) and (x, y) denote the coordinates of the hologram and the observation plane, respectively. It is interesting to find that $I(x, y)$ changes into $I(-x, -y)$ if $\varphi(x_0, y_0)$ is added to a minus sign

$$A_0^2\left|F\left[e^{-i\varphi(x_0,y_0)}\right]\right|^2$$

$$= A_0^2\left|\iint_{-\infty}^{\infty} e^{-i\varphi(x_0,y_0)}e^{-i2\pi\left(f_x x_0+f_y y_0\right)}\,dx_0dy_0\right|^2$$

$$= A_0^2 \left| \left[\iint_{-\infty}^{\infty} e^{i\varphi(x_0,y_0)} e^{-i2\pi(-f_x x_0 - f_y y_0)} \, dx_0 dy_0 \right]^* \right|^2$$

$$= I(-x,-y) \tag{5.3}$$

where we have $f_x=x/\lambda z$ and $f_y=y/\lambda z$, which represent the x and y components of the wave vector, respectively. λ denotes the wavelength and z is the reconstruction distance. The change from $I(x, y)$ to $I(-x, -y)$ means that the reconstructed image is rotated by 180° around the image center (figure 5.3). This interesting property can give rise to many useful applications, as it does in the case of image switchable functionality that will be discussed in the next section.

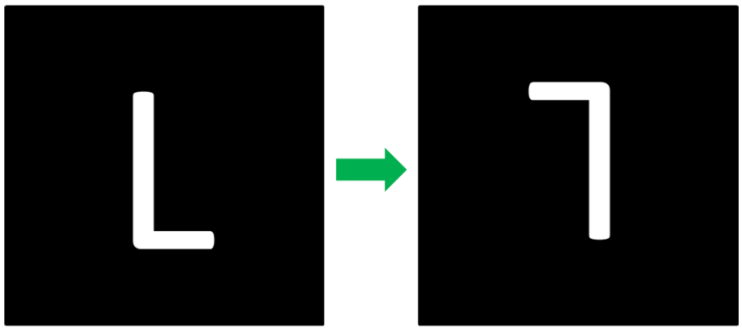

Figure 5.3 Schematics of the change from *I*(*x*, *y*) to *I*(*-x*, *-y*).

5.2.2 Realization of the helicity multiplexed functionality using a metasurface

Here another question arises: how to add a minus sign to the phase function $\varphi(x_0, y_0)$? As discussed in chapter 2, the positive or negative sign of the geometric phase is determined by the left- or right-handedness of the incident light, providing an exactly right solution to the question. Here the recently proposed reflection-type metasurface [5.20] is utilized to achieve the helicity multiplexed functionality. The reflection-type metasurface has nanorods on the top (each nanorod is 75nm wide, 200nm long and 30nm high), a SiO_2 spacer (80 nm) and a metallic ground layer (150 nm). Each nanorod can work as a reflection-type half-wave plate with the fast axis along the nanorod. The light converted by the reflection-type half-wave plate preserves the helicity of the incident circularly polarized light, and it is given an additional geometric phase of $\pm 2\varphi$ ('+' is valid for the conversion from LCP to LCP and '-' for that from RCP to RCP). Considering that the half-wave plate is non-ideal, there is also unconverted part, which has the opposite helicity and no geometric phase.

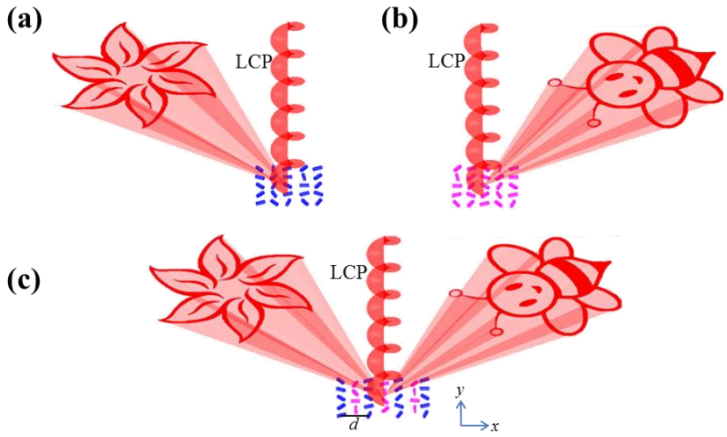

Figure 5.4 Design principle of the HMMH. The holographic 'flower' and 'bee' are projected to different sides of the LCP incident light by the metasurfaces in (a) and (b), respectively. Both metasurface holograms are designed based on the Gerchberg−Saxton algorithm. The two off-axis images are symmetrically distributed. (c) The two metasurfaces in (a) and (b) are merged, which can reconstruct 'flower' and 'bee' simultaneously [5.9].

The design principle of the HMMH is shown in figure 5.4. First, two phase-only metasurface holograms are generated by using the Gerchberg−Saxton algorithm, which can reconstruct the images of 'flower' and 'bee' and project them to different directions [figure 5.4(a-b)]. Then the two metasurfaces are merged as shown in figure 5.4(c). Since the blue nanorods correspond to 'bee' and the purple ones contribute to 'flower', both images can be reconstructed simultaneously. With the helicity reversion of the incident light, phase profiles of the reflected light from the three metasurfaces in figure 5.4 are all added to a minus sign, and the reconstructed images are rotated around the incident light to 180° (figure 5.5). As a result, the reconstructed image at a given position is switchable, i.e., either 'bee' or 'flower'.

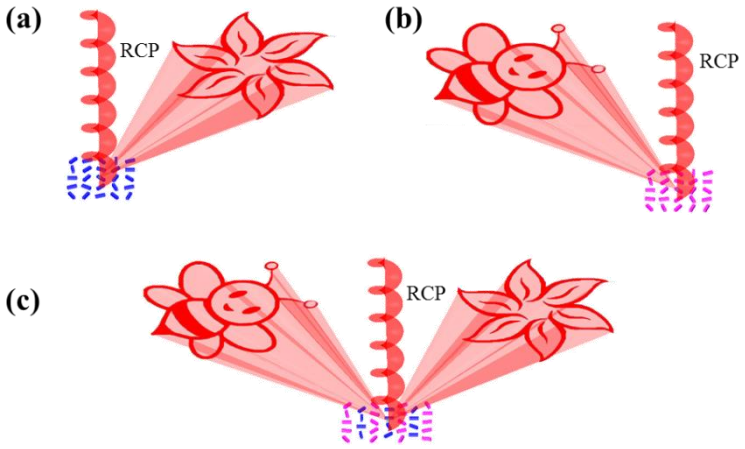

Figure 5.5 Reconstructed images of the HMMH with the RCP incident light [5.9].

Gold and silver are both conventional materials for metasurfaces. For example, gold is used in reference [5.20] to provide high conversion efficiency between 630 nm to

1050 nm. The plasmon frequencies for gold and silver are $13.8\times10^{15}s^{-1}$ and $14\times10^{15}s^{-1}$, respectively, which are very close to each other and they both lie in the ultraviolet region. However, their behaviors in the visible spectrum can be rather different due to the interband transitions, where bound electrons are excited to higher bands when working at high frequencies. As shown in figure 5.6, the absorptions of the blue and green light are much weaker for silver than that for gold. Therefore we conclude that silver is a better choice for the metasurfaces designed to operate in the full visible spectrum.

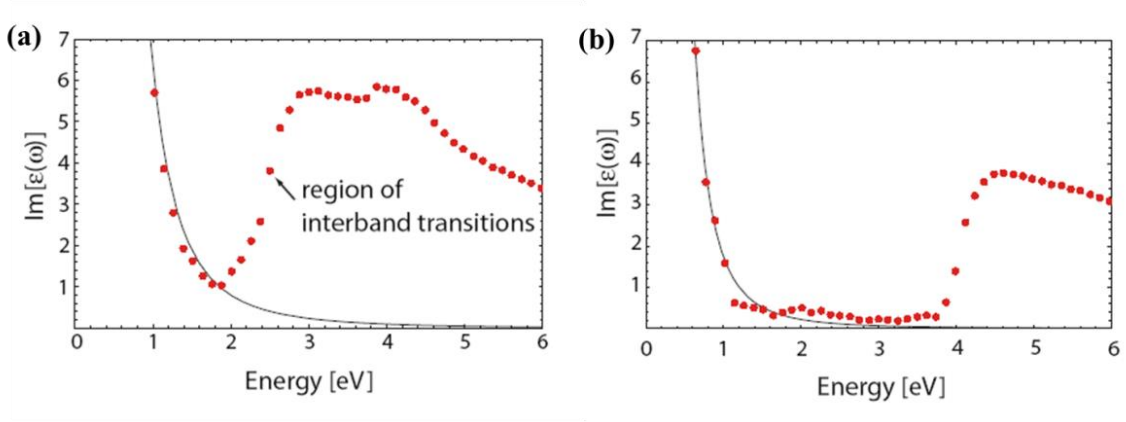

Figure 5.6 Imaginary part of the permittivity $\varepsilon(\omega)$ for gold and silver. The solid curves are obtained through the free electron gas model, and the dots represent the literature values. The mismatch between the curves and the dots are due to the interband transitions, which are not included in the free electron gas model. (a) Gold. (b) Silver [5.21].

5.3 Experimental characterizations of the HMMH

5.3.1 Design of the projection angles

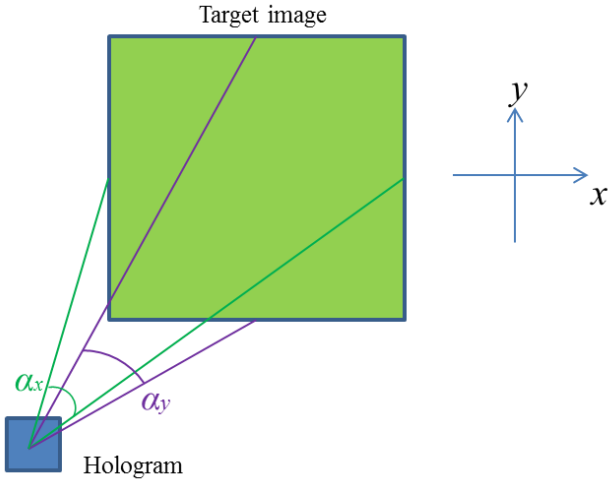

Figure 5.7 Schematics of the projection angles of the metasurface.

As shown in figures 5.4-5.5, the holographic images are projected out by the metasurface; therefore it is needed to find out the parameters of the metasurface that

determine the projection angles. The pixel numbers of the hologram and the holographic image are both assumed to be m in the x-direction and n in the y-direction. A single pixel in the hologram has the size of $P_{1x} \times P_{1y}$, and that in the holographic image is $P_{2x} \times P_{2y}$.

Since the holographic image can be regarded as a Fourier transform of the hologram, their respective pixel sizes have the following relationship

$$p_{2x} = \frac{\lambda z_0}{m p_{1x}} \tag{5.4}$$

$$p_{2y} = \frac{\lambda z_0}{n p_{1y}} \tag{5.5}$$

where λ is the designed wavelength, and z_0 is the reconstruction distance. As shown in figure 5.7, the holographic image is generated by a hologram with projection angles α_x and α_y. Therefore the following geometric relationship can be obtained

$$m p_{2x} = 2 z_0 \tan(\alpha_x/2) \tag{5.6}$$

$$n p_{2y} = 2 z_0 \tan\left(\alpha_y/2\right) \tag{5.7}$$

Combining equations (5.4)-(5.7), the projection angles α_x and α_y can be deduced as

$$\alpha_x = 2 arctan\left(\frac{\lambda}{2 p_{1x}}\right) \tag{5.8}$$

$$\alpha_y = 2 arctan\left(\frac{\lambda}{2 p_{1y}}\right) \tag{5.9}$$

For simplicity, the target images of ‘bee’ and ‘flower’ are both square with the pixel numbers m=n=531 (figure 5.8). The wavelength is 632.8 nm, and the pixel size of the hologram is 424 nm ×424 nm. According to equations (5.8)-(5.9), the projection angles are α_x=α_y=73.46°.

Figure 5.8 Binary target images of ‘bee’ and ‘flower’. The black and white pixels have the intensity values of 0 and 1, respectively.

By properly adjusting the locations of the 'bee' and 'flower' as shown in figure 5.8, the off-axis angles of the holographic images can be controlled accordingly. In this section, the designed projection angles are shown in figure 5.9.

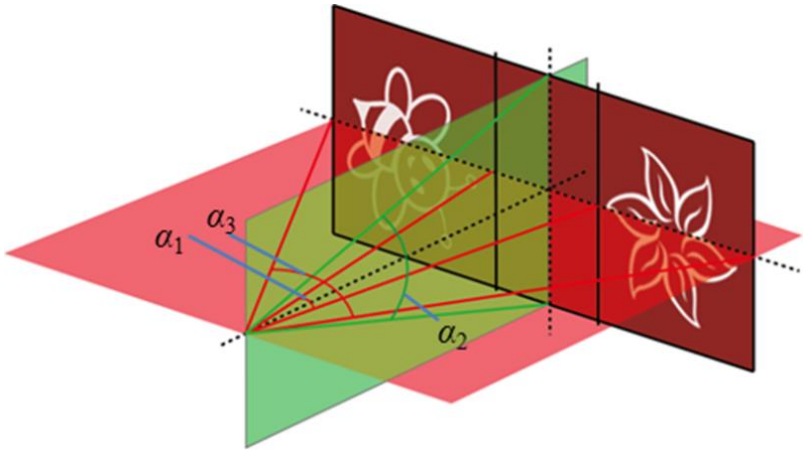

Figure 5.9 Projection angles of the merged hologram. The angles α_1/ α_2/ α_3 have the values of 20.7°/ 22°/ 64.7°[5.9].

5.3.2 Other concerns of the metasurface hologram

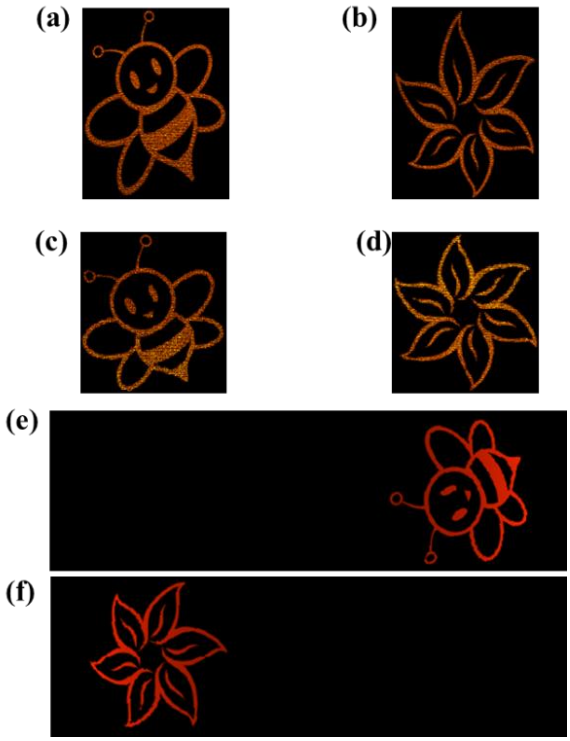

Figure 5.10 Compensation of the target images. The holographic images are simulated if the target images are (a-b) not compensated or (c-d) compensated. (e)-(f) The compensated target images [5.9].

Gerchberg−Saxton algorithm utilizes the paraxial approximation to simplify the propagation function between the hologram and the target image. However, the holographic images will be distorted when the projection angles are large enough [figures 5.10 (a)-(b)]. To reconstruct undistorted images [figure 5.10 (c)-(d)] in the far

field, the target images have to be compensated in advance as shown in figures 5.10 (e)-(f).

It is reported that in the case of Fourier elements, the replication of the basic element does not change the overall diffraction pattern, but increases the SNR [5.22]. Therefore the merged hologram is arranged in a 2×2 periodic array (figure 5.11), and the total size of the metasurface hologram will be 450 μm×450 μm.

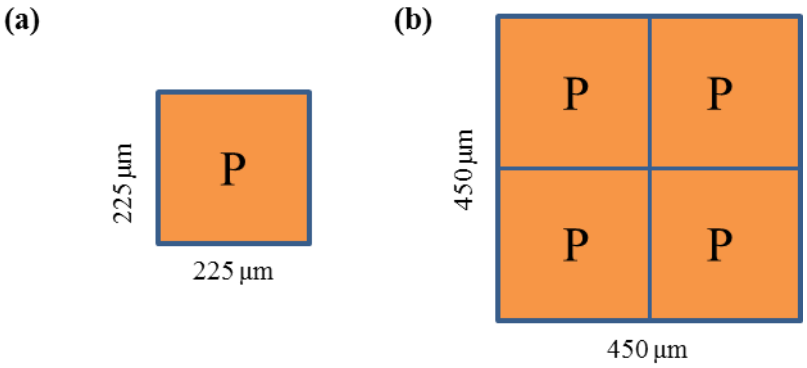

Figure 5.11 Replication arrangement of the hologram. (a) The merged metasurface has the size of 225 μm × 225 μm. (b) By placing the merged metasurface into a 2×2 periodic array, the reconstructed image will not be changed, but the laser speckles will be greatly suppressed.

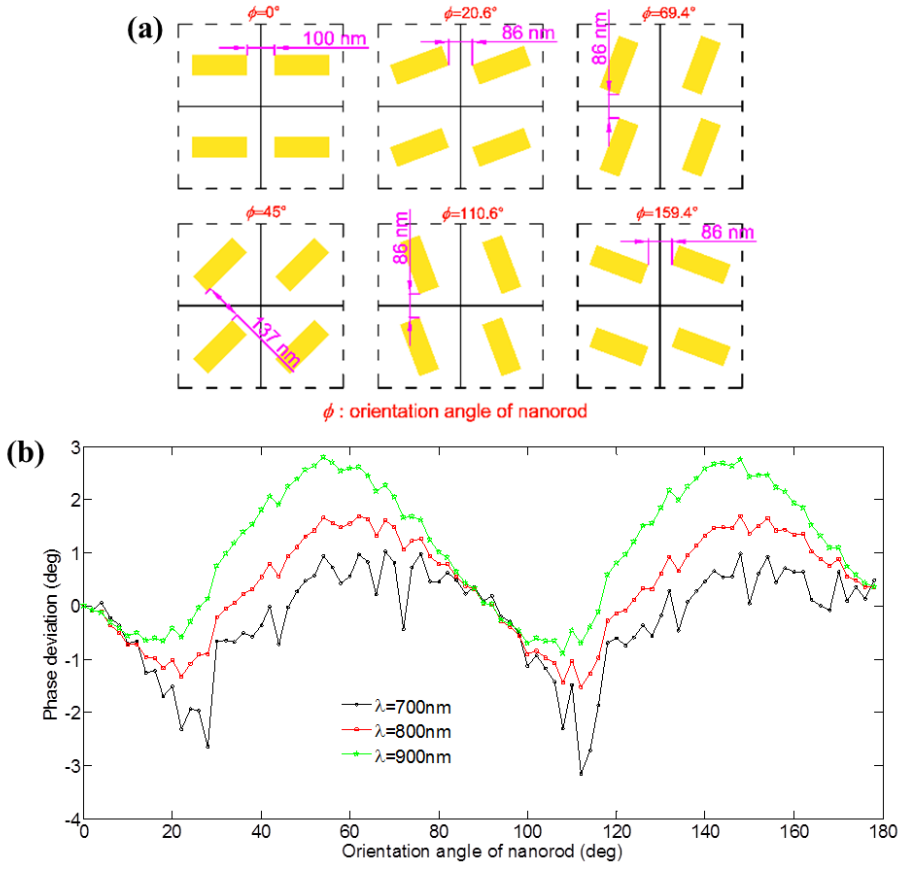

Figure 5.12 Near-field coupling of the nanorods. (a) The uniform arrays of nanorods with different orientations are used as examples. (b) Simulated phase deviation versus the orientations of the nanorods in (a) [5.9].

The nanorods in the metasurface are densely packed, hence the near field coupling has to be considered. Here the coupling effect is evaluated by calculating the phase deviations from the designed value 2φ, which is the ideal geometric phase. As shown in figure 5.12(a), uniform arrays of nanorods are used as examples, and d_1 is the distance between the nearest corners of the neighboring nanorods. Figure 5.12(b) shows that the peaks of the phase deviation curve correspond to the smallest values of d_1, and the maximum phase deviation is within $\pm 3^{\circ}$. Although the number of phase levels is not limited when we use the geometric phase, here the 16 phase levels are used as shown in figure 5.13. In comparison with the phase step of $\pi/8$, the maximum phase deviation caused by the coupling is much less and therefore can be ignored [5.20].

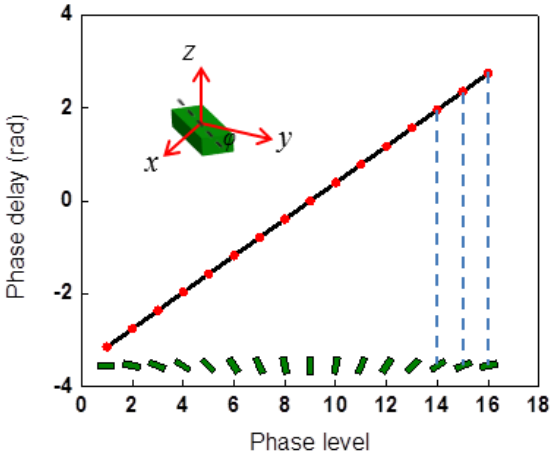

Figure 5.13 Schematic of the phase steps. 16 phase levels are adopted to make sure that the near field coupling is much less than the phase step [5.9].

5.3.3 Experimental setup and the reconstructed images versus the polarization state of the incident light

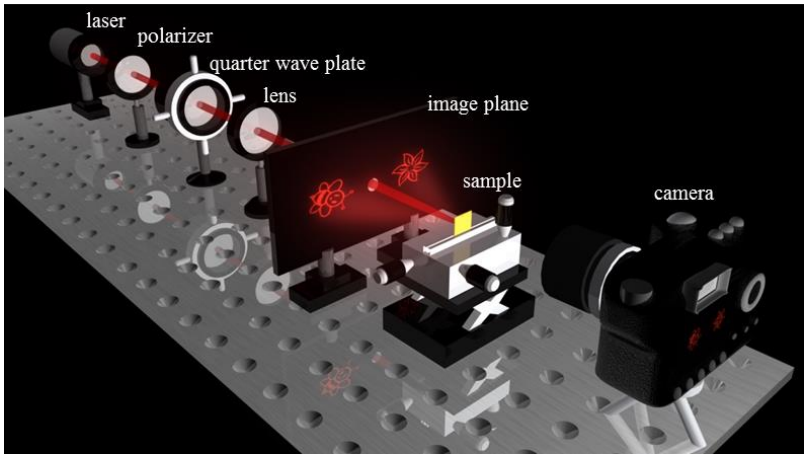

Figure 5.14 Experimental setup to characterize the HMMH. The light comes from a supercontinuum laser, and its polarization state is adjusted by a polarizer and a quarter-wave plate. Then it passes through an opening on the screen and shines on the sample. The holographic images on the screen are captured by a camera [5.9].

The experimental setup to characterize the HMMH is shown in figure 5.14. The light source is a supercontinuum laser (Fianium-SC400-PP), which covers the visible and near infrared range. A polarizer and a quarter-wave plate are used to change the incident light polarization. Then the light is slightly focused by a lens and passes through an opening on the screen. The metasurface to be tested is fastened to a three dimensional translational stage. Due to the off-axis design of the metasurface hologram, the reflected light contributing to the holographic images will be projected onto the screen. The unconverted light is reflected back and passes through the opening again; hence it does not affect the quality of the reconstructed images. The size of the reconstructed images grows with the reconstruction distance, so the images are large enough to be captured by a normal camera.

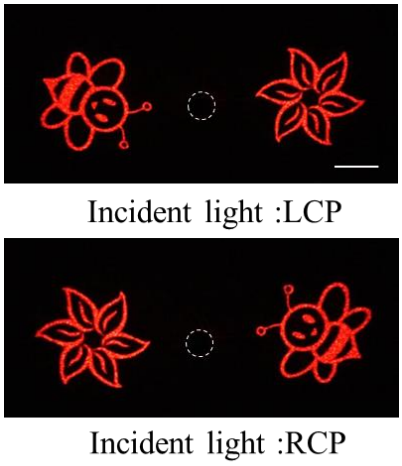

Figure 5.15 Reconstructed images for the LCP and RCP incident light at 633 nm. The opening on the screen is marked out. The scale bar is 1 cm [5.9].

Figure 5.15 shows the images captured on the screen at 633 nm. The reconstruction distance is set to be 5 cm. It shows that the patterns of 'bee' and 'flower' rotate 180° around the image center with the helicity reversion of the incident light, which agrees well with the prediction. Also, the reconstructed 'bee' and 'flower' patterns have high fidelity in comparison with the target images.

The cases for the pure RCP or LCP incident light are shown in figure 5.15. However, the situation changes with other polarization states. Here the evolution of the images on the right side of the screen is taken as an example. At first, there are only 'flower' with LCP incident light [figure 5.16(a)]. Then a dim 'bee' begins to appear since a subtle RCP component is introduced into the left-handed elliptically polarized light [figure 5.16(b)]. For the linear polarization, which has equal orthogonal circular polarizations, the 'bee' and 'flower' patterns also have the equal amplitude [figure 5.16(c)]. After that, the 'bee' turns to be brighter than 'flower' since the right-handed elliptically polarized

light has more RCP component [figure 5.16(d)]. Finally, only 'bee' is observed on the right side when the incident light changes to RCP [figure 5.16(e)]. Overall, since all the intermediate polarization states in figures 5.16(b)-(d) can be regarded as a superposition of the two orthogonal circular components, the corresponding images can be regarded as superpositions of figures 5.16(a) and (e) with different coefficients.

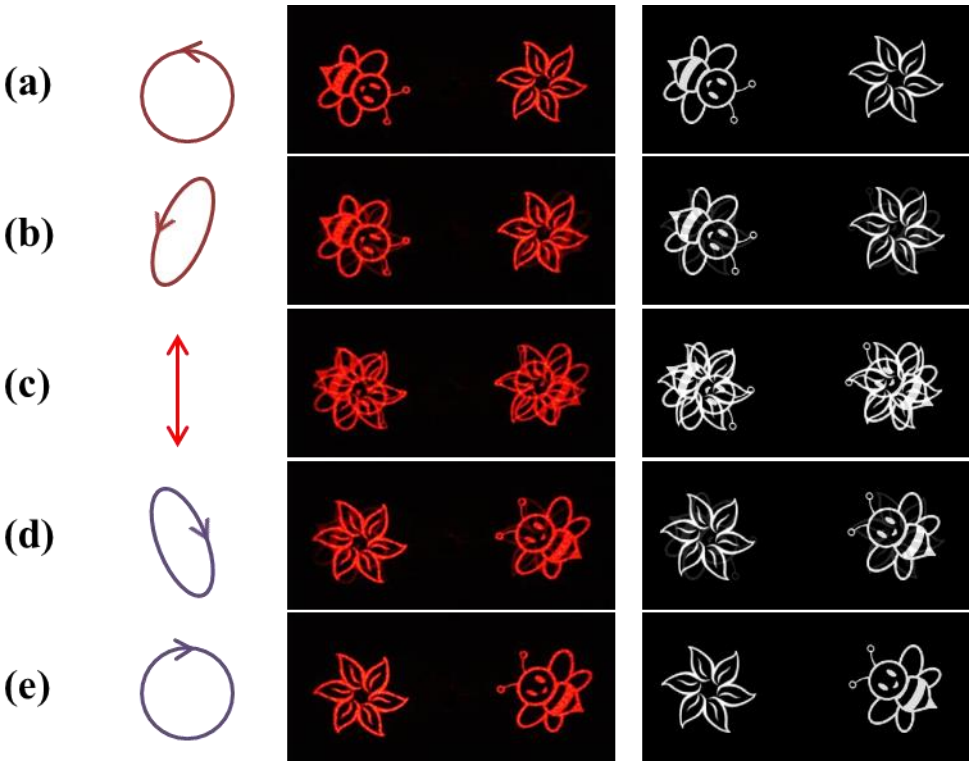

Figure 5.16 Reconstructed images versus the evolution of the incident light polarization. The left column shows the schematics of the polarization ellipse. The middle and right columns show the experiment and simulation results, respectively [5.9].

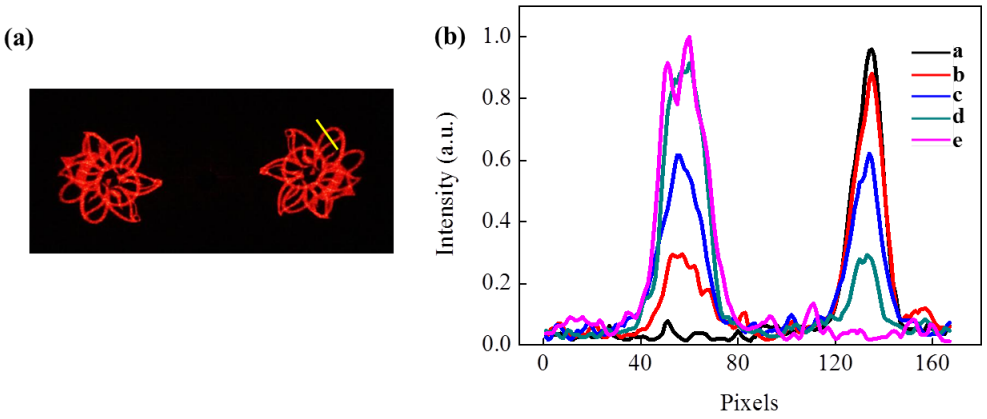

Figure 5.17 Evolution of the images versus the polarization of the incident light. (a) A short line crosses the patterns of 'bee' and 'flower' simultaneously. (b) The five lines a-e correspond to the polarization states in figures 5.16(a)-(e), respectively. The horizontal axis represents the pixel numbers on the line, and the vertical axis is the normalized intensity [5.9].

In the following, the evolution of the images versus the incident light polarization is quantitatively analyzed. Assuming that there is a line on the right side of the screen, which crosses part of the 'flower' and 'bee' patterns [figure 5.17(a)], then the intensity along this line is studied for different polarization states. The five lines with different colors in figure 5.17(b) correspond to the five polarization states in figure 5.16. The peaks around the 55th and 135th pixels represent the intensity of the 'bee' and 'flower', respectively. It intuitionally shows that intensity of 'flower' decreases while that of the 'bee' pattern increases when the incident light gradually changes from LCP to RCP.

5.3.4 Image quality and efficiency of the HMMH

As mentioned in section 4.3, the SNR is important to characterize the quality of a holographic image. Here the SNR is defined as the ratio between the peak intensity of the reconstructed image and the standard deviation of the background noise [5.23]. The background is chosen to be the dark areas around the reconstructed image. The off-axis design enables the unconverted light to be reflected back through the hole on the screen, and it barely affects the reconstructed images. The SNR is measured to be 43.5 for the image in figure 5.16(a). In comparison with the reported SNR value of 24.4 [5.23], the image obtained here shows a significant improvement in the background noise suppression.

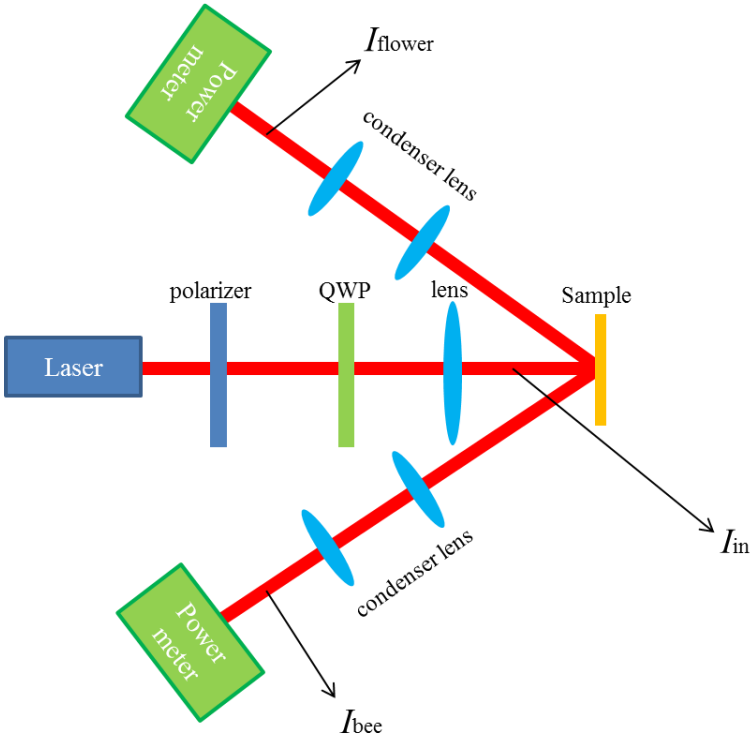

Figure 5.18 Experimental setup for the efficiency measurement.

The experimental setup for the efficiency measurement is shown in figure 5.18. Since the size of the reconstructed image grows fast with the propagation distance, a pair of condenser lens (Ø45 mm, f=32.1 mm, NA=0.60) are used to collect the entire image of 'bee' or 'flower'. The conversion efficiency of the metasurface is calculated as the intensity of the reflected light contributing to the holographic images divided by that of the incident light:

$$\eta=(I_{\text{bee}}+I_{\text{flower}})/(pI_{\text{in}}) \tag{5.10}$$

where p represents the transmissivity of the condenser lenses pair. The efficiency is measured from 475 nm to 1100 nm [figure 5.19], and the peak efficiency is located at 960 nm with the value of 40%.

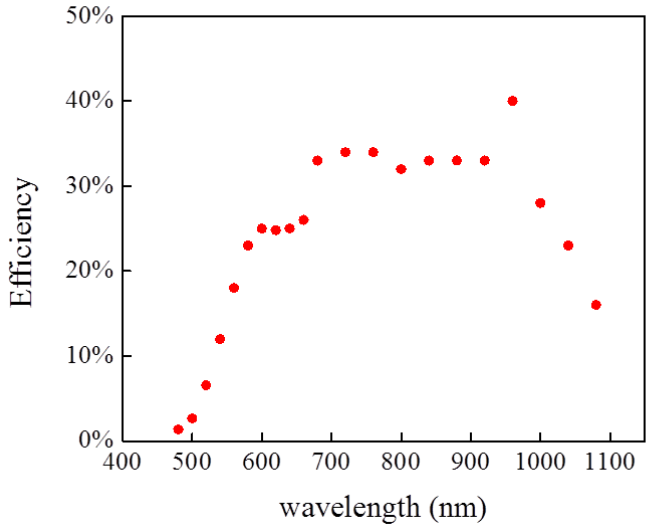

Figure 5.19 Measured conversion efficiency of the metasurface [5.9].

5.4 Optimized design of the HMMHs

5.4.1 Design principle

The design method proposed in section 5.2 provides a unique way to integrate two different functionalities into a single device. However, the same helicity multiplexed functionality can be realized with higher conversion efficiency by utilizing an optimized design principle. As shown in figure 5.20, the target image for the optimized design contains both the 'bee' and 'flower', which is different from the target images in figure 5.8. Then Gerchberg−Saxton algorithm is used to retrieve the phase profile that contributes to 'bee' and 'flower' simultaneously. With the reversion of the incident light helicity, the reconstructed image rotates 180° around the image center, which is similar to that in figures 5.4-5.5.

Figure 5.20 Target image of the optimized design.

To show the difference between the original design and the optimized design, the angular spectrum representation is used to analyze the complex field distribution across the metasurface plane. It is known that a two-dimensional monochromatic field $U(x,y)$ can be Fourier-transformed, and the obtained angular spectrum represents a series of plane waves propagating in different directions away from that field

$$A(f_x, f_y) = \iint_{-\infty}^{\infty} U(x,y) exp\left[-i2\pi\left(f_x x + f_y y\right)\right] dxdy \tag{5.11}$$

The parameters f_x and f_y are the spatial frequencies along the x- and y- directions, respectively, and they are related to the direction cosines a the plane wave by

$$f_x = \frac{cos\alpha}{\lambda} \tag{5.12}$$

$$f_y = \frac{cos\beta}{\lambda} \tag{5.13}$$

where α (β) represents the angle formed by the wave vector of the plane wave and the x- (y-) axis. If we have

$$f_x{}^2 + f_y{}^2 < \frac{1}{\lambda^2} \tag{5.14}$$

The planar wave is a propagating wave, and its travel over the distance z only adds a phase shift without affecting the amplitude. Or else if

$$f_x{}^2 + f_y{}^2 > \frac{1}{\lambda^2} \tag{5.15}$$

The wave is an evanescent wave, whose amplitude decreases with the propagation distance. Therefore only the propagating waves contribute to the holographic image in the far field. Equations (5.14)-(5.15) denote that the propagation of plane waves is

limited by a spatial frequency filter as shown in figure 5.21, and the edge of the circle represents the cut-off frequencies.

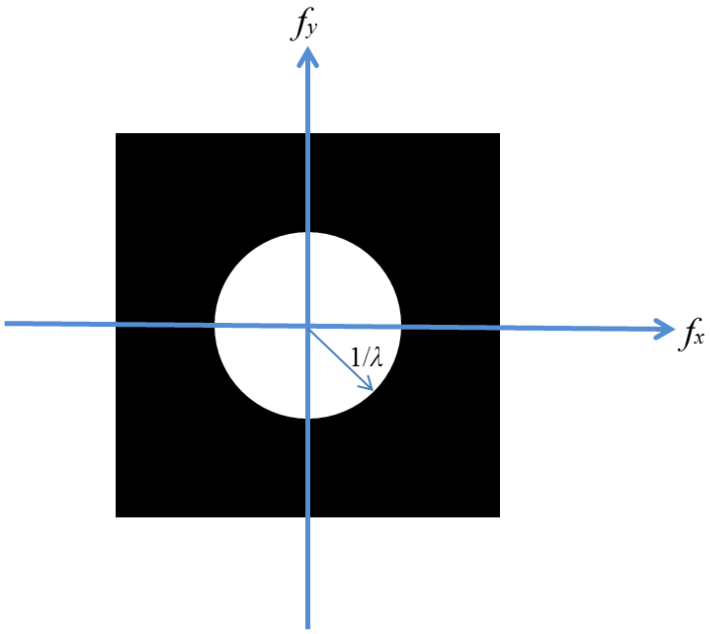

Figure 5.21 Spatial frequency limitations to the plane wave propagation.

If the metasurface is under the illumination of a plane wave, the reflected light has the complex field distribution in the metasurface plane

$$U(x,y) = A_1 e^{\pm i\varphi(x,y)} \tag{5.16}$$

where A_1 represents the amplitude of the reflected light, and $\varphi(x, y)$ denotes the phase profile. The positive or negative sign is valid for the left- or right- helicity, respectively. According to the equation (5.11), Fourier transform is applied to $U(x, y)$ to obtain the angular spectrum $A(f_x, f_y)$ of the reflected light.

The phase profiles of the reflected light in figures 5.4(a), (b) and (c) are first analyzed, and their angular spectrums are shown in figures 5.22(a), (b) and (c), respectively. Then the angular spectrum of the reflected light from the optimized metasurface is obtained [figure 5.22(d)]. In comparison with figures 5.22(a)-(b), figure 5.22(c) shows that the merging process transfers a great part of energy to the higher spatial frequencies. In contrast, most of the energy is still located at low frequencies for the optimized design [figure 5.22(d)].

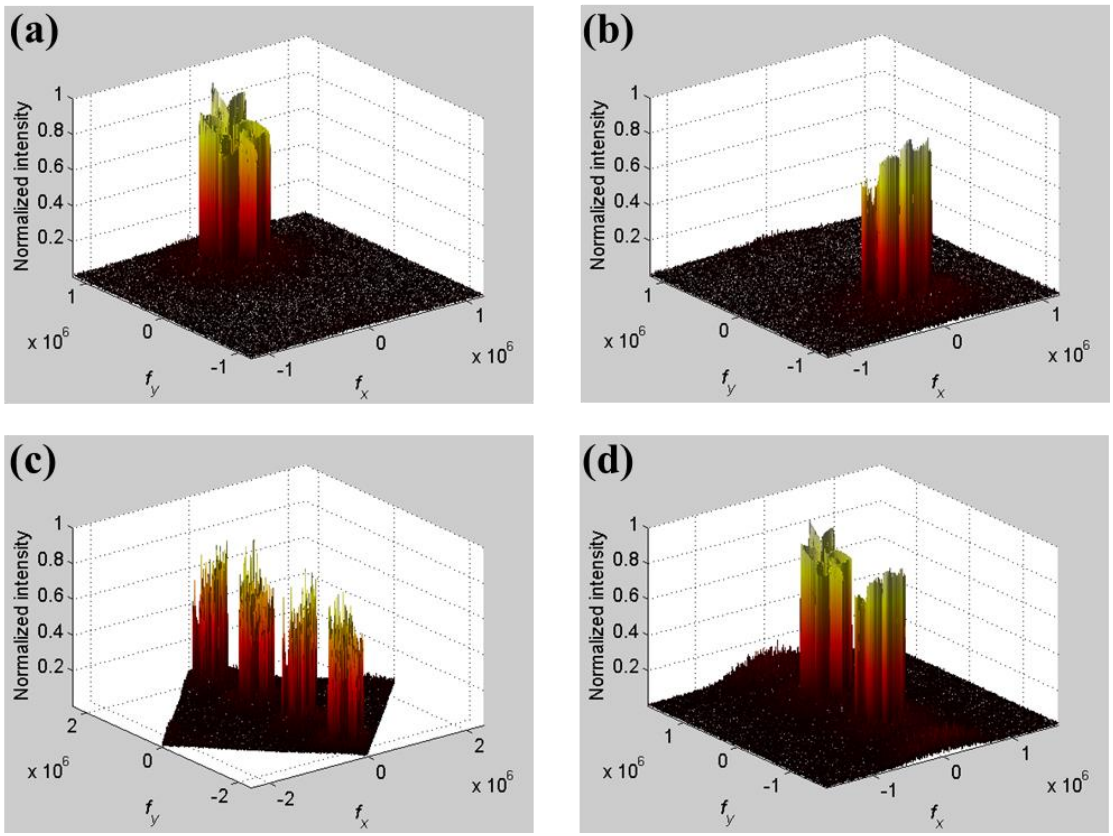

Figure 5.22 Normalized angular spectrums for different metasurfaces. (a)-(c) Angular spectrums corresponding to the reflected light in figures 5.4(a), (b) and (c), respectively. (d) Angular spectrum of the reflected light from the optimized metasurface [5.9].

Comparing figure 5.21 with figure 5.22(c), it shows that a significant part of high spatial frequencies is filtered out by the frequency filter for the wavelengths between 475 nm to 1100 nm. Besides, the high frequencies loss increases with the wavelengths, which are inversely proportional to the cut-off frequencies. On the contrary, the optimized design faces much less high frequencies loss [figure 5.22(d)], and the majority of energy contributes to the holographic image.

5.4.2 Efficiency of the optimized metasurface

The efficiency of the optimized metasurface is measured (figure 5.23), which shows a significant improvement in comparison with the original design (figure 5.19). The efficiency is over 40% for the wavelengths between 620 nm and 1020 nm. The peak efficiency is located at 860 nm with the value of 59.2%, and the experimentally measured SNR is 73.8 at 633 nm.

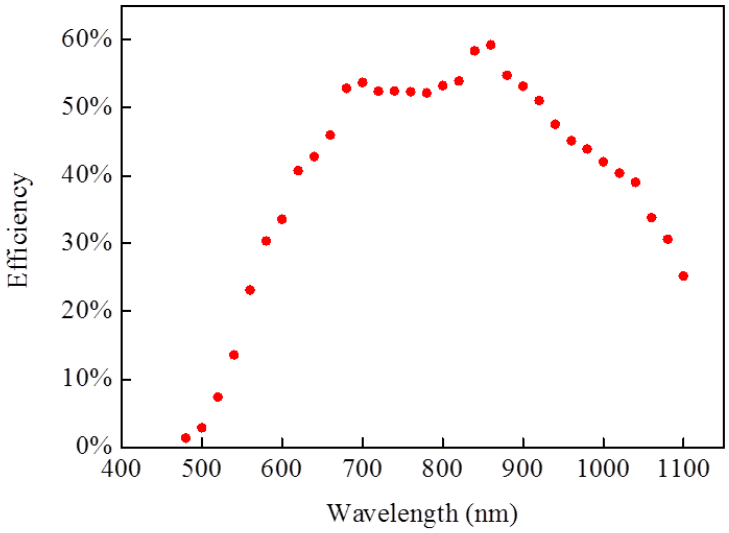

Figure 5.23 Measured efficiency of the metasurface with the optimized design [5.9].

By using the FDTD method, the conversion efficiency is simulated as shown in figure 5.24. The red curve denotes that the majority part of the incident light is converted by the metasurface, and the unconverted part (blue curve) has low amplitude for a broad wavelength range.

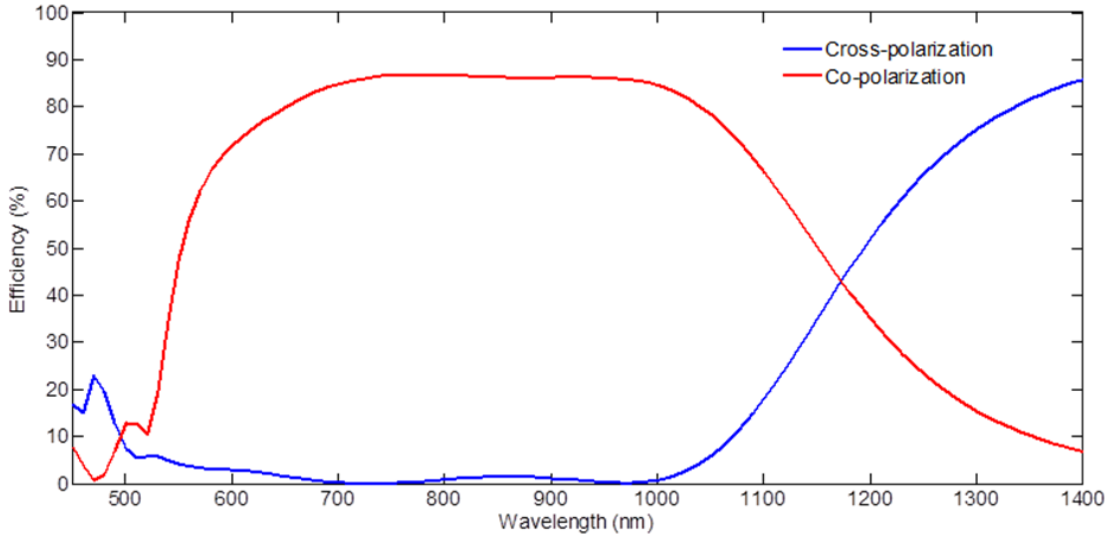

Figure 5.24 Simulated conversion efficiency of the metasurface [5.9]. The blue (red) curve represents the efficiency of the reflected light which has the opposite (same) helicity as the incident light.

The simulated conversion efficiency is higher than that of the experimental results. There are three main reasons accounting for the lower experimental values: First, the fabrication errors, such as the nanorod distortion and the defects in the SiO_2 layer (figure 5.25) make the metasurface different from the initial design. Second, since a titanium layer (~1 nm) is added above the SiO_2 layer to increase its adhesion to the

silver nanorods, the conversion efficiency is therefore decreased as titanium is a highly lossy material (figure 5.26). Finally, the holographic image has a wide projection angle, which makes the efficiency measurement difficult. The measured efficiency values are very sensitive to the positions of the condenser lenses (figure 5.18), and the error in the measurement system is hard to avoid.

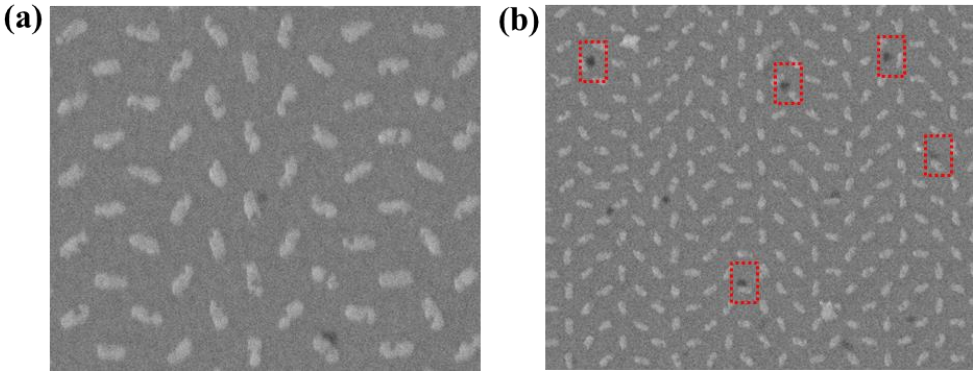

Figure 5.25 Fabrication errors of the metasurface. (a) The nanorods deviate from the designed rectangular shape. (b) The defects in the SiO_2 layer [5.9].

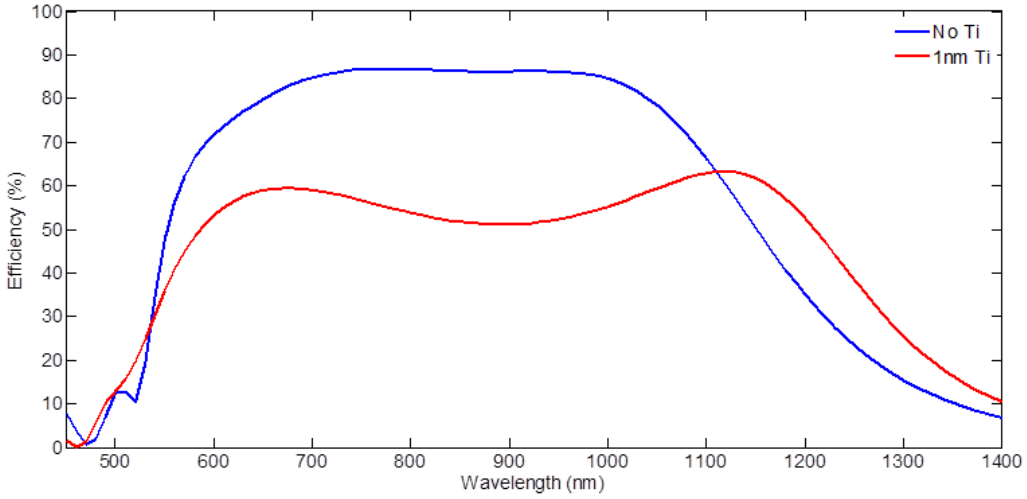

Figure 5.26 Simulated conversion efficiency for metasurface with or without titanium layer [5.9]. The red (blue) curve represents the simulated conversion efficiency of the metasurface, which is with (without) titanium layer between the nanorods layer and the SiO_2 spacer.

The reflection-type metasurface functions like a Fabry–Pérot cavity as illustrated in chapter 2. However, the resonance condition in the Fabry–Pérot cavity deviates from the original design if the incident light is tilted. Here we measure the conversion efficiency of the metasurface for different incident angles (figure 5.27), and the result shows that the efficiency decreases with the increase of the incident angle.

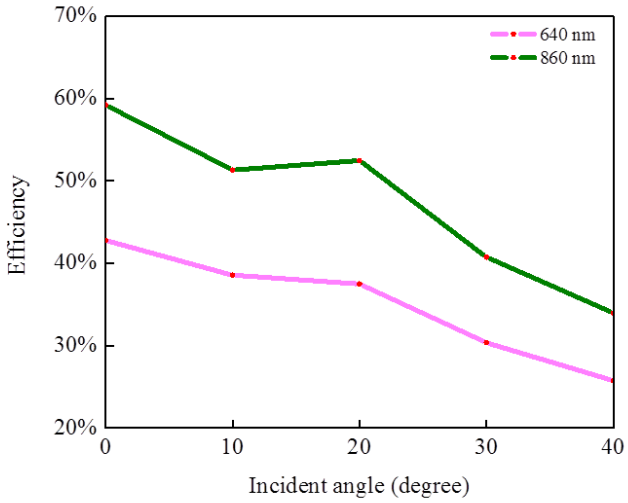

Figure 5.27 Experimentally obtained conversion efficiency of the metasurface for the incident light at different incident angles [5.9].

Although it is challenging for the metasurface holograms proposed in the literature to generate clear images within the whole visible wavelength range, the metasurface proposed here can reconstruct fine images by using blue (475 nm) and green (524 nm) lasers (figure 5.28).

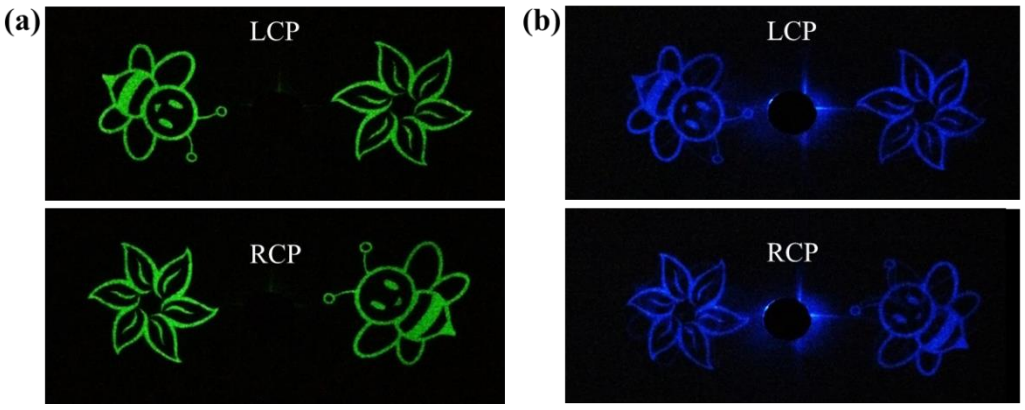

Figure 5.28 Experimentally obtained holographic images at (a) 524 nm and (b) 475 nm [5.9].

5.5 Conclusions

In conclusion, a metasurface hologram with helicity multiplexed functionality is demonstrated, which is of great interest from the practical point of view. The HMMH is realized by merging two arrays of nanorods into a single device, or by placing two different patterns on the same target image, which are straightforward for both design and fabrication. Furthermore, the reflection metasurfaces provide high efficiency and broadband performance. The clear images of blue, green and red colors unambiguously demonstrate its potential for the applications in the visible range. Since several major concerns regarding the image fidelity, efficiency and bandwidth are addressed by the

HMMH proposed here, it may facilitate the applications of polarization selective devices such as data storage, information processing, and microscopy.

5.6 References

5.1 F. Xu, J. E. Ford, Y. Fainman, *Polarization-selective computer-generated holograms: design, fabrication, and applications*. Appl. Opt. **34**, 256-266 (1995).

5.2 A. V. Krishnamoorthy, F. Xu, J. E. Ford, Y. Fainman, *Polarization-controlled multistage switch based on polarization-selective computer-generated holograms*. Appl. Opt. **36**, 997-1010 (1997).

5.3 J. E. Ford, F. Xu, K. Urquhart, Y. Fainman, *Polarization-selective computer-generated holograms*. Opt. Lett. **18**, 456-458 (1993).

5.4 W. Yu, T. Konishi, T. Hamamoto, H. Toyota, T. Yotsuya, Y. Ichioka, *Polarization-multiplexed diffractive optical elements fabricated by subwavelength structures*. Appl. Opt. **41**, 96-100 (2002).

5.5 J. Scheuer, Y. Yifat, *Holography: Metasurfaces make it practical.* Nat. Nano. **10**, 296-298 (2015).

5.6 J. Lin, et al. *Polarization-Controlled tunable directional coupling of surface plasmon polaritons*. Science **340**, 331-334 (2013).

5.7 X. Z. Chen, et al. *Dual-polarity plasmonic metalens for visible light*. Nat. Commun. **3**, 1198 (2012).

5.8 Y. Zhao, A. Alu, *Tailoring the dispersion of plasmonic nanorods to realize broadband optical meta-waveplates*. Nano Lett. **13**, 1086-1091 (2013).

5.9 D. Wen, et al. *Helicity multiplexed broadband metasurface holograms*, Nat. Commun. **6**, 8241 (2015).

5.10 X. B. Yin, Z. L. Ye, J. Rho, Y. Wang, X. Zhang, *Photonic spin Hall effect at metasurfaces*. Science **339**, 1405-1407 (2013).

5.11 Z. H. Jiang, et al. *Broadband and Wide field-of-view plasmonic metasurface-enabled waveplates*. Sci. Rep. **4**, 7511 (2014).

5.12 Y. Yang, I. I.Kravchenko, D. P. Briggs, J. Valentine, *All-dielectric metasurface analogue of electromagnetically induced transparency*. Nat. Commun. **5**, 5753 (2014).

5.13 Y. Yao, et al. *Electrically Tunable Metasurface Perfect absorbers for ultrathin mid-infrared optical modulators*. Nano Lett. **14**, 6526-6532 (2014).

5.14 S. F. Shi, et al. *Optimizing Broadband Terahertz modulation with hybrid graphene/metasurface structures*. Nano Lett. **15**, 372-377 (2015).

5.15 F. Ding, Z. Wang, S. He, V. M. Shalaev, A. V. Kildishev, *Broadband high-efficiency half-wave plate: A supercell-based plasmonic metasurface approach*. ACS NANO **9**, 4111-4119 (2015).

5.16 W. T. Chen, et al. *High-efficiency broadband meta-hologram with polarization-controlled dual Images*. Nano Lett. **14**, 225-230 (2014).

5.17 Y. Montelongo, J. O. Tenorio-Pearl, W. I. Milne, T. D. Wilkinson, *Polarization switchable diffraction based on subwavelength plasmonic nanoantennas*. Nano Lett. **14**, 294-298 (2014).

5.18 R. W. Gerchberg, W. O. Saxton, *A Practical Algorithm for the determination of phase from image and diffraction plane pictures*. OPTIK **35**, 237-246 (1971).

5.19 https://en.wikipedia.org/wiki/Gerchberg%E2%80%93Saxton_algorithm.

5.20 G. Zheng, H. Mühlenbernd, M. Kenney, G. Li, T. Zentgraf, S. Zhang, *Metasurface holograms reaching 80% efficiency*. Nat. Nano.**10**, 308-312 (2015).

5.21 S. Maier, Plasmonics: *Fundamentals and Applications*. Springer: New York, 2007.

5.22 B. C. Kress, P. Meyrueis, *Applied digital optics: from micro-optics to nanophotonics*. John Wiley & Sons: West Sussex, 2009.

5.23 X. Ni, A. V. Kildishev, V. M. Shalaev, *Metasurface holograms for visible light*. Nat. Commun. **4**, 2807 (2013).

Chapter 6 Geometric phase induced broadband optical rotation

In this chapter, a broadband optical rotation device is proposed and experimentally verified using the geometric metasurface-based rectangular phase grating. The grating responds differently to the LCP and RCP incident light, which provides a degree of freedom to control the optical rotation angle of the reflected light. The design method, along with its high performance within the visible and near infrared range can facilitate the application of optical rotation devices in integrated optical systems.

6.1 Introduction

Optical rotation occurs when a beam of light passes through certain materials that respond differently to the LCP and RCP light, thereby rotating the polarization angle of the incident light [6.1]. Many useful applications such as concentration determination [6.2] and organic structure analysis [6.3, 6.4] are based on the measurement of optical rotation angles. Conventionally, optical rotation is observed in chiral materials, which lack microscopic mirror symmetry, such as quartz or sugar solutions. However, since the optical rotation functionality is generally weak in the naturally occurring materials, a distance much longer than the operating wavelength is needed to provide notable optical rotation angles. Faraday rotation is a magneto-optical phenomenon that causes slightly different speeds of the LCP and RCP light beams, but the size of a Faraday rotator is also limited by the available magneto-optical materials.

Optical metamaterials derive their properties from the structures rather than the component materials. By using artificial structures that are different from their mirror images, 3D chiral metamaterials open up new avenues to manipulate optical rotation [6.5-6.8]. However, the fabrication of 3D metamaterials faces technical challenges, especially when they are designed to work in the visible and near infrared range. 2D metamaterials, or metasurfaces [6.9-6.13], can be designed to have chirality with much simpler fabrication processes [6.14, 6.15], but the magnitude of the rotation angle is limited. Besides the chirality-induced optical rotation, a non-chiral metasurface can also be used to realize optical rotation [6.16]. The metasurface consists of two subunits of nanorods with a spatial displacement between them. The linearly polarized incident light is decomposed into LCP and RCP components with a phase difference proportional to the spatial displacement. The optical rotation is realized through collective operation of all the non-chiral nanoantennas rather than the chirality of each antenna. This method provides an effective way to rotate the polarization angle of the scattered light, whose wavelength is larger than the two times of p (p is the pixel pitch

of the metasurface). Nevertheless, the scattered light beam with a wavelength shorter than 2*p* will be shifted away from the designed plane of refraction due to the spatial arrangement of the two subunits. Furthermore, the efficiency of the transmission-type plasmonic metasurface is very low as mentioned in chapter 2. Therefore, a new way to realize arbitrary optical rotations with high efficiency and broadband performance is highly needed.

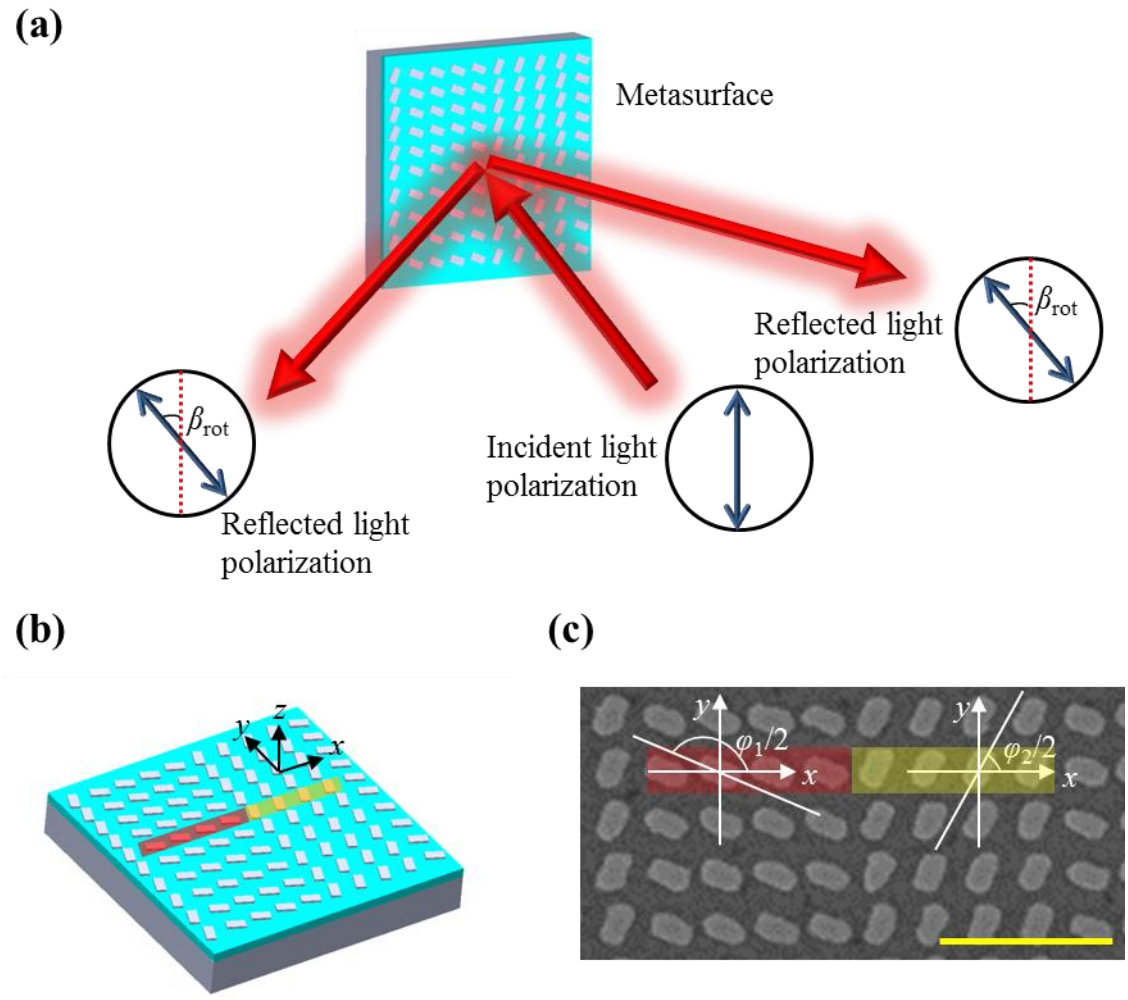

Figure 6.1 The reflection-type geometric metasurface designed for optical rotation. (a) A linearly polarized light beam is incident normally onto the metasurface, each order of the reflected light remains to be linearly polarized but with an optical rotation angle β_{rot}. Here β_{rot} is defined as the angle between the oscillation direction of the reflected light and the vertical direction of the reflection plane. (b) Schematic and (c) SEM image of the designed metasurface. The nanorods colored with red and yellow form angles of φ_1 /2 and φ_2 /2 with the *x*-axis, respectively. The scale bar is 1μm. All the nanorods have the same length (200 nm), width (75 nm) and thickness (30nm). The pixel pitch is 300 nm.

In this chapter, a method is demonstrated to achieve the optical rotation using a non-chiral reflection-type geometric metasurface. A metasurface-based rectangular phase grating can separate the incident light into two orthogonal circular components, and

give a designed phase difference to them. The superposition of the RCP and LCP light then forms a new light beam with a rotated polarization angle [figure 6.1(a)]. The high efficiency and broadband performance of the proposed device make it potential for practical applications.

6.2 Design principle of the metasurface for optical rotations

First, a rectangular phase grating is realized by using a reflection-type geometric metasurface, which consists of a silver nanorod layer on the top, a SiO_2 spacer in the middle and a silver ground layer at the bottom. Each supercell contains eight nanorods: the first four have the same orientation angle of $\varphi_1/2$, and the last four have the angle of $\varphi_2/2$ [figures 6.1(b)-(c)]. If the metasurface is under the illumination of RCP light, the reflected RCP light from a supercell will be given geometric phases of φ_1 and φ_2, which agree with the rectangular-shaped phase curve in figure 6.2(a).

The reflection coefficient of the rectangular phase grating with the RCP incident light is [6.21, 6.22]

$$t(x_0, y_0) = \left(e^{i\varphi_1} - e^{i\varphi_2}\right) rect\left(\frac{x_0}{a}\right) * \frac{1}{d} comb\left(\frac{x_0}{d}\right) + e^{i\varphi_2} \tag{6.1}$$

Here (x_0, y_0) is used to represent the coordinates in the grating plane. The parameter a is the length of the phase step φ_1, and d is the period length. The function *rect* represents a rectangular function. The value of *rect* (x_0/a) equals to 1 if $|x_0| \leq a$, or else it equals to 0. *comb* denotes the periodically distributed Dirac delta functions. If a planar wave is incident onto the rectangular phase grating and modulated by $t(x_0, y_0)$, the reflected light in the far field with a distance z will have the field distribution

$$U(x_1, y_1) = \frac{1}{i\lambda z} e^{ikz} e^{\left[i\frac{k}{2z}(x_1^2 + y_1^2)\right]} T\left(f_x, f_y\right)_{f_x = \frac{x_1}{\lambda z}, f_y = \frac{y_1}{\lambda z}} \tag{6.2}$$

where λ represents the wavelength of the incident light, and the wave vector k equals to $2\pi/\lambda$. $T(f_x, f_y)$ is the Fourier transform of $t(x_0, y_0)$

$$T\left(f_x, f_y\right) = \left(e^{i\varphi_1} - e^{i\varphi_2}\right) \frac{a}{d} \mathrm{sinc}\left(\frac{a x_1}{\lambda z}\right) \sum_{n=-\infty}^{+\infty} \delta\left(\frac{x_1}{\lambda z} - \frac{n}{d}, \frac{y_1}{\lambda z}\right) + e^{i\varphi_2} \delta\left(\frac{x_1}{\lambda z}, \frac{y_1}{\lambda z}\right) \tag{6.3}$$

Equation (6.3) shows that the reflected light will be divided into several diffraction orders lying symmetrically on both sides of the incident light. The schematic of the $\pm 1^{th}$ orders is shown in figure 6.2(b).

If the incident light changes into LCP, the phase profile of the reflected LCP light is added to a minus sign [figure 6.2(c)]. Then equation (6.3) changes to

$$T'(f_x, f_y) = \left(e^{-i\varphi_1} - e^{-i\varphi_2}\right)\frac{a}{d}\mathrm{sinc}\left(\frac{ax_1}{\lambda z}\right)\sum_{n=-\infty}^{+\infty}\delta\left(\frac{x_1}{\lambda z} - \frac{n}{d}, \frac{y_1}{\lambda z}\right) + e^{-i\varphi_2}\delta\left(\frac{x_1}{\lambda z}, \frac{y_1}{\lambda z}\right) \quad (6.4)$$

And the schematic of the ±1[th] LCP light is shown in figure 6.2(d).

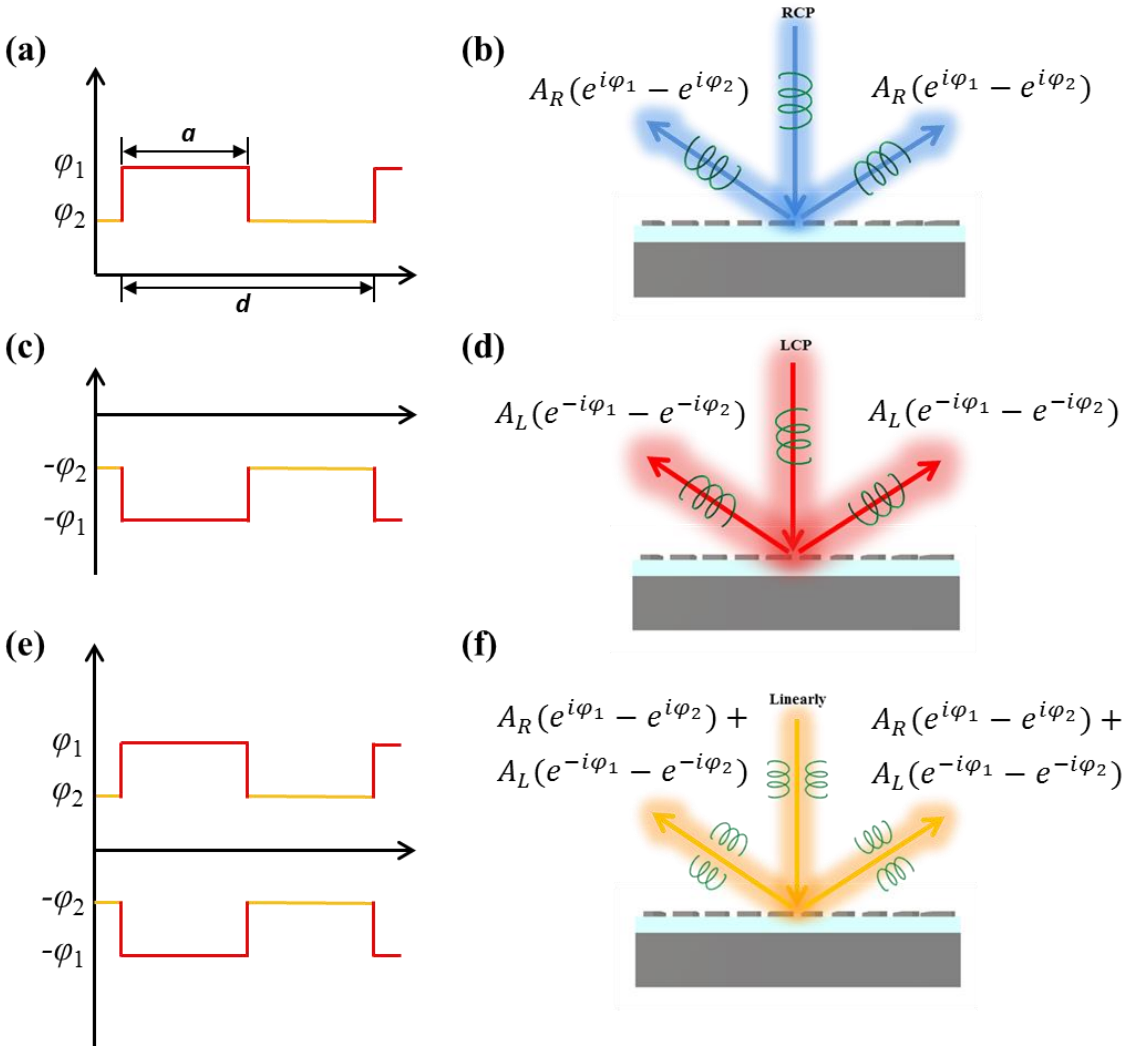

Figure 6.2 Design principles of the metasurface for polarization rotation. (a) Phase profile of the reflected RCP light from the metasurface. (b) The ±1[th] orders reflected RCP light both have the amplitude $A_R(e^{i\varphi_1} - e^{i\varphi_2})$. (c) Phase profile of the reflected LCP light. (d) The ±1[th] orders reflected LCP light both have the amplitude $A_L(e^{-i\varphi_1} - e^{-i\varphi_2})$. (e) Since the metasurface responds differently to the LCP and RCP light, it shows dual phase profiles for the linearly polarized incident light. (f) The +1[th] order LCP and RCP reflected light superpose and form a light beam with rotated polarization direction. So do the -1[th] order LCP and RCP reflected light.

A linearly polarized incident light beam consists of equal LCP and RCP components, and the metasurface responds differently to the two components [figure 6.2(e)]. Equations (6.3) - (6.4) denote that the n^{th} order (n=±1, ±2 …) reflected RCP and LCP light beams have the identical propagation direction, which forms an angle γ_n with the metasurface normal

$$\gamma_n = arctan\left(\frac{\lambda n}{d}\right) \quad (6.5)$$

Besides, they have the equal reflection coefficient since

$$\left|e^{i\varphi_1} - e^{i\varphi_2}\right| = \left|e^{-i\varphi_1} - e^{-i\varphi_2}\right| \tag{6.6}$$

The n^{th} order RCP and LCP reflected light also have a phase difference $\Delta\Phi$ between them, which is induced by the rectangular phase grating

$$\Delta\Phi = \varphi_{nR} - \varphi_{nL} = \text{phase}\left(e^{i\varphi_1} - e^{i\varphi_2}\right) - \text{phase}\left(e^{-i\varphi_1} - e^{-i\varphi_2}\right) \tag{6.7}$$

where the function *phase* extracts the phase angle of a complex number.

According to equations (6.5)-(6.7), the reflected RCP and LCP components have the equal amplitude, same propagation direction, and a phase difference $\Delta\Phi$. By properly adjusting the value of $\Delta\Phi$, the n^{th} order of RCP and LCP reflected light would superpose and form a linearly polarized light beam with a designable optical rotation angle [figure 6.2(f)]. For the *y*-polarized incident light (figure 6.1), it can be deduced that $\Delta\Phi$ is twofold of the optical rotation angle

$$\Delta\Phi = 2\beta_{rot} \tag{6.8}$$

Where the optical rotation angle β_{rot} is also defined in figure 6.1. Equation (6.7) can be rewritten as

$$\Delta\Phi = phase\left[\left(e^{i\varphi_{10}} - e^{i\varphi_{20}}\right)e^{i\alpha}\right] - phase\left(\left[e^{-i\varphi_{10}} - e^{-i\varphi_{20}}\right]e^{-i\alpha}\right) \tag{6.9}$$

where $\varphi_{10}+\alpha = \varphi_1$ and $\varphi_{20}+\alpha = \varphi_2$. If we choose $\varphi_{10} = \pi$ and $\varphi_{20} = 0$, $\Delta\Phi$ would have a very brief expression of

$$\Delta\Phi = 2\alpha \tag{6.10}$$

Equations (6.8) and (6.10) imply that α equals to β_{rot}, which provides an elegant way to encode the optical rotation angle to the configuration of the metasurface. To achieve the optical rotation angle β_{rot}, the values of $\{\varphi_1, \varphi_2\}$ can be written as $\{\pi+\beta_{\text{rot}}, \beta_{\text{rot}}\}$, which are then represented by a geometric metasurface similar to that in figure 6.1(b).

6.3 Simulation of the optical rotation functionality

Here, the polarization direction of a linearly polarized light is defined as the angle between the direction of the light oscillation and the *x*-axis as shown in figure 6.1. To verify the optical rotation method proposed above, four different samples are designed, aiming to rotate the 90° polarized (*y*-polarized) incident light by the angles of $\beta_{\text{rot}} = 45°$, 90°, 135° and 180°. In other words, the desired polarization directions of the reflected light from samples I-IV are -45°, 0°, 45° and 90°, respectively. As discussed above, the values of $\{\varphi_1, \varphi_2\}$ for the four samples I, II, III and IV are {225°, 45°}, {270°, 90°},

{315°, 135°} and {360°, 180°}, respectively. The SEM image of the sample III is shown in figure 6.1(c) as an example.

Prior to the experimental characterization of the samples, their optical rotation functionalities are first simulated using the diffraction theory. Here sample III is taken as an example. Each nanorod in the metasurface can be regarded as a point source that emits a diverging LCP (RCP) spherical wave. The initial phase of a spherical wave is $\pm 2\varphi$, and φ is the orientation angle of the corresponding nanorod. The '+' and '-' signs are valid for the RCP and LCP light, respectively. Then the amplitude distribution in the far field can be calculated as the superposition of all the spherical waves. Here A_L and A_R are used to represent the far-field amplitude distributions of LCP and RCP light, respectively.

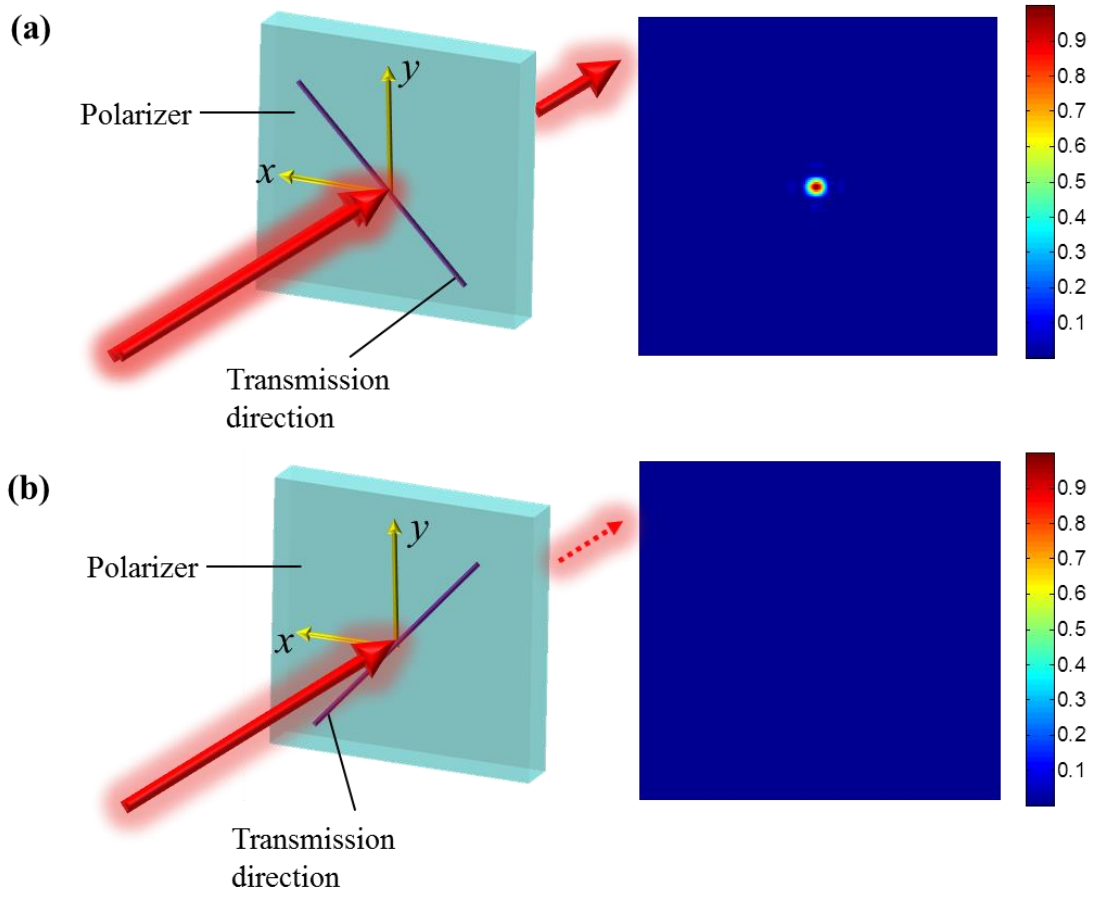

Figure 6.3 Polarization state of the reflected light from sample III if the incident light is linearly polarized along the *y* direction. An observation area around the $+1^{th}$ order with a size of 0.05×0.05 m^2 is chosen, and it is 1m away from the metasurface. The +45° and -45° linearly polarized components of the reflected light are calculated as shown in (a) and (b), respectively. The calculation process is equivalent to filtering the reflected light with a +45° or -45° polarizer.

If the incident light is linearly polarized along the *y*- direction, it has equal RCP and LCP components and a π phase difference between them. The Jones vector of the reflected light can be written as

$$R_{Jones} = \begin{bmatrix} A_L - A_R \\ iA_L + iA_R \end{bmatrix} \tag{6.11}$$

Then the +45° linearly polarized component of the reflected light can be represented by the Jones vector

$$J_{+45^\circ} = \frac{1}{2}\begin{pmatrix} 1 & 1 \\ 1 & 1 \end{pmatrix} R_{Jones} \tag{6.12}$$

The calculated result in an area around the +1th order is shown in figure 6.3(a). Similarly, the -45° linearly polarized component is

$$J_{-45^\circ} = \frac{1}{2}\begin{pmatrix} 1 & -1 \\ -1 & 1 \end{pmatrix} R_{Jones} \tag{6.13}$$

And the result is shown in figure 6.3(b). The calculation clearly shows the reflected light has no -45° linearly polarized component. Therefore the reflected light is +45° linearly polarized, which agrees well with our initial design.

6.4 Experimental verification of the optical rotation functionality

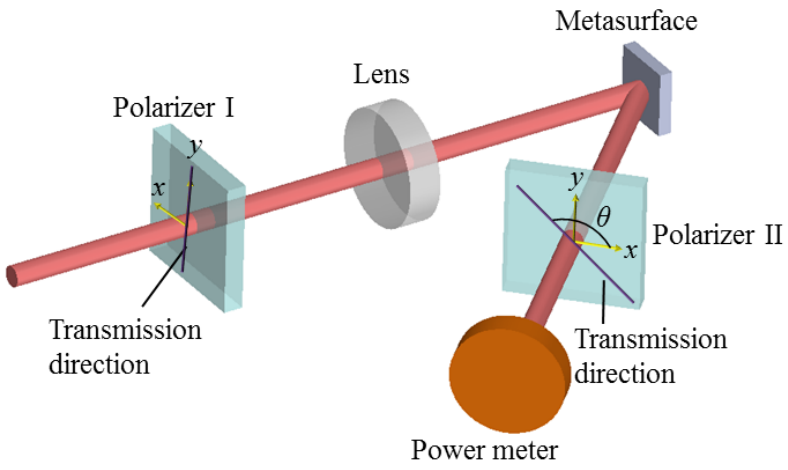

Figure 6.4 Experimental setup to characterize the polarization state of the reflected light. The incident light passes through the polarizer I and is shrunk by the lens, then it is incident normally onto the metasurface. The polarization state of the +1th order reflected light is measured by polarizer II and the power meter.

The experimental setup to characterize the optical rotation functionality of the fabricated samples is shown in figure 6.4. The incident light comes from a supercontinuum laser; then it passes through polarizer I with the transmission axis along

the *y*-direction. The light is focused by a lens and impinges normally onto the metasurface. The polarization state of the reflected light is analyzed by rotating polarizer II to different directions θ and recording the intensity values *I*. The obtained $I(\theta)$ curve carries the polarization information of the reflected light.

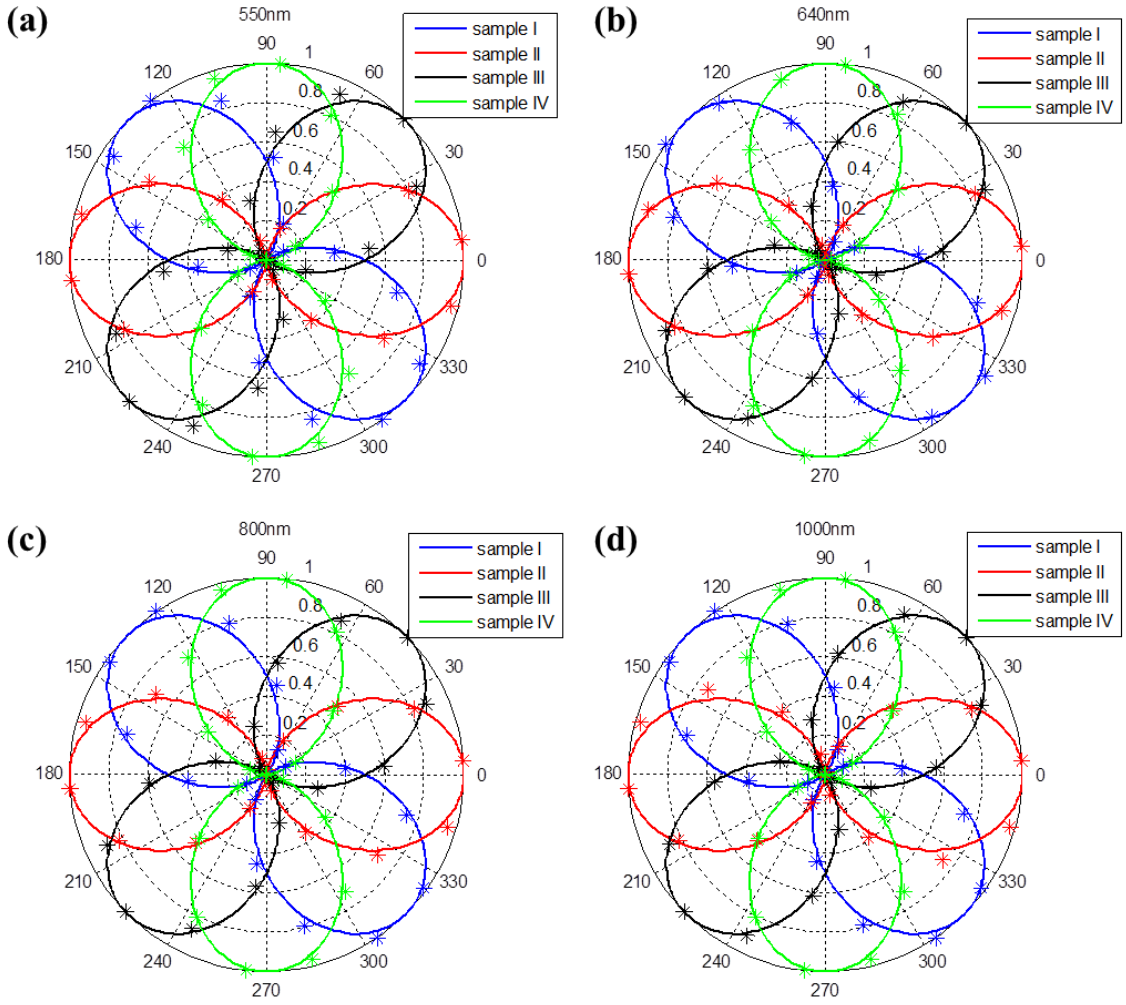

Figure 6.5 Measured polarization states at different wavelengths. The blue, red, black and green discrete asterisks represent the measured intensity values from samples I, II, III and IV, respectively. The four solid lines denote the ideal $I(\theta)$ curves corresponding to the -45°, 0°, 45° and 90° linearly polarized light. The incident wavelengths are (a) 550nm, (b) 640 nm, (c) 800nm and (d) 1000nm.

The wavelength of the incident light is first set to be 550 nm. As shown in figure 6.5(a), the individual asterisks represent the experimentally obtained intensity values at different θ, and they are plotted in a polar coordinate. The blue, red, black and green colors denote the results obtained from samples I, II, III and IV, respectively. The four solid lines represent the predicted $I(\theta)$ curves for the linearly polarized light along -45°, 0°, 45° and 90°. The location of a curve peak at a certain angle θ denotes its polarization direction. As the experimental results agree well with the predicted ones, it

unambiguously shows that samples I-IV rotate the incident light to the designed polarization angles. Since the geometric phase induced by a nanorod is solely determined by its orientation, the optical rotation method proposed above is valid for a broad range of wavelengths. Here the four samples are tested with other three wavelengths of 640 nm, 800 nm, and 1000 nm, and the experimental results show good agreement with the predicted values [figures 6.5(b)-(d)].

Since a majority of the reflected energy is concentrated to the $\pm 1^{th}$ orders, the conversion efficiency is defined as the total intensities of $\pm 1^{th}$ orders reflected light divided by that of the incident light. The conversion efficiency of sample IV is experimentally measured as shown in figure 6.6, which is comparable with that in chapter 5.

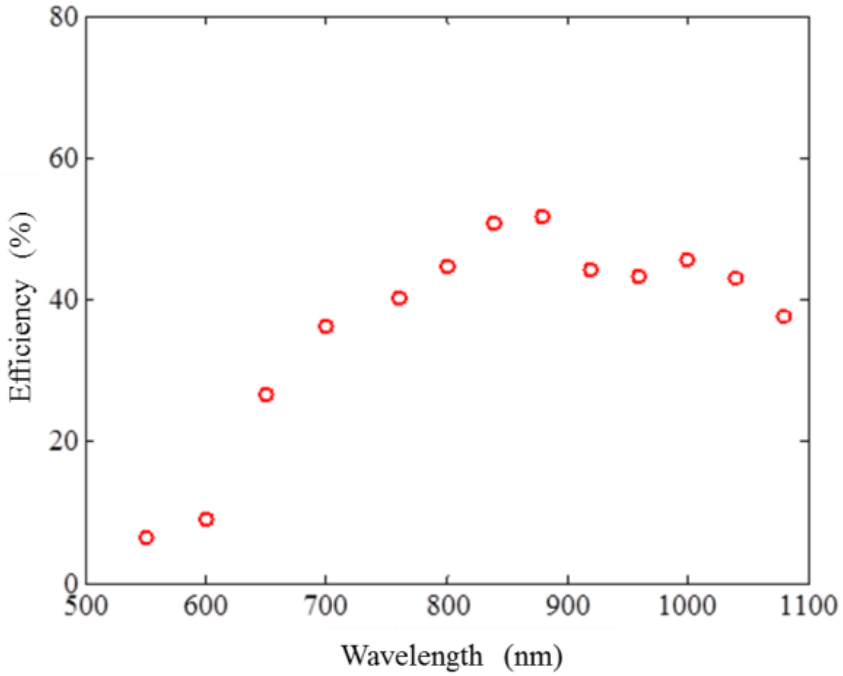

Figure 6.6 Measured conversion efficiency of sample IV.

6.5 Discussion

The energy distribution among different reflection orders is related to the configuration of the metasurface. As shown in equation (6.3), the intensity of the n^{th} order reflected light has to satisfy

$$I_n \propto \left|\left(e^{i\varphi_1} - e^{i\varphi_2}\right)\frac{a}{d}\,sinc\left(\frac{na}{d}\right)\right|^2 \tag{6.14}$$

If we have $\varphi_1 = \pi + \alpha$ and $\varphi_2 = \alpha$, equation (6.14) is simplified as

$$I_n \propto \left|\frac{1}{n\pi}\,sin\left(\frac{na\pi}{d}\right)\right|^2 \tag{6.15}$$

As a result, *a/d* is the key parameter determining the energy distribution. The normalized reflection intensities of the first four orders versus *a/d* are shown in figure 6.7. In this chapter, a majority of the reflected light is designed to concentrate on the $\pm 1^{th}$ orders. So *a/d* is chosen to be 0.5, with a = 1.2 μm and d = 2.4 μm. It should be noted that the measured efficiency is about 26% for each order due to the equal energy distribution between the $\pm 1^{th}$ orders. However, the design is applicable for the cases when the optical rotation and beam splitting have to be met simultaneously.

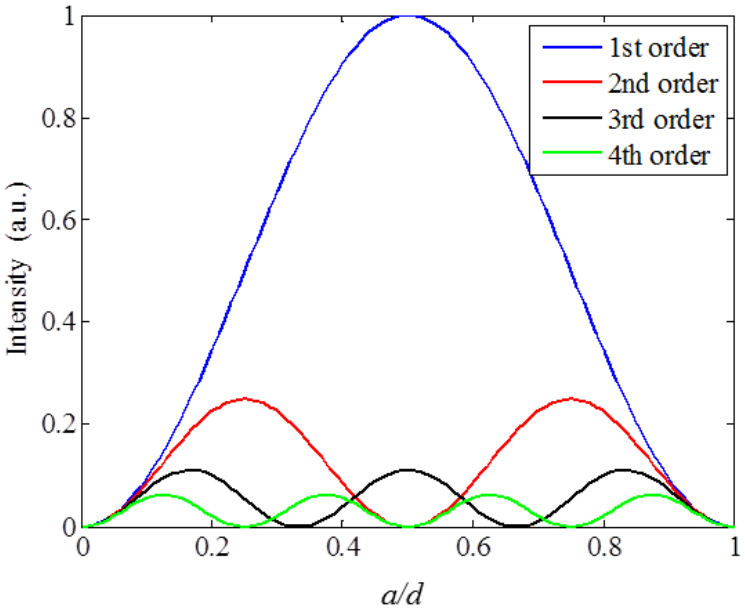

Figure 6.7 Normalized intensity distributions of the first four reflection orders.

In comparison with other methods for the optical rotation, such as the combination of two sawtooth gratings with a spatial displacement [6.16], the one proposed here does not shift the reflected light away from the designed plane (figure 6.8). The fabricated samples maintain the polarization rotation functionality for different wavelengths; however, it is worth noting that the reflection angles change with the wavelengths, as shown in equation (6.5).

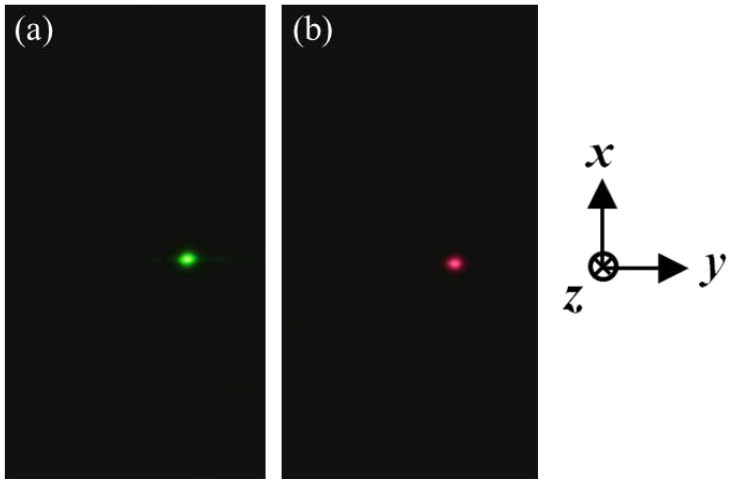

Figure 6.8 The area around the +1th order in the observation plane at (a) 550 nm and (b) 600 nm.

The polarization contrast ratio of the reflected light is measured, which is defined as the intensity ratio between the desired polarization and its cross polarization. The sample IV is taken as an example, and the results are shown in table 6.1. It verifies that the polarization state of the reflected light agrees with the initial design and the noise is low.

Table 6.1 Measured polarization contrast ratio of the reflected light from sample IV

Wavelength(nm)	550	600	660	700	750	800
Ratio(dB)	23.7	27.0	28.9	36.2	33.0	38.0
Wavelength(nm)	850	900	950	1000	1050	1090
Ratio(dB)	33.8	34.3	30.3	30.2	28.4	27.5

Although the metasurfaces are designed to provide high conversion efficiency when the incident light is normal to the metasurface, their optical rotation functionality still exists when the incident light is tilted to a certain degree (figure 6.9).

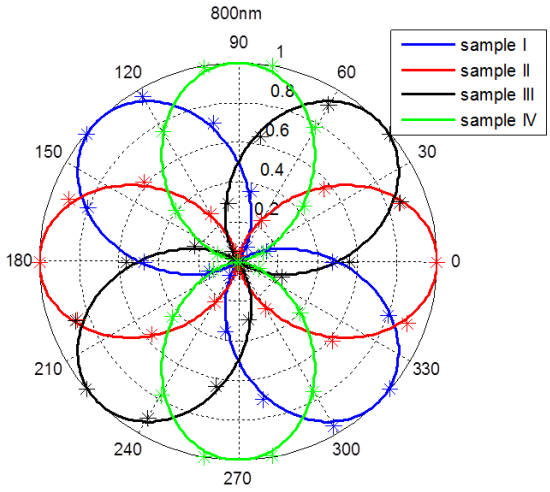

Figure 6.9 Polarization state of the reflected light when the incident angle is 15.22°. The incident light is set to be *y*-polarized.

6.6 Conclusion

In conclusion, we propose an approach to rotate the incident linearly polarized light to arbitrarily designed directions by using the metasurface-based rectangular phase gratings. The optical rotation angle of the reflected light is solely dependent on the phase steps in the grating, providing an elegant way to realize the optical rotation. The reflection-type metasurface has high efficiency in the visible and near infrared range. Besides, the geometric phase is independent of the wavelengths, which guarantees the broadband performance of the metasurface. Since this approach addresses several major issues of the traditional optical rotation elements, such as the volume and bandwidth, it may facilitate the device miniaturization and system integration.

6.7 References

6.1 L. D. Barron, *Molecular light scattering and optical activity*, Cambridge University Press, Cambridge (2004).

6.2 A. I. Rusanov, and A. G. Nekrasov, *One More Extreme near the Critical Micelle Concentration: Optical Activity*, Langmuir **26**, 13767-13769 (2010).

6.3 Y. A. He, B. Wang, R. K. Dukor, and L. A. Nafie, *Determination of Absolute Configuration of Chiral Molecules Using Vibrational Optical Activity: A Review*, Appl. Spectrosc. **65**, 699-723 (2011).

6.4 H. J. Rhee, et al., *Femtosecond characterization of vibrational optical activity of chiral molecules*, Nature **458**, 310-313 (2009).

6.5 J. K. Gansel, et al., *Gold Helix Photonic Metamaterial as Broadband Circular Polarizer*, Science **325**, 1513-1515 (2009).

6.6 S. Zhang, et al., *Negative Refractive Index in Chiral Metamaterials*, Phys. Rev. Lett. **102**, 023901 (2009).

6.7 D.-H. Kwon, D. H. Werner, A. V. Kildishev, and V. M. Shalaev, *Material parameter retrieval procedure for general bi-isotropic metamaterials and its application to optical chiral negative-index metamaterial design*, Opt. Express **16**, 11822-11829 (2008).

6.8 E. Plum, et al., *Metamaterial with negative index due to chirality*, Phys. Rev. B **79**, 035407 (2009).

6.9 N. Yu, et al., *Light Propagation with Phase Discontinuities: Generalized Laws of Reflection and Refraction*, Science **334**, 333-337 (2011).

6.10 A. V. Kildishev, A. Boltasseva, and V. M. Shalaev, *Planar Photonics with Metasurfaces*, Science **339**, 1232009 (2013).

6.11 N. K. Grady, et al., *Terahertz Metamaterials for Linear Polarization Conversion and Anomalous Refraction*, Science **340**, 1304-1307 (2013).

6.12 D. Wen, et al., *Helicity multiplexed broadband metasurface holograms*, Nat. Commun. **6**, 9241 (2015).

6.13 F. Yue, et al., *Vector Vortex Beam Generation with a Single Plasmonic Metasurface*, Acs Photonics **3**, 1558–1563 (2016).

6.14 A. Papakostas, et al., *Optical Manifestations of Planar Chirality*, Phys. Rev. Lett. **90**, 107404 (2003).

6.15 M. Kuwata-Gonokami, et al., *Giant optical activity in quasi-two-dimensional planar nanostructures*, Phys. Rev. Lett. **95**, 227401 (2005).

6.16 A. Shaltout, J. Liu, V. M. Shalaev, and A. V. Kildishev, *Optically Active Metasurface with Non-Chiral Plasmonic Nanoantennas*, Nano Lett. **14**, 4426-4431 (2014).

6.17 C. Pfeiffer, and A. Grbic, *Bianisotropic Metasurfaces for Optimal Polarization Control: Analysis and Synthesis*, Phys. Rev. A **2**, 044011 (2014).

6.18 F. Ding, Z. Wang, S. He, V. M. Shalaev, and A. V. Kildishev, *Broadband High-Efficiency Half-Wave Plate: A Supercell-Based Plasmonic Metasurface Approach*, ACS NANO **9**, 4111-4119 (2015).

6.19 A. Pors, M. G. Nielsen, and S. I. Bozhevolnyi, *Broadband plasmonic half-wave plates in reflection*, Opt. Lett. **38**, 513-515 (2013)

6.20 Z. H. Jiang, et al., *Broadband and Wide Field-of-view Plasmonic Metasurface-enabled Waveplates*, Sci. Rep. **4**, 07511 (2014).

6.21 J. Goodman, *Introduction to Fourier Optics*, Roberts & Company Publishers, Englewood Colorado (2005)

6.22 N. LV, *Fourier Optics*, China Machine Press, Beijing (2006).

Chapter 7 Conclusions and Outlook

7.1 Conclusions

In this study, nanorods of subwavelength sizes are used as building blocks to form geometric metasurfaces, which give geometric phase to the transmitted or reflected light. The sign of geometric phase is determined by the helicity of the incident light, which yields miniature optical devices of novel applications. In chapter 3, a phase gradient metasurface is proposed that provides opposite phase gradient to the anomalously refracted LCP and RCP components, and therefore send them to different directions. The ellipticity and helicity of the incident polarized light can be obtained by measuring the intensities of the two components. In chapter 4, two optical elements with different functionalities, such as a hologram and a cylindrical lens, can be integrated into a single device. The overall performance of the device is determined by the helicity of the incident circularly polarized light. In chapter 5, a broadband high-efficiency metasurface hologram is realized with helicity multiplexed functionalities. Two holographic images swap their positions when the helicity of the incident light is reversed. In chapter 6, a metasurface is used to realize a rectangular phase grating, which gives the designed optical rotation angle to the reflected light according to the heights of the two phase steps.

In conclusion, the geometric metasurface based optical elements have the following key strengths. First of all, the fabrication of metasurfaces is much simpler than that for three-dimensional metamaterials. Second, the distance between neighboring nanorods can be subwavelength, which not only gives a fine sampling of a phase function but also minimize the total size of the device. Also, arbitrary phase levels can be achieved since the geometric phases are solely determined by the orientations of the nanorods. Finally, the different responses of the geometric metasurfaces to the incident LCP and RCP light can yield many novel optical properties.

7.2 Outlook

The development of metasurface devices continues to evolve rapidly. However, there are still several major challenges. For example, most of the metasurfaces are fabricated by using ebeam lithography or focused ion beam, imposing a cost barrier to their mass applications. Recently, much effort has been made to achieve large scale metasurfaces with alternative ways. For example, large-scale metasurface for near perfect absorption has been experimentally demonstrated using direct sputtering

deposition. Random metallic nanoparticles layer can be formed on a substrate by controlling the deposition and post-treatment conditions [7.1]. Chemically synthesized silver nanocubes can be randomly adsorbed by a polymer spacer layer on a gold film, which forms a large scale metasurface absorber without the need to control the accurate position of each nanocube [7.2]. Despite the successful demonstrations of metasurface absorbers, large scale metasurfaces to achieve phase and polarization control still need nanoantennas with precise geometry, orientations, and positions, whose fabrication process remains to be improved.

The integrations of metasurfaces to other optical elements are more important for real applications than their usages as single devices. Metasurfaces can be fabricated on the end of the optical fibers using "decal transfer" [7.3] technique to enhance the Raman scattering signals [7.4]. Or else the nanopatterns can be placed along the fibers to interact with the evanescent waves [7.5]. The combination of metasurface with the magneto-optical material can enhance the degree of the polarization rotation, due to the strong coupling between the localized plasmon resonance of the metasurface and the waveguide mode of the magneto-optical film [7.6, 7.7]. By integrating metasurfaces onto the commercially available silicon photodiodes, the orbital angular momentum can be selectively detected [7.8]. In spite of the efforts toward the integrations of metasurfaces with other devices, the commonly used materials, such as gold and silver, still lacks CMOS compatibility. Also, the overall efficiency of the integrated systems has to be improved.

The properties of metasurfaces can be adjusted if their component materials are tunable versus the external field. For instance, the conductivity of doped semiconductors can be adjusted by the voltage bias and photoexcitation [7.9, 7.10]. Therefore semiconductors prove to be an ideal material for tunable metasurfaces in the microwave, THz and near infrared ranges [7.11]. Besides, the helix pitch of the chiral nematic liquid crystal can be tuned using external stimulate such as heat and electric field. Therefore its reflection band can be tuned by the temperature and voltage [7.12]. The phase-change medium $Ge_2Sb_2Te_5$ can switch between an amorphous state and a metastable cubic crystalline state by femtosecond laser pulses. Hence the functionality of a metasurface based on $Ge_2Sb_2Te_5$ can be erased and rewritten in a dynamical way [7.13]. Overall, since active control of metasurfaces would largely extend their applications, metasurfaces with smart responses to the external stimulation will play a critical role in the future development of metasurfaces.

As the metasurfaces are developing rapidly, a lot of novel applications are induced thereby. Besides the phase, amplitude and polarization control in free space as mentioned in chapter 1, metasurfaces prove to be effective when applied to the fields of guided wave optics [7.14-7.16], nonlinear optics [7.17-7.23], spin-Hall effect [7.24-7.25], chemical sensors [7.26], polarimeters [7.27-7.28], and so on. Despite the great advances in metasurfaces, there is still large room for improvements in electric or optical tunability, CMOS compatibility and manufacturing techniques, which are the key points for large scale applications.

7.3 References

7.1 K. Liu, et al., *A large-scale lithography-free metasurface with spectrally tunable super absorption*, Nanoscale **6**, 5599-5605 (2014).

7.2 A. Moreau, et al., *Controlled-reflectance surfaces with film-coupled colloidal nanoantennas*, Nature **492**, 86-89 (2012).

7.3 E. J. Smythe, M. D. Dickey, G. M. Whitesides, and F. Capasso, *A Technique to Transfer Metallic Nanoscale Patterns to Small and Non-Planar Surfaces*, ACS NANO **3**, 59-65 (2009).

7.4 E. J. Smythe, M. D. Dickey, J. M. Bao, G. M. Whitesides, and F. Capasso, *Optical Antenna Arrays on a Fiber Facet for in Situ Surface-Enhanced Raman Scattering Detection*, Nano Lett. **9**, 1132-1138 (2009).

7.5 N. Yu, and F. Capasso, *Optical Metasurfaces and Prospect of Their Applications Including Fiber Optics*, J. Lightwave Technol. **33**, 2344-2358 (2015).

7.6 J. Y. Chin, et al., *Nonreciprocal plasmonics enables giant enhancement of thin-film Faraday rotation*, Nat. Commun. **4**, 1599 (2013).

7.7 D. Floess, et al., *Tunable and switchable polarization rotation with non-reciprocal plasmonic thin films at designated wavelengths*, Light-Sci Appl **4**, e284 (2015).

7.8 P. Genevet, J. Lin, M. A. Kats, and F. Capasso, *Holographic detection of the orbital angular momentum of light with plasmonic photodiodes*, Nat. Commun. **3**, 2293 (2012).

7.9 C. Hou-Tong, J. T. Antoinette, and Y. Nanfang, *A review of metasurfaces: physics and applications*, Rep. Prog. Phys. **79**, 076401 (2016).

7.10 M. Ferrera, et al., *Dynamic nanophotonics [Invited]*, J. Opt. Soc. Am. B **34**, 95-103 (2016).

7.11 M. U. Augustine, et al., *Roadmap on optical metamaterials*, J. Opt. **18**, 093005 (2016).

7.12 J. Kobashi, H. Yoshida, and M. Ozaki, *Planar optics with patterned chiral liquid crystals*, Nat. Photon. **10**, 389-393 (2016).

7.13 Q. Wang, et al., *Optically reconfigurable metasurfaces and photonic devices based on phase change materials*, Nat. Photon. **10**, 60-65 (2016).

7.14 A. Wu, et al., *Experimental Demonstration of In-Plane Negative-Angle Refraction with an Array of Silicon Nanoposts*, Nano Lett. **15**, 2055-2060 (2015).

7.15 D. Ohana, B. Desiatov, N. Mazurski, and U. Levy, *Dielectric Metasurface as a Platform for Spatial Mode Conversion in Nanoscale Waveguides*, Nano Lett. **16**, 7956-7961 (2016).

7.16 Z. Li, et al., *Controlling propagation and coupling of waveguide modes using phase-gradient metasurfaces*, Nat. Nano. **advance online publication** (2017).

7.17 G. Li, et al., *Continuous control of the nonlinearity phase for harmonic generations*, Nat. Mater. **14**, 607-612 (2015).

7.18 N. Segal, S. Keren-Zur, N. Hendler, and T. Ellenbogen, *Controlling light with metamaterial-based nonlinear photonic crystals*, Nat. Photon. **9**, 180-184 (2015).

7.19 M. Tymchenko, et al., *Gradient Nonlinear Pancharatnam-Berry Metasurfaces*, Phys. Rev. Lett. **115**, 207403 (2015).

7.20 R. Camacho-Morales, et al., *Nonlinear Generation of Vector Beams From AlGaAs Nanoantennas*, Nano Lett. **16**, 7191-7197 (2016).

7.21 G. Grinblat, Y. Li, M. P. Nielsen, R. F. Oulton, and S. A. Maier, *Enhanced Third Harmonic Generation in Single Germanium Nanodisks Excited at the Anapole Mode*, Nano Lett. **16**, 4635-4640 (2016).

7.22 L. Gui, et al., *Nonlinear Refractory Plasmonics with Titanium Nitride Nanoantennas*, Nano Lett. **16**, 5708-5713 (2016).

7.23 F. Walter, G. Li, C. Meier, S. Zhang, and T. Zentgraf, *Ultrathin Nonlinear Metasurface for Optical Image Encoding*, Nano Lett. **17**, 3171–3175 (2017).

7.24 J. Sun, et al., *Spinning Light on the Nanoscale*, Nano Lett. **14**, 2726-2729 (2014).

7.25 A. Shaltout, J. J. Liu, A. Kildishev, and V. Shalaev, *Photonic spin Hall effect in gap-plasmon metasurfaces for on-chip chiroptical spectroscopy*, Optica **2**, 860-863 (2015).

7.26 H. T. Miyazaki, et al., *Dual-band infrared metasurface thermal emitter for CO2 sensing*, Appl. Phys. Lett. **105** (2014).

7.27 A. Pors, M. G. Nielsen, and S. I. Bozhevolnyi, *Plasmonic metagratings for simultaneous determination of Stokes parameters*, Optica **2**, 716-723 (2015).

7.28 J. P. B. Mueller, K. Leosson, and F. Capasso, *Ultracompact metasurface in-line polarimeter*, Optica **3**, 42-47 (2016).